MODELLING OF THE MECHANISMS GOVERNING CRIMP IN WOOL

A thesis

submitted in partial fulfilment of

the requirements for the Degree

of

Doctor of Philosophy

in

Computational and Applied Mathematics

in the

University of Canterbury

by

Bernie Pui Man Tsang

University of Canterbury

2003

Acknowledgments

First, I would like to thank my principal supervisor, Professor Graeme C. Wake. Thank you for regularly giving so generously of your time, for teaching me a lot about research and for searching out sources of funding, and for your constant optimism and encouragement.

Sincere thanks are due also my external supervisors, Dr. Clive Marsh, Dr. Bruce van Brunt and Dr. David Cottle. Thank you for your enthusiasm for the project and the personal interest you have taken in me and my work. Also, my ex-supervisor, Assoc. Professor Bruce Robson, who tragically passed away in the middle of the project. Thanks for given me some precious suggestions.

Many thanks to Dr. Andy Wilkins for your generous help, interest and valuable advice throughout the time. Thank you for Dr. John W. S. Hearle for your advice and kindness to let me use the materials of your presentation from the 13th International Hair-Science Symposium. Also, sincere thanks to Dr. Hilary Ockendon of OCIAM of University of Oxford for your advantageous suggestions.

I would like to thank Canesis/Wool Research Organisation of New Zealand (WRONZ) and New Zealand Wool Industry Charitable Trust for their contributions of grants. Thanks to people in WRONZ who gave me many necessary information and Peter Durrant for helping with the photographic procedures and for providing the necessary equipment.

Finally, I would like to thank the Department of Mathematics and Statistics of University of Canterbury for providing a friendly and comforting environment for my study in these year.

Abstract

This thesis considers modelling one of the mechanisms, which governs the formation of wool fibres. The problem is investigated by constructing a mathematical model that is based on the geometry of the ultrastructure of the wool fibres. The deformed shapes of the wool fibres are obtained by minimising the strain energy calculated from the mathematical model. The objective of this study is to explore the relationship between the ultrastructure and the crimpy shape of the wool fibres.

The first chapter gives the background information of wool fibre, the outline of the thesis and defines the problem.

The second chapter examines the structures inside the wool fibres and the mechanisms, which govern the shapes of the wools fibres. The variables used to describe the fibre shapes are introduced here. Then, some simple examples are given to demonstrate the mathematical model.

In the third chapter, the structures of the wool fibres are simplified with several assumptions and used to construct the basic model. Then, some results are given with various values of different parameters to demonstrate the properties of the model. Some modifications of the model are made, which include the addition of the cuticle shell and an approximate analytical model by Taylor's expansion.

The fourth chapter develops another modification of the mathematical model with the addition of a 'macrofibril' structure. The fifth chapter gives the last modification of the model uses integration to calculate the total energy of the whole fibre.

The sixth and the seventh chapters show the practical methods to measure the natural shape of a single fibre and the cross-section pattern of the fibre respectively. The measured natural shape of the wool fibre can be used to verify the local estimated shape of the wool fibre, which is calculated by the mathematical model with the measured cross-section pattern.

Contents

List of Figures

1 Introduction

1.1 Background

This thesis deals with the problem of finding wool fibre shape that relates to its ultrastructure. This problem is of interest to textile researchers wishing to improve the quality of wool fibre products. With the development of the genetic engineering, it is possible to alter the ultrastructure of wool fibre. Therefore, if we know about the relationship between the ultrastructure and the shape of wool fibre, it is possible in the future that we can control the quality of wool fibre.

Since wool fibre products are one of the major export products for New Zealand, there is the need to make sure that they can maintain their high quality so as to compete in the worldwide market. There are six characteristics to predict wool processing and end-product performance, including fibre diameter, fibre length after carding loose wool bulk, the degree of unscourable discolouration, the lustre of fibre and presence of vegetable matter. Fibre diameter, fibre length after carding, unscourable discolouration and vegetable matter are of particular importance for fine wools suitable for spinning into fine yarn. In the case of coarser crossbred type wool, bulk, along with staple length and discolouration, are important for machine-made carpets, hand-knitting yarns and bedding products.

Wool bulk is the factor that relates to the research of this thesis. Generally, wool bulk relates to the ability of wool to fill space. Although there are different definitions of wool bulk in different countries, a suggested measurement of bulk is the volume occupied by a gram of clean scoured carded wool under a defined pressure. Low bulk wools range between 18 and 22 cm^3/g while high bulk wools range between 30 and 35 cm^3/g under a defined pressure.

The productivity of wool can be increased by increasing the fleece weight. Farmers have incorporated high fleece weight lustre breeds into their flocks

to increase the mean diameter of the clip. However, lustre and bulk are negatively correlated with lustrous wools having a low bulk and vice versa, consequently, lustre has also increased with a corresponding drop in bulk. Low bulk lustrous wool is preferred for hand-made carpet yarn market to give a special visual effect, but lack of wool bulk causes the loss of market in many other products. High bulk wool has the ability to fill space, thus, yarns made from high bulk wool appear fuller than yarns made from low bulk wool. Moreover, high bulk wool is preferred for machine-made carpets, where it improves wearability and appearance retention, and in knitting yarns. The natural crimp of the high bulk fibre can entrap air effectively and acts as a better thermal insulator. This trapped air improves the warmth of knitted garments and over and underlay bedding quilts. High bulk wool is also less prone to felting than low bulk wool, thereby improving durability during use.

Bulk is closely related to fibre crimp. Individual fibres in high bulk wool possess a helical crimp analogous to a coiled spring, whereas individual fibres in low bulk wool have a flat or planar crimp. The effect of this difference in crimp type means that individual fibres in low bulk wools can pack closely together, giving the visually pleasing effect of a pronounced staple crimp termed character. The coiled fibres of high bulk wool cannot pack closely together and result in a poorly defined staple crimp. Fibre crimp can be partially described by curvature of the fibre curve. The effect of the fibre diameter and fibre curvature on the core bulk of wool fibres has been studied (e.g. [12], [19]).

1.2 The problem

The production of wool products involves several stages which are shown as in Figure 1. The formation of wool fibre includes the biological and physical changes of the wool fibre; then, in the processing stage, wool fibres are converted into yarns and fabric through different processes, which include shearing, scouring, carding, spinning etc. finally, the yarns and fabric are

made into various products (e.g. carpet, knitwear, apparel). The main objective is to improve the quality of wool fibre by increasing the amount of wool crimp and hence the wool bulk. Therefore, in this thesis, we are concerned with the mechanism that determines wool fibre crimp in the first instance. More detail is provided in the next chapter.

From a previous study of the wool fibre, the ultrastructure of the wool fibre is observed to have a relationship to the fibre shape (Figure 2). Thus, we are trying to fill the gap between the ultrastructure of the wool fibre and wool fibre shape by forming a mathematical model that can describe the dominating mechanism.

By studying the geometry of the different cells and structures inside the wool fibre, we are able to formulate and calculate the strain energy wool fibre induced when changing into different shapes in term of several properties (e.g. curvature and torsion). Since the wool fibre is considered to form shape that ensures it attains an equilibrium or minimum energy state, we can minimise the strain energy equation of the wool fibre to find the deformed shape of the fibre. The idea of the mechanism is discussed in chapter 2 and the mathematical formulations are given in chapter 3.

1.3 Outline of thesis

1.3.1 Chapter 2

The central theme of this thesis is finding the mechanism that controls the deformed shape of wool fibre. Having the hypothesis that the deformed shape is related to the ultrastructure inside the wool fibre, we must understand the appearance of the ultrastructure. Section 2.1 gives a brief description of the ultrastructure of wool fibre, the growth of wool fibre and the specific part we are considering.

In section 2.2, various models are proposed in which wool fibre is considered as a "bimetallic strip" as previous authors have described. Then, the

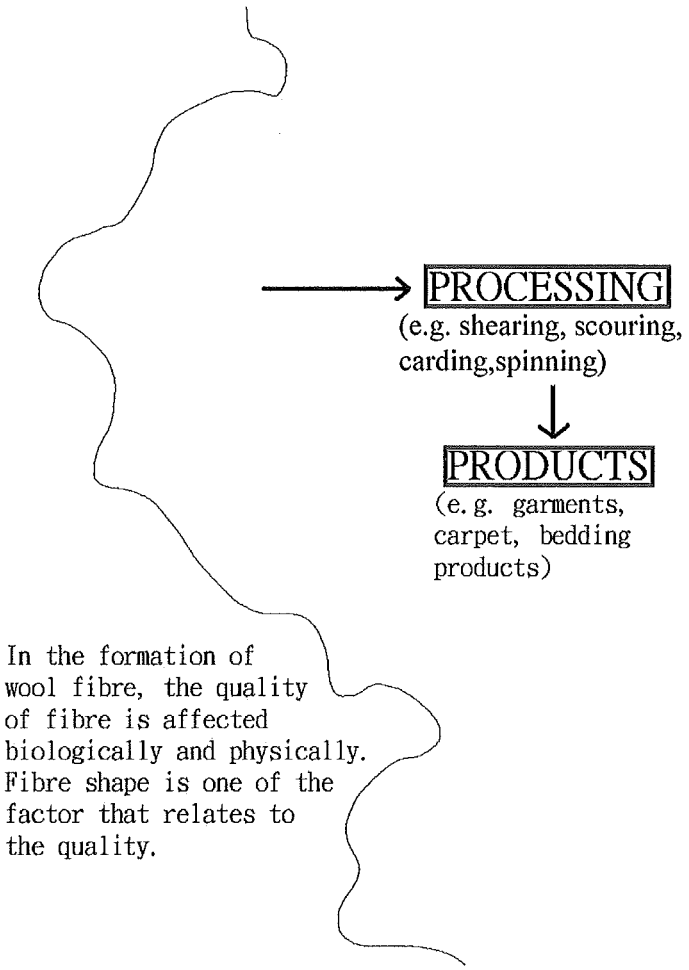

Figure 1: Diagram of stages from wool fibre to end-product

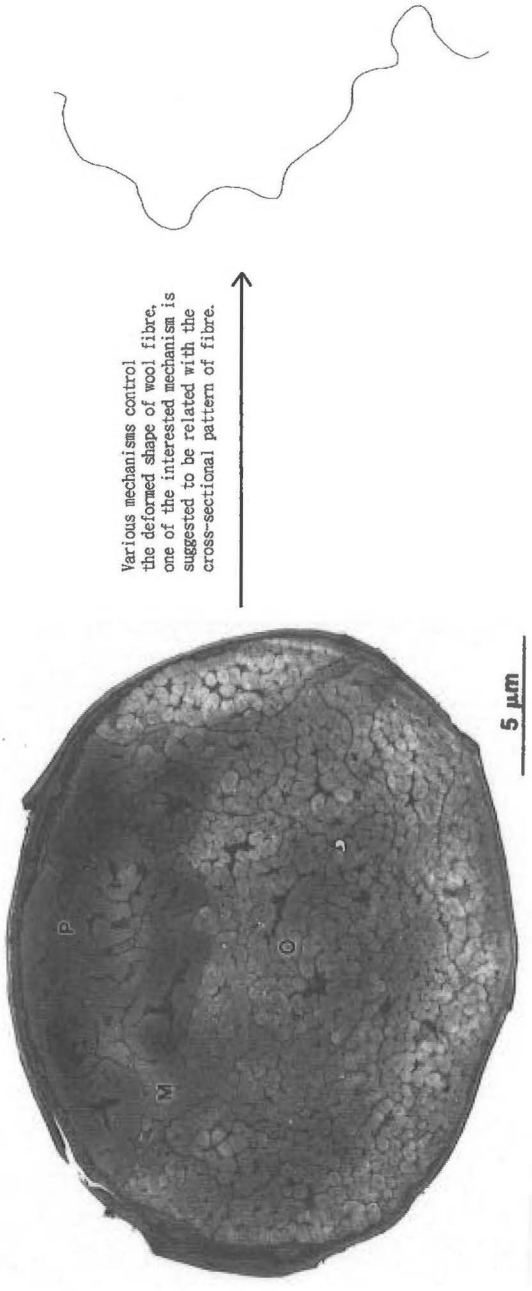

Figure 2: Relationship between ultrastructure and the fibre shape

suggested mechanism is determined from the practical consideration of the ultrastructure of the wool fibre. By making several assumptions, we form a simplified ideal model that reduces the number of variables and still gives reasonable results.

Starting with this simplified concept, we thus add further detail so as to form a realistic model, which has a limited number of variables. In the following section, several simple examples show the fundamental idea of the mathematical model and also the importance of the parameter torsion, which does not always appear in the description of the deformed shape of wool fibre in various models.

1.3.2 Chapter 3

In chapter 3, the formulations and the mathematical concepts of a basic model are shown. This model ignores a structure called macrofibril in wool fibre. Without the macrofibril, the computation is largely reduced and the model can still give reasonable predictions of the deformed shape of wool fibres.

Some "experimental" results are also given with the effects of various parameters of the fibre model being investigated by computer simulation, such as the different ultrastructure pattern and the amount of lateral contraction applied to the fibre, which reflect the properties of the mathematical model. Some modifications of the model are also demonstrated with asymptotic large parameter expansion and the addition of the cuticle, which is the outer shell of the fibre.

1.3.3 Chapters 4 and 5

Chapters 4 and 5 cover the extension of the basic model. In chapter 4, it is modified by adding the macrofibril structure. This model is considered to be more realistic with the additional feature that the estimated fibre shape is

closer to a straight line rather than a helical shape. We then show that the result can be improved with the addition of cuticle to the model.

The basic model in chapter 3 and macrofibril model in chapter 4 are both "discrete" models. In these models, the strain energy of the individual inner structure elements are calculated individually and then summed. In chapter 5, a continuum model is constructed. The intention of developing this model is to reduce the large amount of computation in the discrete models, especially the macrofibril model.

1.3.4 Chapter 6

To verify the accuracy of the simulation results, we need to compare them to the actual values in practice. Therefore, we develop a method to measure the fibre shapes. The natural fibre shapes are obtained by photographing them at various angles in several 2D images. With the known value of the difference of the angles between these 2D images, the 2D curves are transformed into discrete points along the curve. Then, we are able to construct 3D images of the wool fibres point by point and calculate the fibre shapes in terms of curvature and torsion. The analysis of the results is also discussed in this chapter.

1.3.5 Chapter 7

We show how to obtain the outer shape of wool fibres from the previous chapter. We then have to know how to measure the ultrastructure pattern inside the wool fibres that provide the data needed in the simulations. In the first part of this chapter, we show various microscopy methods to obtain the ultrastructure of the wool fibre. In the second part, the measured microscopy examples are used with the mathematical model to estimate the local shape of the fibre.

2 Mechanism of wool crimping

2.1 Brief description of wool follicle

There are many unknown aspects about wool follicles that involve various biological, chemical and physical processes. For example, protein synthesis, cell differentiation and the change of hair shape are not well understood. Figure 3 shows the inner structures of a wool follicle. The formation of the follicle starts at the bulb, which is labelled zone A. It is here that the cells are formed. In zone B, protein synthesis and cell differentiation in the cortices start. Cell differentiation continues, and different layers of cells are formed from zones C to E. The cells stop growing and do not change shape after zone E. In other words, the biological and chemical processes are completed by zones F and G. The wool follicle emerges from the skin, and it is here that the shape of the wool fibre begins to change. In this thesis we focus on the changing shape of the fibre after it emerges from the skin. We present a mechanism to explain the formation of the fibre shape and the factors that affect the process of wool crimping.

One of the possible mechanisms is caused by the physical change of the wool fibres due to water desorption after fibres emerge from the skin. This causes lateral contraction across the cross-section of the fibres. The various types of cells inside the fibres have different physical properties and different amounts of longitudinal extensions are induced across the fibres, which leads to the curving shape of fibres. This mechanism and the fibre shapes are greatly affected by the cross-sectional pattern along the fibres. The internal structure of wool fibres is shown in Figure 3. Also, the mechanism will be explained in more detail in this chapter. The formulation of the full mathematical model is described in the next chapter.

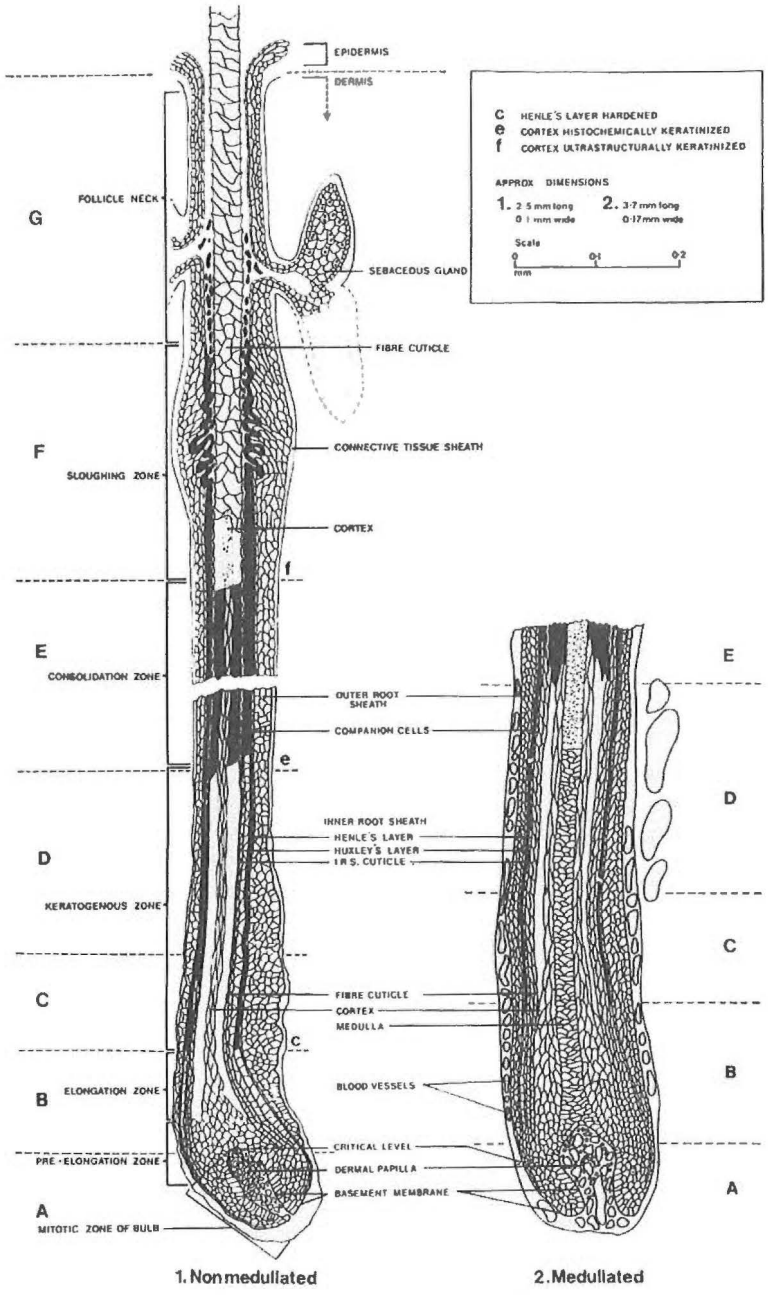

Figure 3: Diagram of the inner structure of wool follicle (From [17])

2.2 Mechanism of wool crimping

A study of a typical cross section of wool fibre shows there are several types of cells in the cortex. The three main types of cortices are called the **ortho-cortex**, **para-cortex** and **meso-cortex**. Figure 4 depicts the microfibrillar structure under the cortex and Figure 5 is a transmission electron microscopy (TEM) image of a cross-section of a wool fibre. Figures 6, 7 and 8 are enlargements that show the ultra-structure within the different types of macrofibrils (refer to [11]).

Within the cortex, macrofibrils are found. Macrofibrils appear as bundles of an ultra-structure called microfibrils or **intermediate filaments** (IFs) that are embedded in sulphur-rich matrix cells of fibre. In each macrofibril of the ortho-cortex, it is clear that whorl patterns of IFs are formed (refer to Figure 6). This observation suggests that the ortho-cortical IFs are packed as concentric helices inside the macrofibrils. Recent work done by Jonathan Caldwell, the author of [6], of Canesis also gives supporting evidence for the above suggestion (refer to Figure 9). From Figures 7 and 8, in contrast, the macrofibrils in the meso-cortex have predominantly hexagonal arrays of IFs and the macrofibrils in the para-cortex indicate a near-hexagonal array along with a lower density of IFs.

When a wool fibre emerges from the skin, water in the matrix of the cortical cells is lost, and this causes the fibre to shrink laterally. This dehydration induces an imbalance of forces and different strains across the wool fibre due to the different structure and properties of the cortical cells. Thus, the fibre must change its shape to restore equilibrium. The connection between the bilateral structure of the cortex and the formation of crimp is discussed by several authors (e.g. [9], [10], [15], [18]).

The simplest model mimics a bimetallic strip. The fibre is regarded as a cylinder with two components corresponding to the ortho-cortex and para-cortex. The ortho-cortex and para-cortex are treated as homogeneous materials having different mechanical properties. Hence the two materials develop

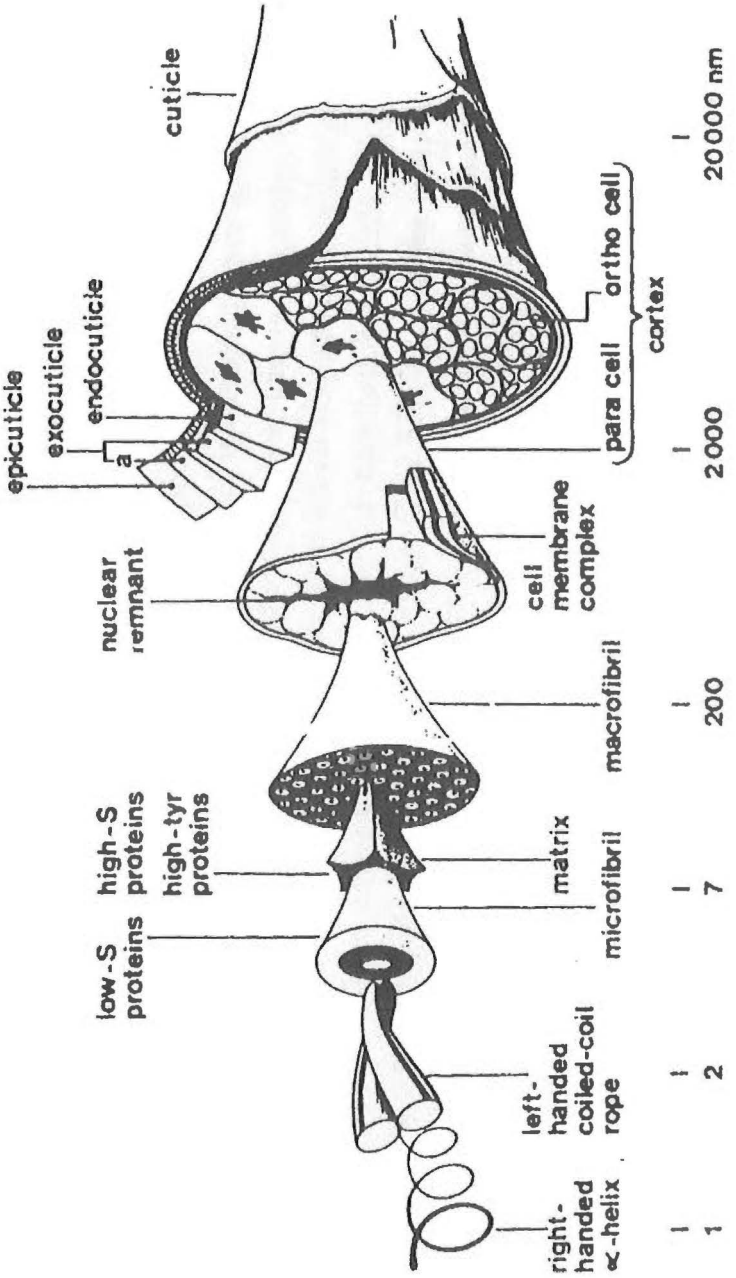

Figure 4: Diagram of the microfibrillar structure of wool follicle (Figure provided by Canesis)

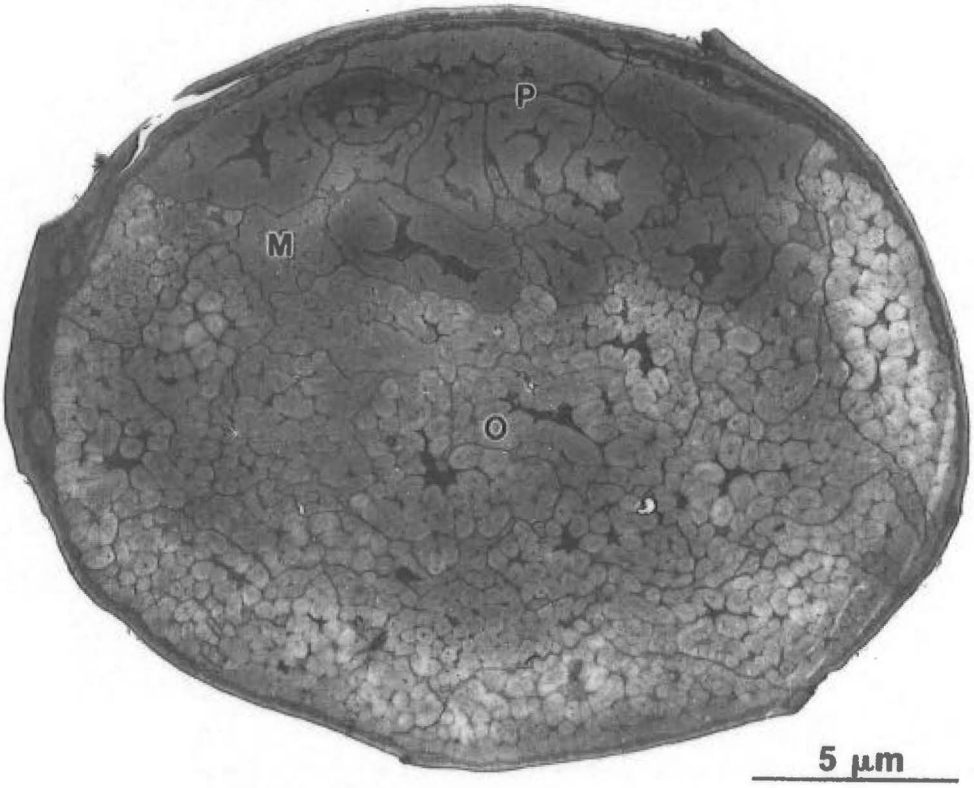

Figure 5: Transverse section from transmission electron microscopy (Figure provided by Canesis)

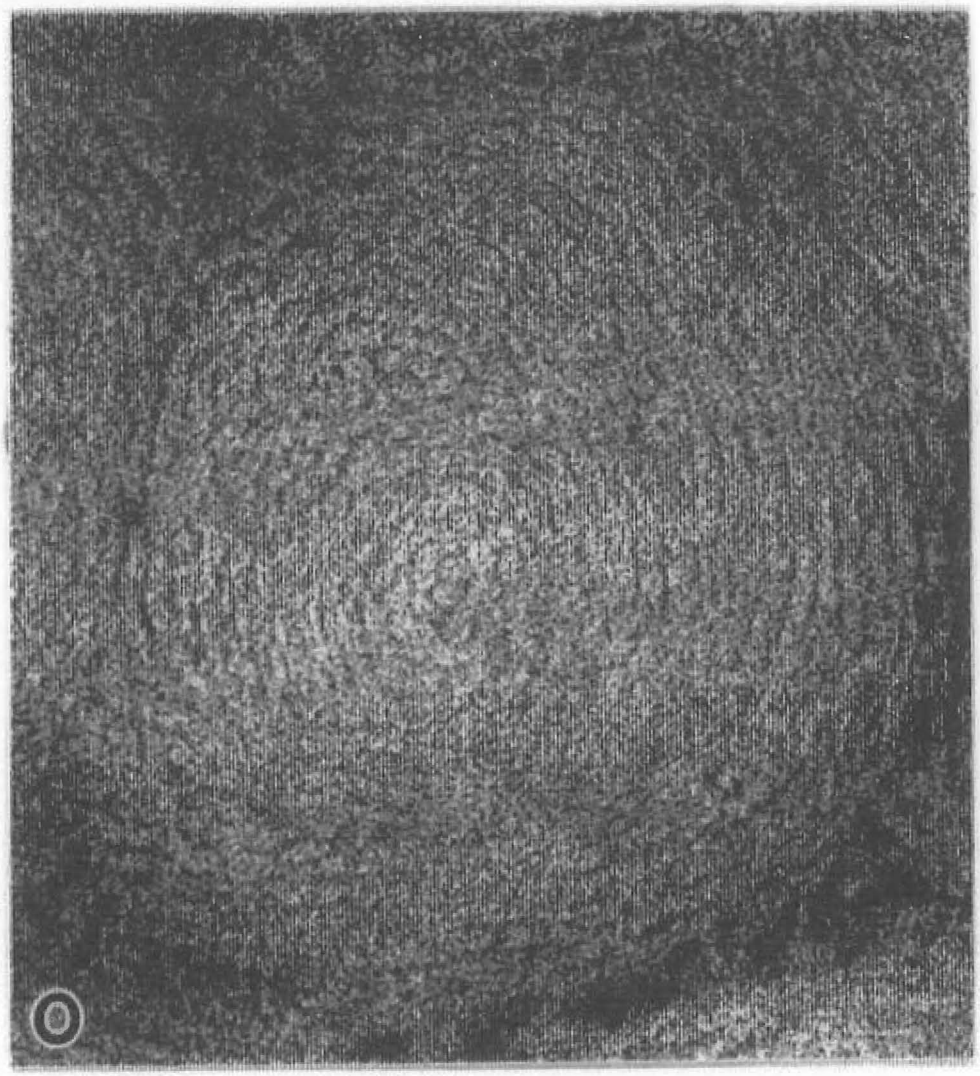

Figure 6: TEM image of ortho-cortical macrofibril (Figure provided by Canesis)

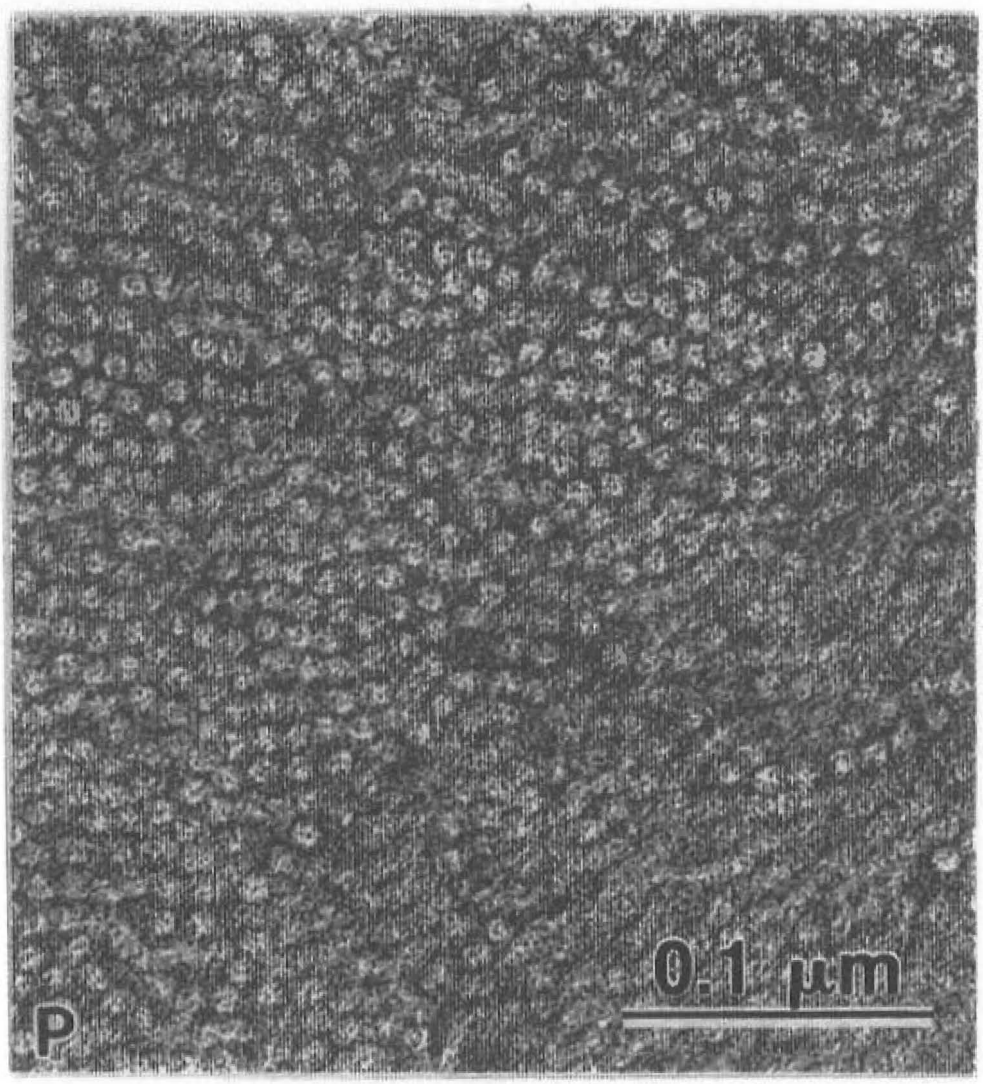

Figure 7: TEM image of para-cortical macrofibril (Figure provided by Canesis)

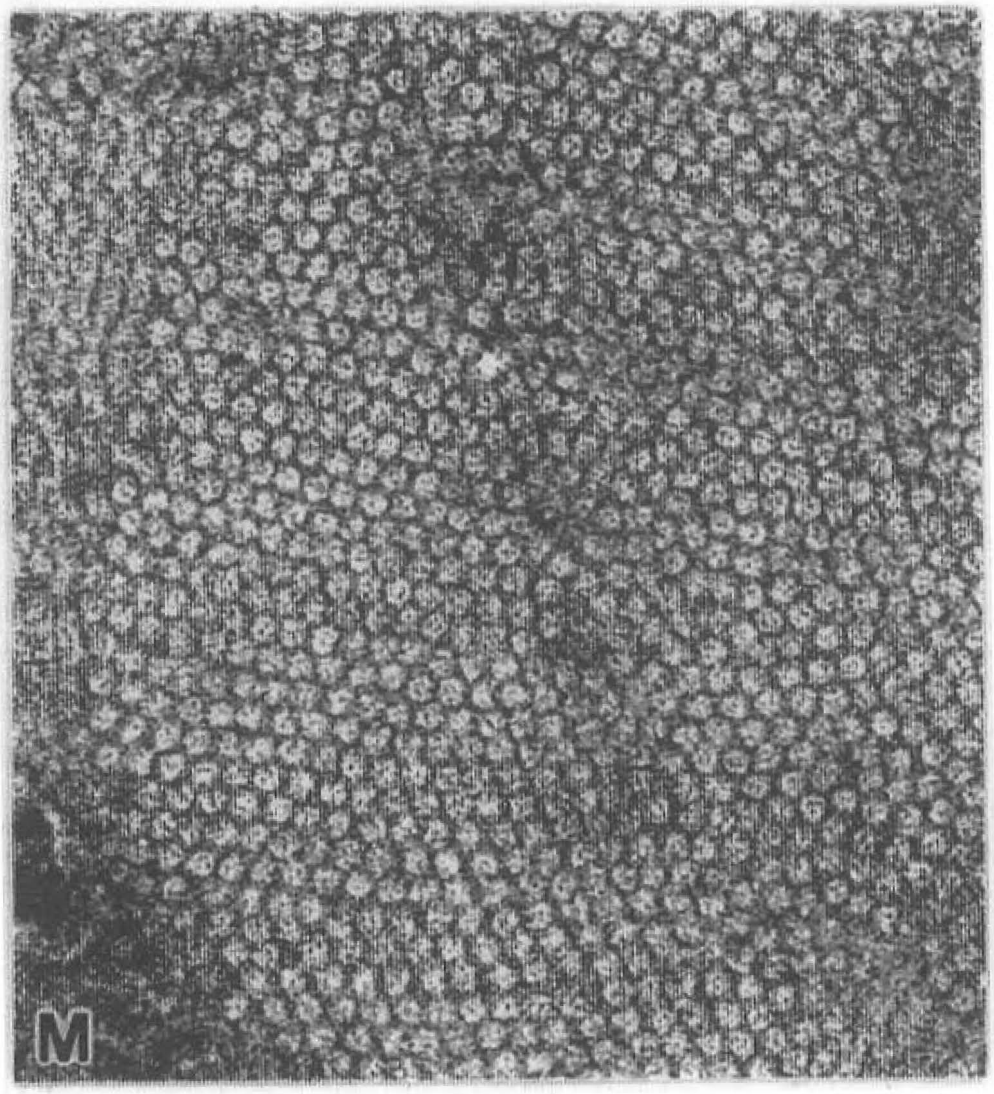

Figure 8: TEM image of meso-cortical macrofibril (Figure provided by Canesis)

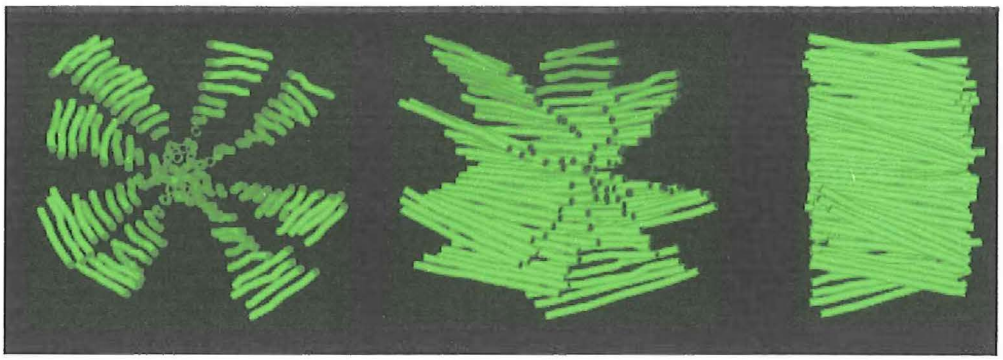

Figure 9: Images of ortho-cortical microfibrils constructed with TEM

differential strains under lateral shrinkage and the shape of fibre corresponds to that which minimises strain energy (c.f. [3] and [20]). A similar model having several components is discussed in [4]. These models ignore the ultra-structure in the cortical cells.

In Munro and Carnaby [16], the authors demonstrate an ortho-cortical macrofibril model which is considered as a regular cylinder filled with concentric helices (IFs) in the wet strain free state (refer to Figure 10). When water desorption starts, the cylinder shrinks laterally and the helices inside elongate in the longitudinal direction. The helices near the centre have a smaller pitch angle than those near the cuticle, and it is assumed that there is no dislocation between the helices. The lateral shrinkage forces the arc lengths of the helices to extend or contract and hence cause an imbalance of strain across the macrofibril. The resulting fibre shape is found by minimising the strain energy of the macrofibril. In the paper, the deformed geometry of a wool fibre is able to be found by putting several macrofibril models together and use finite elements to calculate the minimum strain energy in the wool fibre.

After fibre emerged from the skin, water stored in the matrix cells starts to be lost. This causes lateral contraction and the radius of the fibre decreases

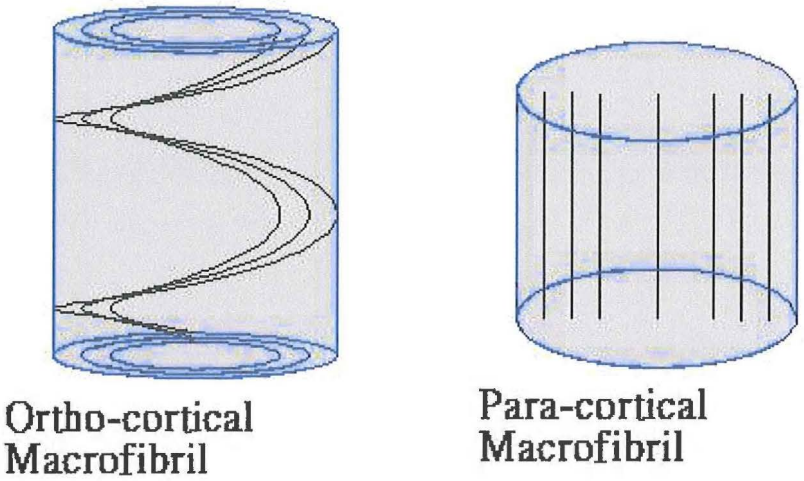

Figure 10: The model of the macrofibril in wet state

evenly. Because of the different geometry of the IFs in different cortices, an imbalance of forces induces across the cross-section of the fibre. The helical ortho-cortical IFs are squashed in the radii while there is no effect to the rod-like para-cortical and meso-cortical IFs. With the reduction of radius, a helix has to increase the length in axial direction to prevent the contraction of arc length. This helps the helix remain in a strain free state. If shear between the IFs arises, all the IFs can stay in a strain free state by extending into different longitudinal lengths and the fibre is straight in this case. However, no or nearly no shear exists between the IFs, it is impossible for the IFs to remain in a strain free state. Hence, the fibre has to deform into a shape that attains a minimum strain energy state.

In this thesis, the idea of Munro and Carnaby is used and extended. Here again the structural elements of the fibre are the IFs, which are represented by a collection of distinct helices in the ortho-cortex and rods in the meso- and para-cortices. Matrix cell structure is omitted in the mathematical model,

so that the mechanical effect of the matrix is neglected. It is assumed that prior to desorption, the fibre is a regular cylinder and that all the IFs are strain free. A reference curve is used to define the shape of the fibre, and the "outputs" of the model describe the shape (in terms of curvature κ, torsion τ, strain ρ and the direction of bending θ) of the reference curve (refer to Figure 11).

Actual fibres always show irregular shape with varying curvature and torsion. It is hypothesised that this is caused by the continuously changing cross-section of the fibre as one moves down the fibre. For simplicity, it is assumed here that the cellular pattern (and hence pattern of IFs) does not change along the length of the fibre. Thus, each transverse cross-section is identical except for its position and orientation and the local shape of the distorted fibre can be determined. Desorption causes these planes to dilate, and this reduces the radii of the helical ortho-cortical IFs. It is assumed that, other than the dilation, the IFs do not shear through the transverse planes. Hence, the deformed fibre still consists of identical cross-sectional planes, but in general the curvature and torsion of the reference curve are non-zero and this means that these planes are inclined and rotated with respect to each other. By neglecting any end effects (alternatively consider an infinitely long fibre), the homogeneity of cross-sectional plane implies that curvature and torsion are constant along the fibre's length; consequently, the fibre will be the shape of a helix. If the cross-section patterns are measured along the fibre, the local deformed shape along the fibre can be described by curvature and torsion.

2.3 Simple examples

In the remainder of this chapter, three simple examples are given that demonstrate the geometry and highlight the importance of the torsion term. Only some simple results are given as follow, the detail mathematical equations and their formulations are given in Chapter 3.

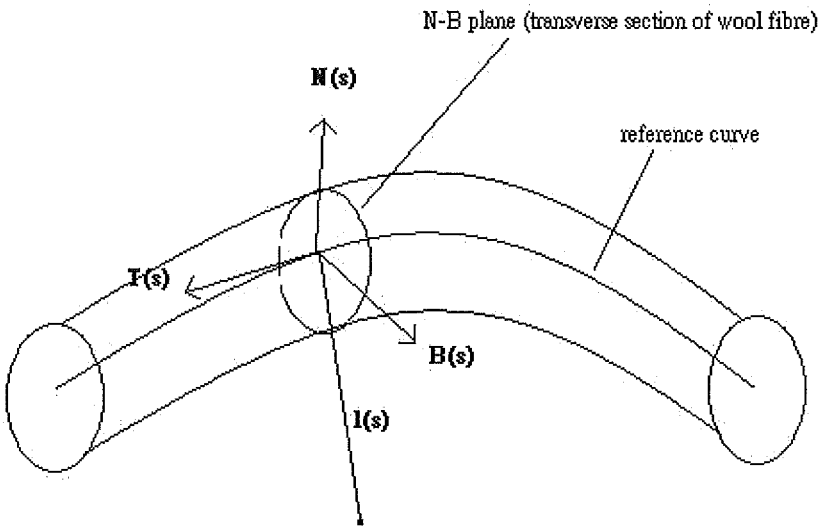

Figure 11: Reference curve $l(s)$ in the N-B plane

2.3.1 1 helix and 1 rod example

The simplest model consists of only one helix and one rod. It is a special example because the final deformed state of the fibre can be achieved with zero strain energy. Further, there is a continuum (1-D) of such solutions and, in this case, the minimum strain energy solution is not unique. The locus of the zero strain energy solution for various values of curvature and torsion is given in Figure 12. Two special, illustrative cases are studied where the fibre deforms to 1) a torsion-free circular arc (refer to Figure 13) and 2) a curvature-free, straight but twisted cylinder (refer to Figure 14). If we choose any solution between the curvature free solution and the torsion free solution on the locus of the zero energy solution on Figure 12, then the reference curve will sweep a circular helix with non zero curvature and torsion, locally to this point on the fibre.

2.3.2 Long and short rods model

If the torsion is identically zero on a curve then it must be a plane curve. Generally, real fibres are space curves that have non zero torsion. A model for fibre shape must therefore include both curvature and torsion. A wool fibre can be modelled as a cylinder containing a collection of helices and rods. Under lateral contraction, the helices stretch longitudinally to prevent a change of arc length, which will induce strain energy in the helices. In a strain free state, the helices will have an elongated longer longitudinal length. One can simplify the model by replacing the helices with rods, which are called "long rods". Now, by hypothesis, there is no shear across the transverse plane, hence, the long rods are compressed and short rods are extended in the axial direction. The fibre assumes the shape that corresponds to minimum total strain energy. The formulation of the model is shown in appendix B.

To illustrate the role of torsion, consider two simple examples with three components and which can be imagined as tri-metallic stripes. The first one

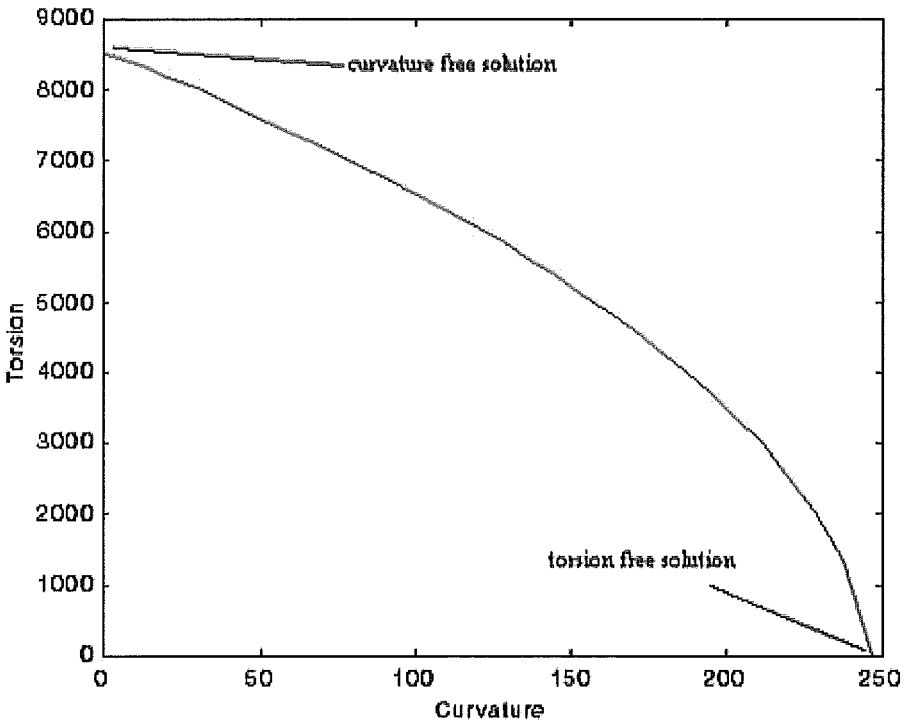

Figure 12: Continuum solutions of strain free dry wool fibre

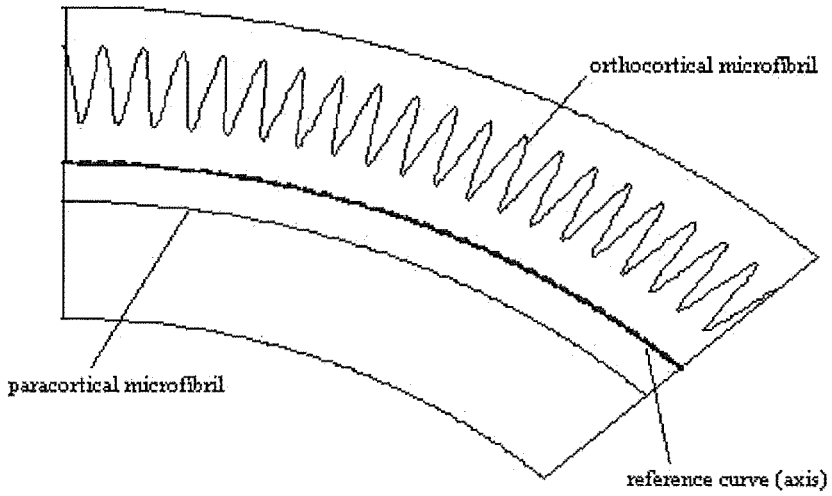

Figure 13: Dry, strain free, torsion free wool fibre

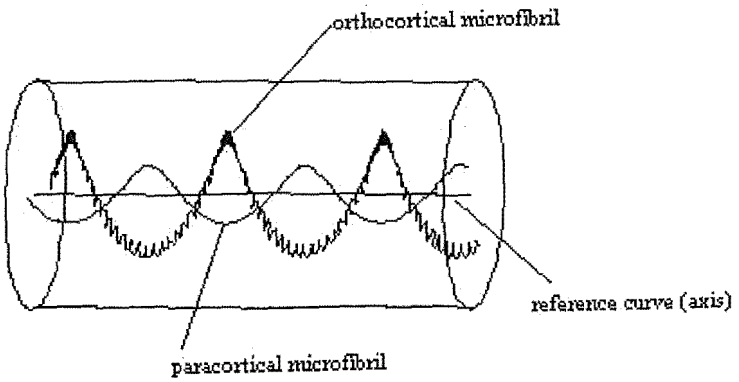

Figure 14: Dry, strain free and curvature free wool fibre

consists of two long rods and one short rod (LLS model) and the second one consists of one long rod and two short rods (LSS model). The energy contours are given in Figures 15 and 16, where the red colour means higher energy value and the dark blue means lower energy value. From the energy contours, LLS model has a single local minimum with positive curvature and zero torsion; LSS model has three critical points with same value of curvature, which include two local minima with a positive and negative torsion respectively and a saddle point at zero torsion. Hence, the LLS model deforms to a planar curve and the LSS model will deform to a right-handed or left-handed helix. The cause of the different results of these two models is not sure but the number of the short rods is suggested to be a possible reason.

2.3.3 Simple helices and rods model

To understand more about the role of torsion, one more simple example is given in this section. Consider a fibre filled with a small number of helices and rods in a 50:50 bilateral pattern, if lateral contraction is applied and minimises the strain energy of the fibre with respect to the four variables curvature κ, torsion τ, strain ρ and the bending direction θ, the shape of the fibre that minimises strain energy gives

$$\begin{aligned} \kappa &= 1.88 \text{ mm}^{-1} , \\ \tau &= 8.28 \text{ mm}^{-1} , \\ \rho &= 1.01 , \\ \theta &= \frac{3\pi}{2} \text{ rad} , \\ e &= 1.88 \times 10^{-16} \text{ J} . \end{aligned}$$

Since the Young's modulus of a single IF is unknown (here it is taken as unity in the appropriate units), the strain energy e (measured in Joules) is just an arbitrary value. More detail is provided in the next chapter. If

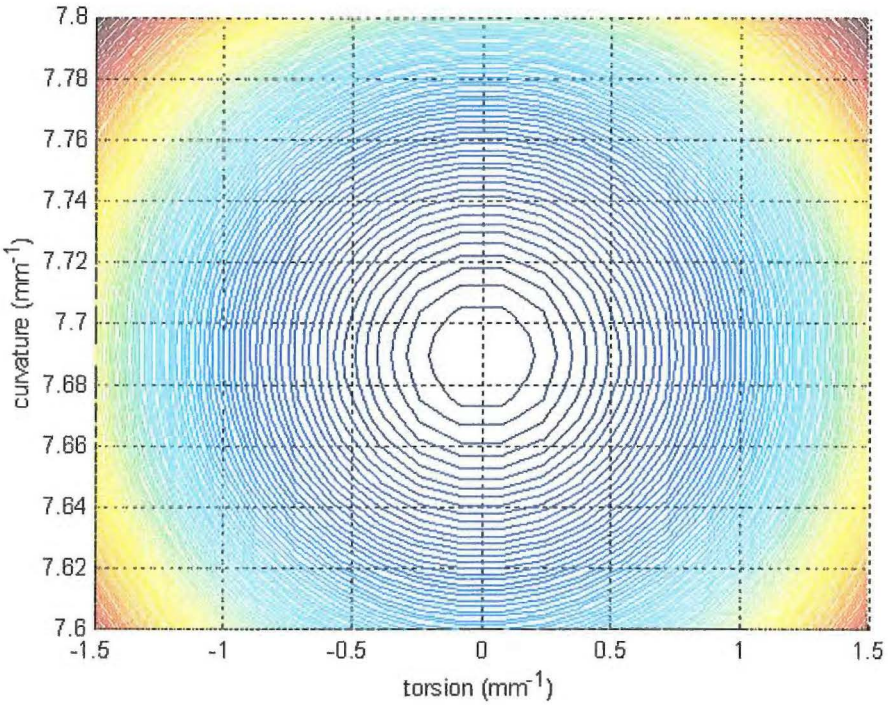

Figure 15: Energy contour plot of LLS model

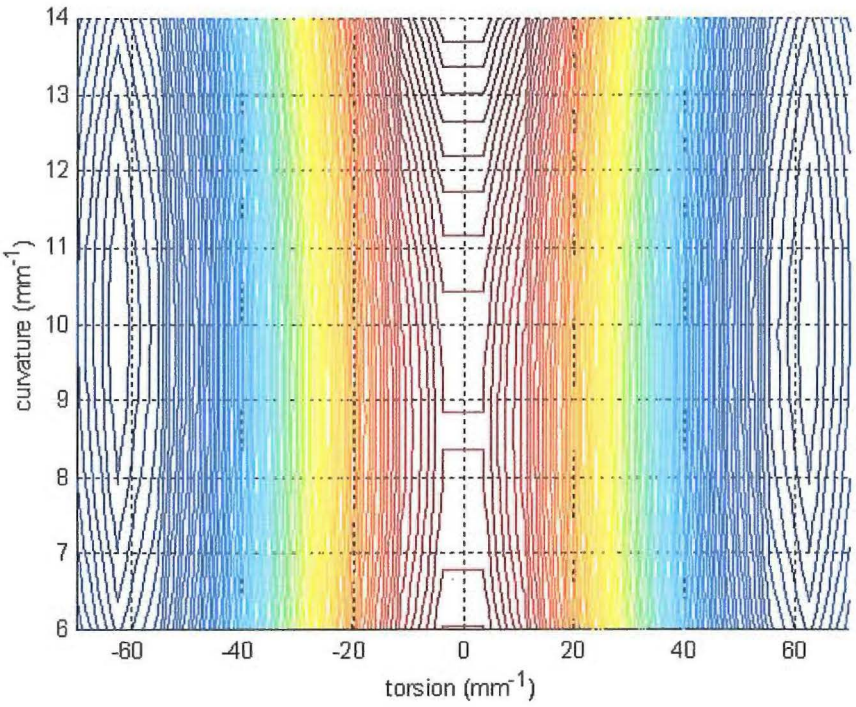

Figure 16: Energy contour plot of LSS model

it is compared with a planar curve fibre with the same amount of strain and curvature but with zero torsion, the calculated strain energy $e = 2.40 \times 10^{-16}$ J. It is greater than the original energy minimised state of the fibre. This result shows that curvature is not the only factor in the minimisation process. A fibre bent into a planar curve (zero torsion) can achieve a lower energy state by increasing torsion value. We minimise the same configuration of fibre with respect to κ, ρ and θ only and keep $\tau = 0$. This minimisation yields

$$\begin{aligned} \kappa &= 1.91 \text{ mm}^{-1} , \\ \tau &= 0 \text{ mm}^{-1} , \\ \rho &= 1.01 , \\ \theta &= \frac{3\pi}{2} \text{ rad} , \\ e &= 2.05 \times 10^{-16} \text{ J} , \end{aligned}$$

which gives strain energy higher than for non-zero torsion. For this example, torsion is important because the fibre achieves a lower energy state when $\tau \neq 0$.

3 Basic Model

3.1 Introduction

In this chapter, a model is presented where intermediate filaments are represented by helices and rods in the basic model, but the macrofibrillar structure of the ortho-cortex is ignored or it can be considered as a simplified model as shown in Figure 17 (compare with Figure 10). The ortho-cortical IFs are represented by isolated single helices, which do not group together about a common axis. Para-cortical and meso-cortical IFs are represented by single rods (refer to Figure 18). These assumptions simplify the analysis and computation, and reduce the number of parameters in the model. Even without the macrofibrillar structure, the use of individual helices yields reasonable predictions for the deformed shape of the wool fibre when compared with the experimental results.

In this chapter we formulate and solve a mathematical model that estimates the deformed shape of a wool fibre with a given MOP (Meso-ortho-para-cortex) pattern. The sensitivity of the results on the model's parameters is demonstrated. A more realistic model that incorporates the cuticle is also studied. Finally, an analytical solution is presented in the last section after first simplifying the basic model via Taylor's expansions.

3.2 The mathematical model

The wool fibre is assumed to be prismatic, i.e., all its cross-sections have an identical MOP pattern. Let L denote the length in the wet state. Given a MOP pattern, non-overlapping helices with radius r, pitch angle ϕ and axial length L are placed in the ortho-cortical region. Rods of length L are placed in the para-cortical and meso-cortical regions. From observation (refer to Figures 7 and 8), the density of IFs in the meso-cortex is about two to three times higher than in the para-cortex. Therefore, it is assumed that the only

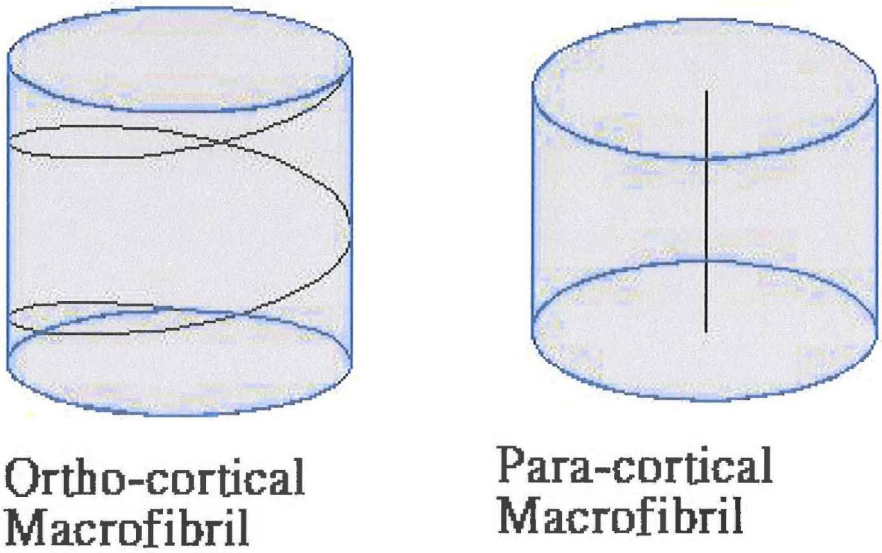

Figure 17: Simplified model of the macrofibril in wet state

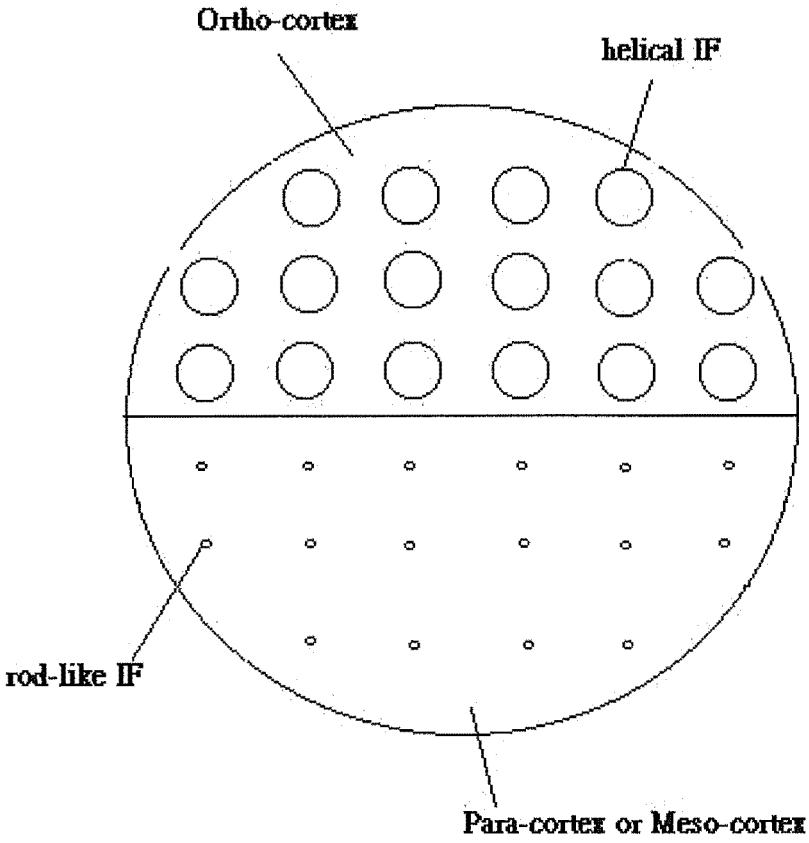

Figure 18: Example of a cross section of a wool fibre displaying isolated helical ortho-cortical IFs and isolated rod like para- or meso-cortical IFs in a bilateral split.

difference between the meso-cortical and para-cortical IFs is that the former is twice as densely packed. The centres of the IFs are placed on the fibre's cross section at the vertices of a square lattice as in Figure 18.

During desorption from the wet to dry state it is assumed there is no delocation of the IF and no shearing forces, so the MOP pattern is preserved and the radial scale simply decreases by a factor of $(1-\gamma) < 1$. All the lengths on the cross-section are then scaled: in particular if the wool fibre has initial radius R_w then its radius after desorption is $\tilde{R}_w = (1-\gamma)R_w$, and the radius of a helical IFs will shrink from r to $\tilde{r} = (1-\gamma)r$ (refer to Figure 19). This shrinkage may reduce the arc length of the ortho-cortical IFs with the no shearing assumption, which would increase their strain energy. This scenario would induce the system to bend and twist in order to achieve a minimum energy state.

Let $\mathbf{l}(s)$ denote the vector to the axis of the wool fibre. This curve is called the reference curve and is used to describe the shape of the fibre. Here s is the arc length. Four variables describe the deformed geometry of the reference curve: $\kappa(s)$ is the curvature of $\mathbf{l}(s)$; $\tau(s)$ is the torsion of $\mathbf{l}(s)$; $\theta(s)$ is the angle between the principal normal vector of $\mathbf{l}(s)$ and some reference vector on the cross-section called the "datum line"; and $\rho(s)$ parameterises the strain of arc length of $\mathbf{l}(s)$. The geometry of space curves is reviewed in Appendix A along with some comments about prismatic fibres.

By construction, the cross-sectional plane is coincident with the normal plane defined by the principal normal $\mathbf{N}(s)$ and binormal $\mathbf{B}(s)$ of $\mathbf{l}(s)$ at each s (refer to Figure 11 and appendix A). Because the fibre is prismatic under the assumptions of the model, $\kappa(s)$, $\tau(s)$, $\rho(s)$ and $\theta(s)$ are constant. The parameter ρ is nondimensionalised so that if L is the original arc length of $\mathbf{l}(s)$ then the deformed arc length after desorption is $\tilde{L} = \rho L$.

Let n_{o} be the number of ortho-cortical IFs, n_{m} be the number of meso-cortical IFs and n_{p} be the number of para-cortical IFs. The positions of the ortho-cortical IFs on the wool fibre cross-section are parameterised by the set

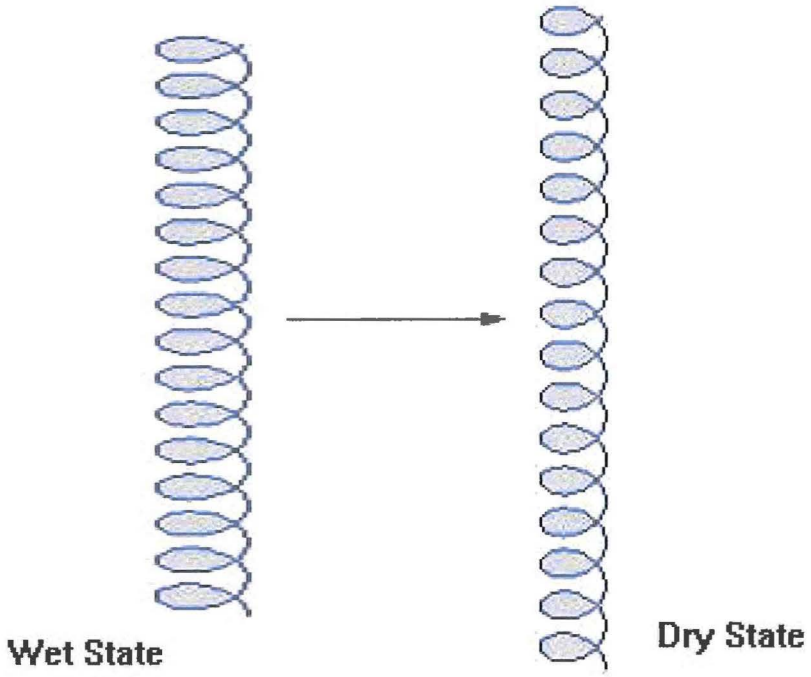

Figure 19: The change of a strain free helix when fibre shrinkage

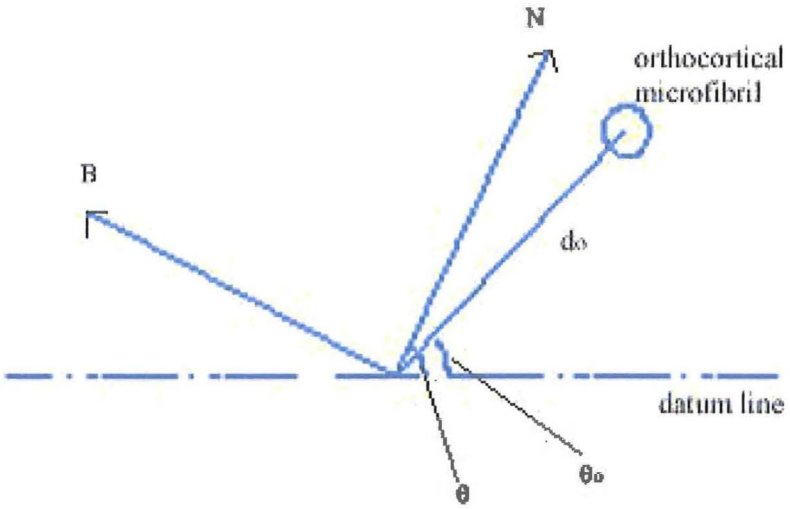

Figure 20: Cross-sectional area in N-B plane

$(d_{\rm o}^i, \theta_{\rm o}^i)$, with $i \in \{1, n_{\rm o}\}$, where $d_{\rm o}^i$ is the length of the vector from the axis of the wool fibre to the $i^{\rm th}$ ortho-cortical IF and $\theta_{\rm o}^i$ is the angle between this vector and the datum line (refer to Figure 20). Similarly, the positions of a meso-cortical or para-cortical IFs are respectively $(d_{\rm m}^i, \theta_{\rm m}^i)$ with $i \in \{1, n_{\rm m}\}$, and $(d_{\rm p}^i, \theta_{\rm p}^i)$ with $i \in \{1, n_{\rm p}\}$.

3.2.1 Strain energy of a deformed para-cortical IF

Denote the position (in global coordinates) of a para-cortical IF by $\mathbf{h}_{\rm p}^i(s)$

$$\mathbf{h}_{\rm p}^i(s) = \mathbf{l}(s) + \tilde{d}_{\rm p}^i \cos(\theta_{\rm p}^i - \theta)\mathbf{N}(s) + \tilde{d}_{\rm p}^i \sin(\theta_{\rm p}^i - \theta)\mathbf{B}(s) \ , \qquad (3.1)$$

where $\tilde{d}_{\rm p}^i = (1-\gamma)\, d_{\rm p}^i$. Since the undeformed arc length of a para-cortical IF is $L_{\rm p}^i = L$, the deformed length $\tilde{L}_{\rm p}^i$ is

$$\tilde{L}_{\rm p}^i = \int_0^{\rho L} \left| \frac{{\rm d}\mathbf{h}_{\rm p}^i}{{\rm d}s} \right| {\rm d}s \ .$$

Using the Frenét formulae (see Equation (A.15) in Appendix A)

$$\begin{aligned}
\frac{{\rm d}\mathbf{h}_{\rm p}^i}{{\rm d}s} &= \frac{{\rm d}\mathbf{l}}{{\rm d}s} + \tilde{d}_{\rm p}^i \cos(\theta_{\rm p}^i - \theta)\frac{{\rm d}\mathbf{N}}{{\rm d}s} + \tilde{d}_{\rm p}^i \sin(\theta_{\rm p}^i - \theta)\frac{{\rm d}\mathbf{B}}{{\rm d}s} \\
&= \mathbf{T}(s) + \tilde{d}_{\rm p}^i \cos(\theta_{\rm p}^i - \theta)\left(-\kappa\mathbf{T}(s) + \tau\mathbf{B}(s)\right) + \tilde{d}_{\rm p}^i \sin(\theta_{\rm p}^i - \theta)\left(-\tau\mathbf{N}(s)\right) \\
&= \left(1 - \tilde{d}_{\rm p}^i \kappa \cos(\theta_{\rm p}^i - \theta)\right)\mathbf{T}(s) + \tilde{d}_{\rm p}^i \tau \cos(\theta_{\rm p}^i - \theta)\mathbf{B}(s) - \tilde{d}_{\rm p}^i \tau \sin(\theta_{\rm p}^i - \theta)\mathbf{N}(s) \ ;
\end{aligned}$$

hence,

$$\begin{aligned}
\left| \frac{{\rm d}\mathbf{h}_{\rm p}^i}{{\rm d}s} \right|^2 &= \left(1 - \tilde{d}_{\rm p}^i \cos(\theta_{\rm p}^i - \theta)\kappa\right)^2 + \left(\tilde{d}_{\rm p}^i \cos(\theta_{\rm p}^i - \theta)\tau\right)^2 + \left(\tilde{d}_{\rm p}^i \sin(\theta_{\rm p}^i - \theta)\tau\right)^2 \\
&= \left(1 - \tilde{d}_{\rm p}^i \cos(\theta_{\rm p}^i - \theta)\kappa\right)^2 + \left(\tilde{d}_{\rm p}^i \tau\right)^2 .
\end{aligned}$$

The deformed arc length of a para-cortical IF is thus

$$\begin{aligned}\tilde{L}^i_{\mathrm{p}} &= \int_0^{\rho L} \sqrt{\left(1-\tilde{d}^i_{\mathrm{p}}\cos(\theta^i_{\mathrm{p}}-\theta)\kappa\right)^2+\left(\tilde{d}^i_{\mathrm{p}}\tau\right)^2}\mathrm{d}s \\ &= \rho L\sqrt{\left(1-\tilde{d}^i_{\mathrm{p}}\cos(\theta^i_{\mathrm{p}}-\theta)\kappa\right)^2+\left(\tilde{d}^i_{\mathrm{p}}\tau\right)^2}. \end{aligned} \tag{3.2}$$

The strain energy of a single para-cortical IF is

$$\begin{aligned} e^i_{\mathrm{p}} &= \int_{A_{\mathrm{p}}} \frac{1}{2}E_{\mathrm{p}}L^i_{\mathrm{p}}\left(\frac{L^i_{\mathrm{p}}-\tilde{L}^i_{\mathrm{p}}}{L^i_{\mathrm{p}}}\right)^2 \mathrm{d}A \\ &= \frac{1}{2}\frac{E_{\mathrm{p}}A_{\mathrm{p}}}{L^i_{\mathrm{p}}}\left(L^i_{\mathrm{p}}-\tilde{L}^i_{\mathrm{p}}\right)^2, \end{aligned} \tag{3.3}$$

where E_{p} is the Young's modulus and A_{p} is the transverse cross-sectional area of the para-cortical IF.

3.2.2 Strain energy of a deformed meso-cortical IF

The deformed length $\tilde{L}^i_{\mathrm{m}}$ of a single meso-cortical IF can be found in a similar manner; thus

$$\begin{aligned}\tilde{L}^i_{\mathrm{m}} &= \int_0^{\rho L} \sqrt{\left(1-\tilde{d}^i_{\mathrm{m}}\cos(\theta^i_{\mathrm{m}}-\theta)\kappa\right)^2+\left(\tilde{d}^i_{\mathrm{m}}\tau\right)^2}\mathrm{d}s \\ &= \rho L\sqrt{\left(1-\tilde{d}^i_{\mathrm{m}}\cos(\theta^i_{\mathrm{m}}-\theta)\kappa\right)^2+\left(\tilde{d}^i_{\mathrm{m}}\tau\right)^2}, \end{aligned}$$

where $\tilde{d}^i_{\mathrm{m}} = (1-\gamma)d^i_{\mathrm{m}}$. The strain energy is

$$e^i_{\mathrm{m}} = \frac{1}{2}\frac{E_{\mathrm{m}}A_{\mathrm{m}}}{L^i_{\mathrm{m}}}\left(L^i_{\mathrm{m}}-\tilde{L}^i_{\mathrm{m}}\right)^2, \tag{3.4}$$

where E_{m} is the Young's modulus and A_{m} is the transverse cross-sectional area of the meso-cortical IF. Note that the equations of the para-cortical and the meso-cortical IFs are mathematically identical. They are identified separately instead of using helices and rods because the densities of the IFs

are different in the para- and meso-cortex. Consider a symmetrical pattern with purely para- or meso-cortex as in Figure 18, the direction of bending will be straight downward (i.e. $\theta = \frac{3\pi}{2}$). If the bottom half of the cross-section is replaced by a mixture of para- or meso- cortex, the direction of bending can be any direction downward (i.e. $\pi < \theta < 2\pi$). Just using helices and rods to clarify the different regions will therefore not be sufficient to describe the differences of the cross-section patterns of these cases.

3.2.3 Strain energy of a deformed ortho-cortical IF

Deriving the deformed length of an ortho-cortical IF is more complicated because it forms a "helix within a helix". Let the vectors $\mathbf{g}_{\mathrm{o}}^{i}(s)$ and $\mathbf{h}_{\mathrm{o}}^{i}(s)$ represent the positions (in global coordinates) of the generating curve (axis) of a helical ortho-cortical IF and the helical ortho-cortical IF itself. That is,

$$\mathbf{g}_{\mathrm{o}}^{i}(s) = \mathbf{l}(s) + \tilde{d}_{\mathrm{o}}^{i}\cos(\theta_{\mathrm{o}}^{i} - \theta)\mathbf{N}(s) + \tilde{d}_{\mathrm{o}}^{i}\sin(\theta_{\mathrm{o}}^{i} - \theta)\mathbf{B}(s) \ ,$$

with $\tilde{d}_{\mathrm{o}}^{i} = (1-\gamma)d_{\mathrm{o}}^{i}$, and

$$\begin{aligned}
\mathbf{h}_{\mathrm{o}}^{i}(s) &= \mathbf{g}_{\mathrm{o}}^{i}(s) + \tilde{r}\cos(\omega s - \theta)\mathbf{N}(s) + \tilde{r}\sin(\omega s - \theta)\mathbf{B}(s) \\
&= \mathbf{l}(s) + \left(\tilde{d}_{\mathrm{o}}^{i}\cos(\theta_{\mathrm{o}}^{i} - \theta) + \tilde{r}\cos(\omega s - \theta)\right)\mathbf{N}(s) \\
&\quad + \left(\tilde{d}_{\mathrm{o}}^{i}\sin(\theta_{\mathrm{o}}^{i} - \theta) + \tilde{r}\sin(\omega s - \theta)\right)\mathbf{B}(s) \ .
\end{aligned}$$

The product ωs shifts by 2π under one complete turn of the IF. After desorption the model assumes

$$\omega = \frac{\tan\phi}{\rho r} \ ,$$

which is an average value over one complete turn. This is derived as follows. Let n_{turn} be the number of turns of a helical IF in the fibre. By assumption it is conserved during desorption. The length traversed along the generating curve of the helical IF while the IF-helix completes one cycle with pitch angle

ϕ is

$$\frac{L}{n_{\text{turn}}} = \frac{2\pi r}{\tan\phi}; \qquad \text{therefore,} \qquad n_{\text{turn}} = \frac{L\tan\phi}{2\pi r} .$$

After desorption, the length L/n_{turn} will expand to $\rho L/n_{\text{turn}}$. Therefore,

$$\omega\left(\frac{\rho L}{n_{\text{turn}}}\right) = 2\pi, \qquad \text{and consequently,} \qquad \omega = \frac{2\pi n_{\text{turn}}}{\rho L} = \frac{\tan\phi}{\rho r} .$$

The derivative of $\mathbf{h}_{\text{o}}^{i}(s)$ with respect to s is calculated using the Frenét formulae,

$$\begin{aligned}
\frac{\mathrm{d}\mathbf{h}_{\text{o}}^{i}}{\mathrm{d}s}(s) &= \mathbf{T}(s) + \left(\tilde{d}_{\text{o}}^{i}\cos(\theta_{\text{o}}^{i}-\theta) + \tilde{r}\cos(\omega s-\theta)\right)\left(-\kappa\mathbf{T}(s)+\tau\mathbf{B}(s)\right) \\
&\quad -\tilde{r}\omega\sin(\omega s-\theta)\mathbf{N}(s) + \left(\tilde{d}_{\text{o}}^{i}\sin(\theta_{\text{o}}^{i}-\theta) + \tilde{r}\sin(\omega s-\theta)\right)\left(-\tau\mathbf{N}(s)\right) \\
&\quad +\tilde{r}\omega\cos(\omega s-\theta)\mathbf{B}(s) \\
&= \left[1-\kappa(\tilde{d}_{\text{o}}^{i}\cos(\theta_{\text{o}}^{i}-\theta) + \tilde{r}\cos(\omega s-\theta))\right]\mathbf{T}(s) \\
&\quad -\left[\tilde{r}\omega\sin(\omega s-\theta) + \tau(\tilde{d}_{\text{o}}^{i}\sin(\theta_{\text{o}}^{i}-\theta) + \tilde{r}\sin(\omega s-\theta))\right]\mathbf{N}(s) \\
&\quad +\left[\tilde{r}\omega\cos(\omega s-\theta) + \tau(\tilde{d}_{\text{o}}^{i}\cos(\theta_{\text{o}}^{i}-\theta) + \tilde{r}\cos(\omega s-\theta))\right]\mathbf{B}(s) .
\end{aligned}$$

There,

$$\begin{aligned}
\left|\frac{\mathrm{d}\mathbf{h}_{\text{o}}^{i}}{\mathrm{d}s}\right|^{2} &= \left[1-\kappa(\tilde{d}_{\text{o}}^{i}\cos(\theta_{\text{o}}^{i}-\theta) + \tilde{r}\cos(\omega s-\theta))\right]^{2} \\
&\quad +\left[\tilde{r}\omega\sin(\omega s-\theta) + \tau(\tilde{d}_{\text{o}}^{i}\sin(\theta_{\text{o}}^{i}-\theta) + \tilde{r}\sin(\omega s-\theta))\right]^{2} \\
&\quad +\left[\tilde{r}\omega\cos(\omega s-\theta) + \tau(\tilde{d}_{\text{o}}^{i}\cos(\theta_{\text{o}}^{i}-\theta) + \tilde{r}\cos(\omega s-\theta))\right]^{2} ,
\end{aligned}$$

and the arc length of a deformed ortho-cortical IF is

$$\begin{aligned}
\tilde{L}_{\text{o}}^{i} &= \int_{0}^{\rho L}\left|\frac{\mathrm{d}\mathbf{h}_{\text{o}}^{i}}{\mathrm{d}s}\right|\mathrm{d}s \\
&= \int_{0}^{\rho L}\left(\left[1-\kappa(\tilde{d}_{\text{o}}^{i}\cos(\theta_{\text{o}}^{i}-\theta) + \tilde{r}\cos(\omega s-\theta))\right]^{2}\right.
\end{aligned}$$

$$+\left[\tilde{r}\omega\sin(\omega s-\theta)+\tau(\tilde{d}_{\mathrm{o}}^{i}\sin(\theta_{\mathrm{o}}^{i}-\theta)+\tilde{r}\sin(\omega s-\theta))\right]^{2}$$
$$+\left[\tilde{r}\omega\cos(\omega s-\theta)+\tau(\tilde{d}_{\mathrm{o}}^{i}\cos(\theta_{\mathrm{o}}^{i}-\theta)+\tilde{r}\cos(\omega s-\theta))\right]^{2}\Big)^{\frac{1}{2}}\mathrm{d}s \quad (3.5)$$

The strain energy of a single ortho-cortical IF is

$$e_{\mathrm{o}}^{i}=\frac{1}{2}\frac{E_{\mathrm{o}}A_{\mathrm{o}}}{L_{\mathrm{o}}^{i}}(L_{\mathrm{o}}^{i}-\tilde{L}_{\mathrm{o}}^{i})^{2}\ , \quad (3.6)$$

where E_{o} is the Young's modulus and A_{o} is the transverse cross-sectional area of the helical IF, and $L_{\mathrm{o}}^{i}=L/\cos\phi$ is the original arc length of an ortho-cortical IF.

Although the Young's modulus of the IFs is unknown, all the IFs are considered to be formed with the same material, so the Young's modulus of the IFs is assumed to be the same. The total energy of a wool fibre is

$$e_{\mathrm{w}}(\kappa,\tau,\rho,\theta)=\sum_{i=1}^{n_{\mathrm{o}}}e_{\mathrm{o}}^{i}+\sum_{i=1}^{n_{\mathrm{m}}}e_{\mathrm{m}}^{i}+\sum_{i=1}^{n_{\mathrm{p}}}e_{\mathrm{p}}^{i}\ . \quad (3.7)$$

From the equations (3.3), (3.4) and (3.6), the strain energy of the IFs are proportional to the Young's modulus. If all the IFs are assumed to have the same Young's modulus, the numerical value of the Young's modulus is not important when minimising equation (3.7). The deformed geometry corresponds to a global minimum for e_{w} with respect to κ, τ, ρ and θ.

3.3 Large parameter expansion

Care must be taken to find the global minimum, not a local one, when searching for a minimum numerically. Equations (3.2), (3.3), (3.5) and (3.6) imply that when κ, τ or ρ are large the wool-fibre energy scales quadratically:

$$\lim_{\kappa\to\infty}\frac{e_{\mathrm{w}}}{\kappa^{2}} = 1,$$
$$\lim_{\tau\to\infty}\frac{e_{\mathrm{w}}}{\tau^{2}} = 1,$$

$$\lim_{\rho \to \infty} \frac{e_w}{\rho^2} = 1.$$

The coefficients of the quadratic terms are never zero for any realistic MOP pattern. These observations are useful when numerically finding minima since they effectively limit the search to an area around the origin in $\kappa - \tau - \rho$ space (in fact, the minima are always found near $\rho = 1$). The remaining parameter θ, is compact.

3.4 Results for a fibre

Consider a MOP pattern that consists of ortho-cortex and para-cortex only: the upper half of the cross-section is ortho-cortex and the lower half is para-cortex as shown in Figure 18. The radius of a wet wool fibre is 15 μm, the radius of the helical ortho-cortical IFs, $r = 0.3$ μm and the pitch angle, $\phi = 30°$, which is the observed value of the outermost IFs in a macrofibril. A lateral dilation, $\gamma = 0.1$ is applied as a reasonable guess. There are 3928 ortho-cortical IFs and 1965 para-cortical IFs packed in square lattice pattern. Since the density of IF is lower in para-cortex than in ortho-cortex, therefore, the number of ortho-cortical IFs is higher even the areas of the cortices are the same. From Figures 21, 22 and 23, the number of IF elements used is chosen such that there are enough IF elements to make sure the minimisation converges to the true value. With the number of IFs is less than 1000, there are zig-zag pattern appearing on the figures, which may be caused by the flat bottom of the energy surface near the local minimum. So that, the minimisation can only give approximate values near the true minima due to numerical error. The minimisation is done by an optimising package in Matlab called "fminu". It is a quasi-Newton method with a mixed quadratic and cubic line search procedure.

With this configuration, the numerical simulation calculates the strain energy of the whole wool fibre and then minimises the strain energy. The

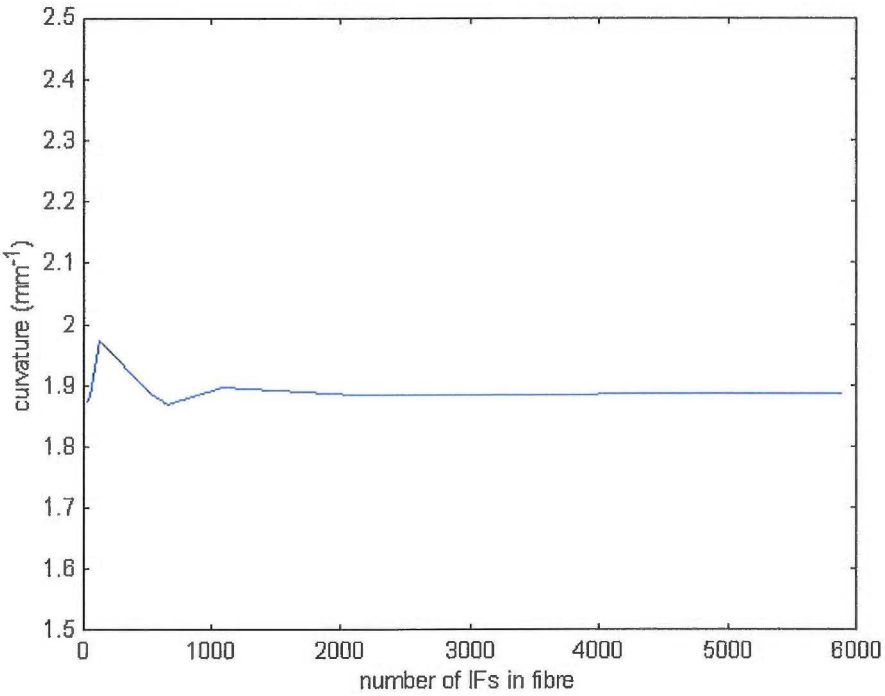

Figure 21: Fibre curvature versus number of IFs in fibre

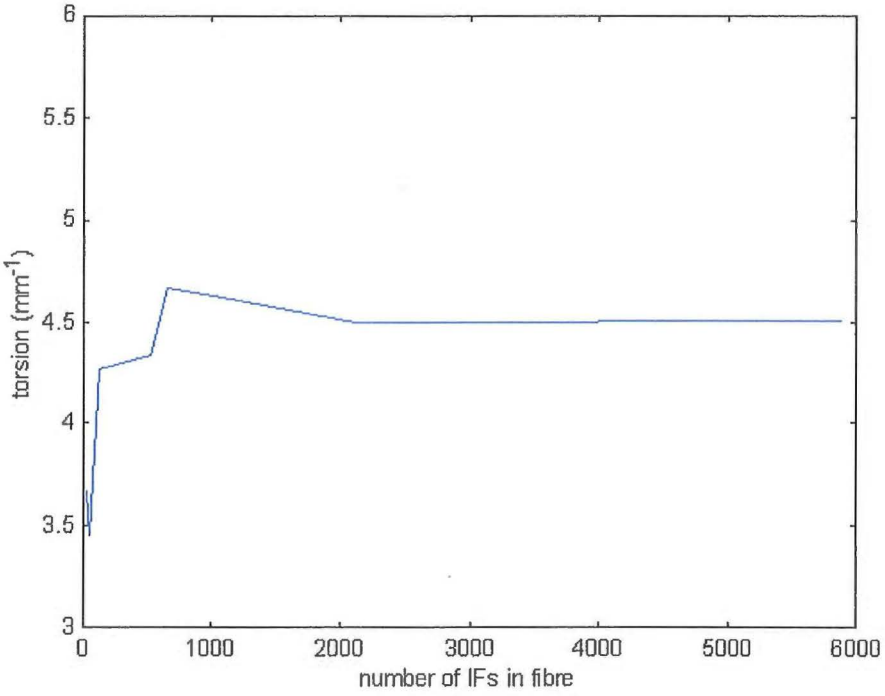

Figure 22: Fibre torsion versus number of IFs in fibre

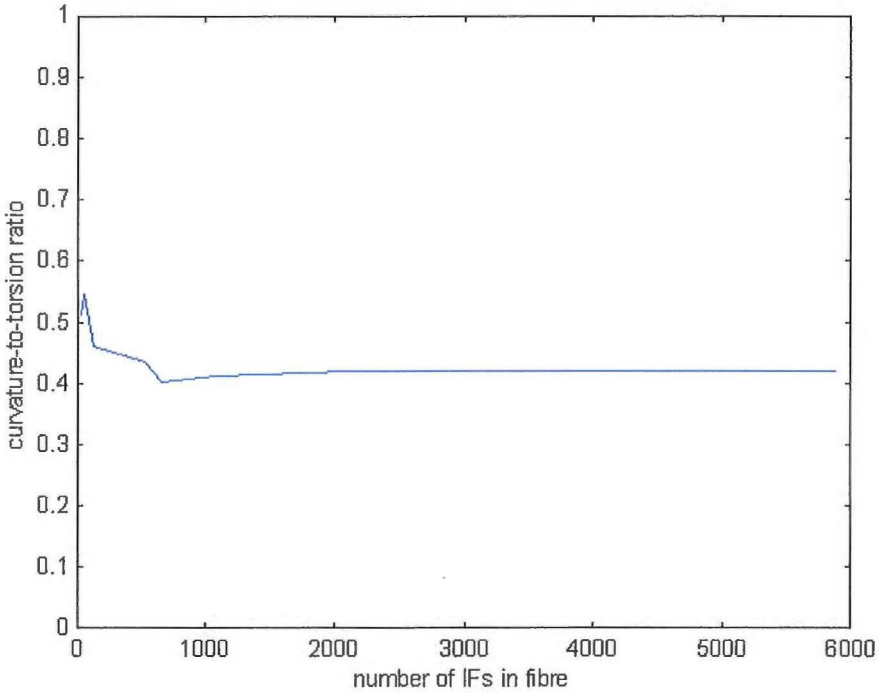

Figure 23: Fibre curvature-to-torsion ratio versus number of IFs in fibre

results from this simulation are

$$\begin{aligned} \kappa &= 1.89 \text{ mm}^{-1} , \\ \tau &= 4.50 \text{ mm}^{-1} , \\ \rho &= 1.02 , \\ \theta &= \frac{3\pi}{2} \text{ rad} , \\ a &= 0.08 \text{ mm} , \\ c &= 1.89 \text{ mm} , \\ \kappa : \tau &= 0.42 , \end{aligned}$$

where a and c are the radius and the pitch distance of the deformed helical reference curve respectively (see Appendix A), i.e.:

$$a = \frac{\kappa}{\kappa^2 + \tau^2} \quad \text{and} \quad c = \frac{\tau}{\kappa^2 + \tau^2} .$$

The global minimum is fairly distinct. The area in which the energy differs from the minimum's energy by less than 1% is approximately bounded by the rectangle

$$1.8 \text{ mm}^{-1} < \kappa < 1.95 \text{ mm}^{-1} \quad \text{and} \quad 2.5 \text{ mm}^{-1} < \tau < 4.5 \text{ mm}^{-1} .$$

The shape of the deformed reference curve is shown in Figure 24.

3.5 Varying the model's parameters

In this section, the effects of varying the model's key parameters are analysed. All the cases below are based on the configuration of Section 3.4.

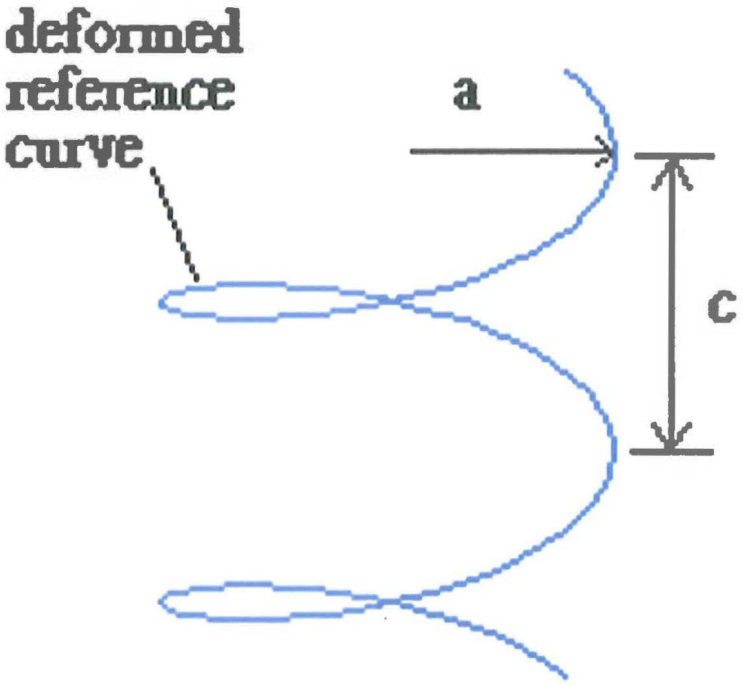

Figure 24: A helical wool fibre

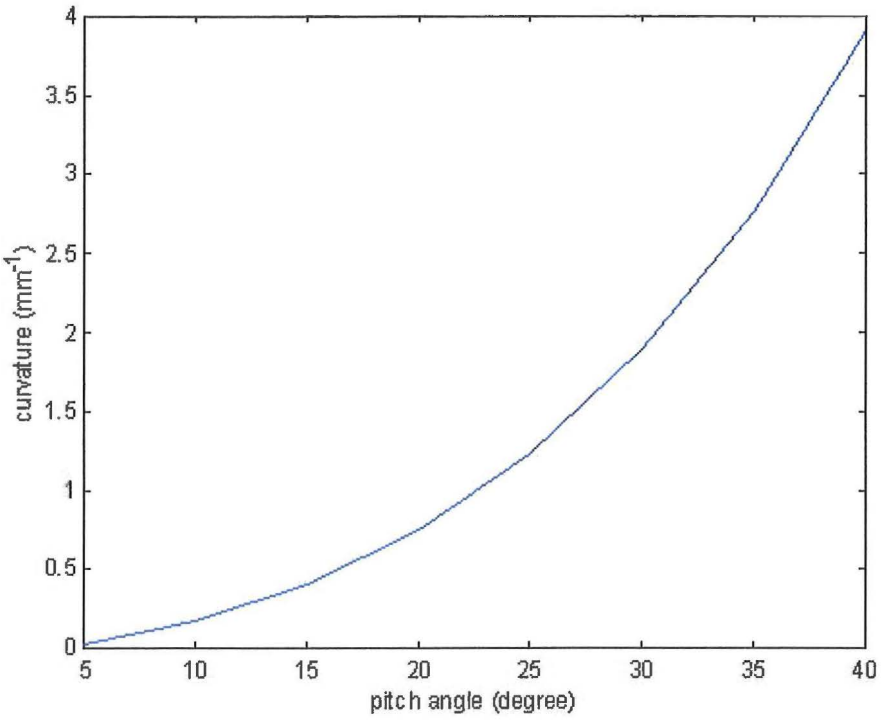

Figure 25: Fibre curvature versus pitch angle ϕ of the ortho-cortical IFs

3.5.1 Pitch angle of the helical ortho-cortical IFs

The outermost pitch angles of helical ortho-cortical IFs in a macrofibril can vary from 10° to 30°. Figures 25 and 26 show curvature κ and torsion τ as a function of the pitch angle ϕ from 5° to 40°. Both curvature and torsion increase with pitch angle (for larger pitch angles in the helices allow larger freedom of extension in axial direction). Hence, the increase in difference of the longitudinal length between helical IFs and rod like IFs produces an increase of bending.

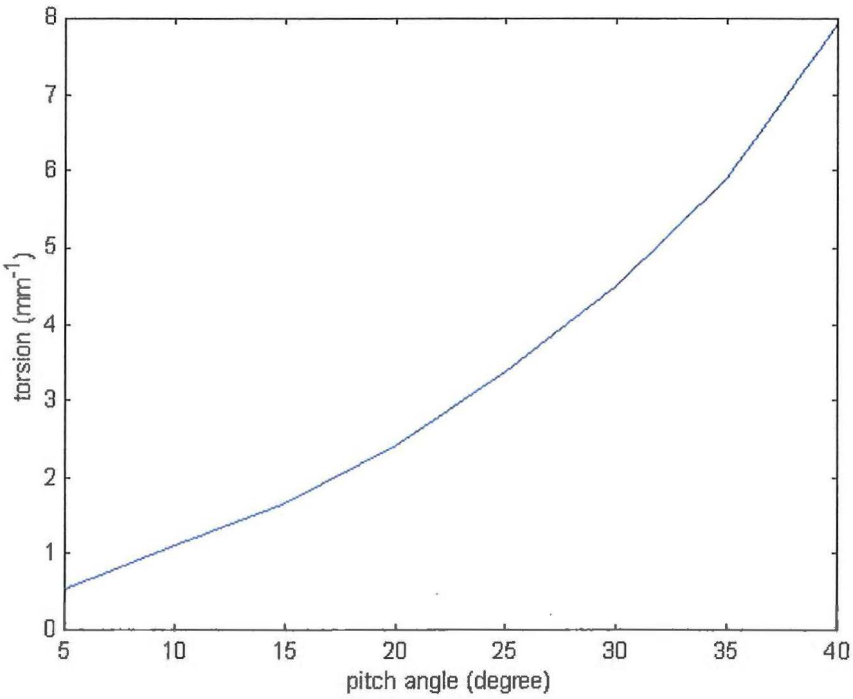

Figure 26: Fibre torsion as a function of pitch angle ϕ of the ortho-cortical IFs

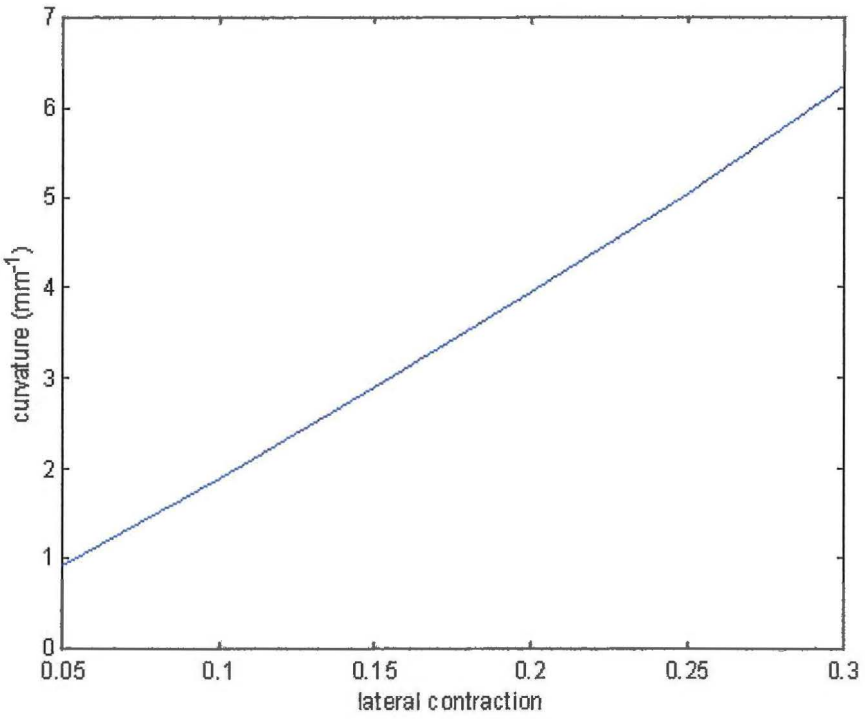

Figure 27: Fibre curvature versus lateral contraction γ

3.5.2 Lateral dilation of wool fibre

In this model, lateral dilation is the driving factor behind crimp formation. Figures 27 and 28 show the change in curvature and torsion as γ is varied from 0.1 to 0.3. Evidently, curvature and torsion both increase with γ because of squashing a helix in a lateral direction and this produces longer longitudinal length of the helix and higher strain energy under stress. However, torsion increases much less rapidly.

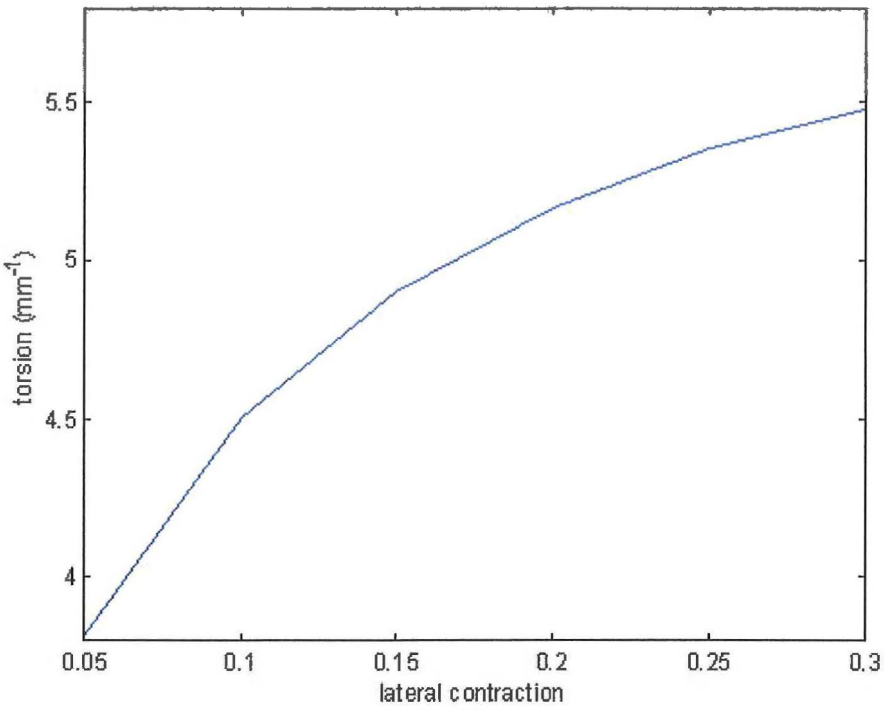

Figure 28: Fibre torsion as a function of lateral contraction γ

3.5.3 Para- and Meso-cortex

If a meso-cortex pattern is substituted for a para-cortex pattern with the same geometry but higher density in IFs, the simulation results are,

$$\begin{aligned} \kappa &= 1.89 \text{ mm}^{-1} , \\ \tau &= 7.22 \text{ mm}^{-1} , \\ \rho &= 1.01 , \\ \theta &= \frac{3\pi}{2} \text{ rad} , \\ a &= 0.03 \text{ mm} , \\ c &= 0.13 \text{ mm} , \\ \kappa : \tau &= 0.26 . \end{aligned}$$

Compared with Section 3.4, it is clear that the substitution reduces a, c and the $\kappa : \tau$ ratio. Since a large amount of strain energy is needed to extend the arc length of the IFs, a model with more rod-like IFs with the same MOP pattern should form a straighter shape to attain the minimum energy state.

3.5.4 Various bilateral pattern

Consider a bilateral cross-section as shown in Figure 18. This cross-section consists of equal densities of helical ortho-cortical IFs and rod-like para-cortical IFs, but the proportion of the two may be varied. By varying this proportion, the pattern that gives an optimal amount of crimp may be found.

The results are shown in Figures 29, 30 and 31. The latter graph demonstrates that when the ortho-to-para ratio is between 60 : 40 and 80 : 20, the curvature to torsion ratio is close 1 : 1. This is the 'most crimpy' using the definition given previously, although the ratio which results in the maximum amount of curvature is not included in this range. Therefore, measuring the curvature alone may not give an adequate estimate of a fibre's crimp.

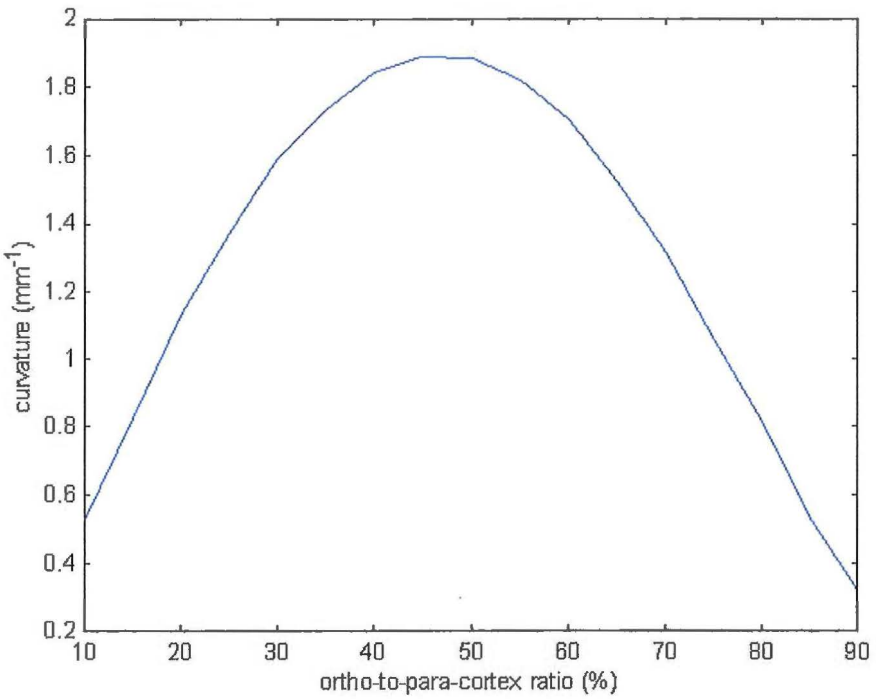

Figure 29: Curvature versus ortho-to-para-cortex ratio (with straight line segments)

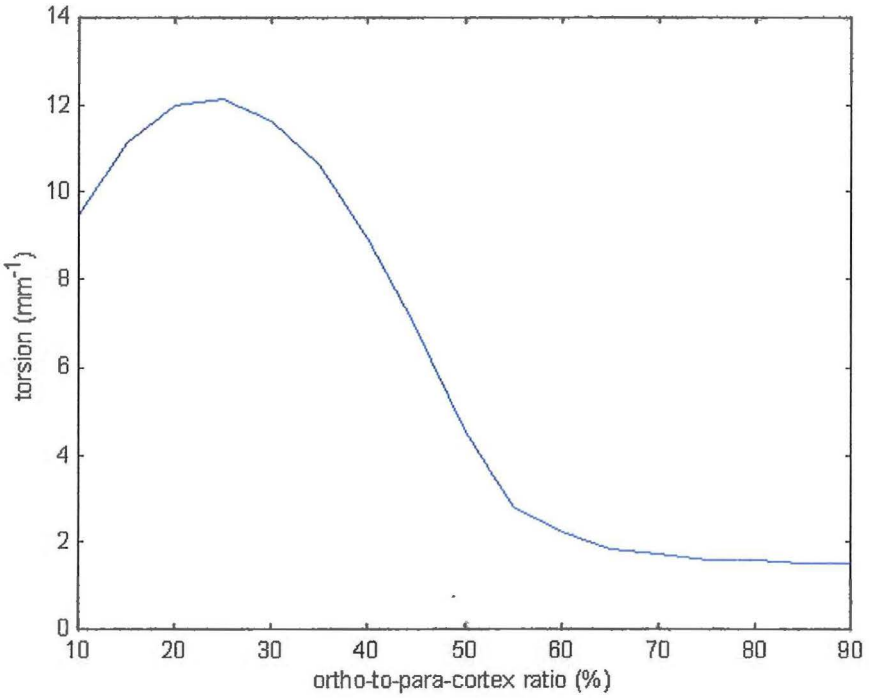

Figure 30: Fibre torsion versus ortho-to-para-cortex ratio (with straight line segments)

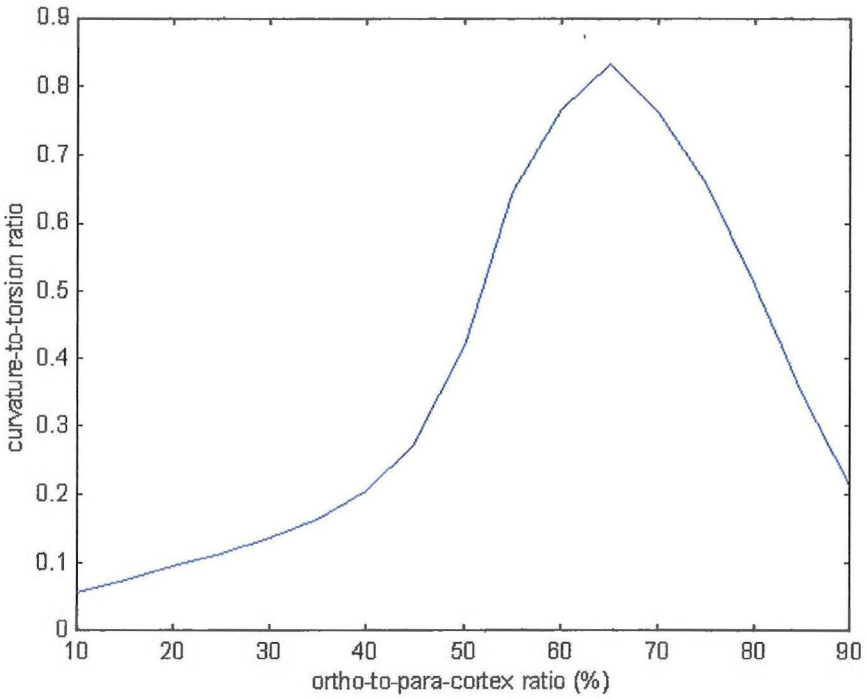

Figure 31: Curvature-to-torsion ratio as a function of ortho-to-para-cortex ratio (with straight line segments)

3.6 Energy surface

In the simple case with only three IF components — similar to the examples given in Section 2.4 but with helices instead of long rods — the simulated results are

$$\begin{aligned} \kappa &= 2.45 \text{ mm}^{-1} , \\ \tau &= 1.91 \text{ mm}^{-1} , \\ \rho &= 1.01 , \\ \theta &= \frac{3\pi}{2} \text{ rad} , \\ a &= 0.25 \text{ mm} , \\ c &= 0.19 \text{ mm} . \end{aligned}$$

The energy-contour plot with fixed parameters $\rho = 1.01$ and $\theta = \frac{3\pi}{2}$ is shown in Figure 32. Fixing these parameters does not change the qualitative shape of the fibre significantly. There is a local minimum for positive torsion. This is different from the long-and-short-rods model which has a symmetrical contour plot. The difference is presumably caused by the chirality of helices. The ortho-cortical IFs are right-handed helices while the wool fibre attains an energy minimum by deforming into a left-handed helix.

3.7 Addition of the cuticle

Cuticle cells are thought to form a stiff scale-like structure on the surface of the hair fibres.[1] This layer of cells can be modelled as a thin cylindrical shell of thickness r_c. In this section, we can consider a simple model that includes the cuticle. In this model, it is assumed that there is no shearing within the shell and between the shell and the fibre body. It is further assumed that the shell shrinks in accord with the cortex so that its final inner radius

[1] After this thesis was completed, new experimental work has been performed which appears to cast doubt on this belief [6].

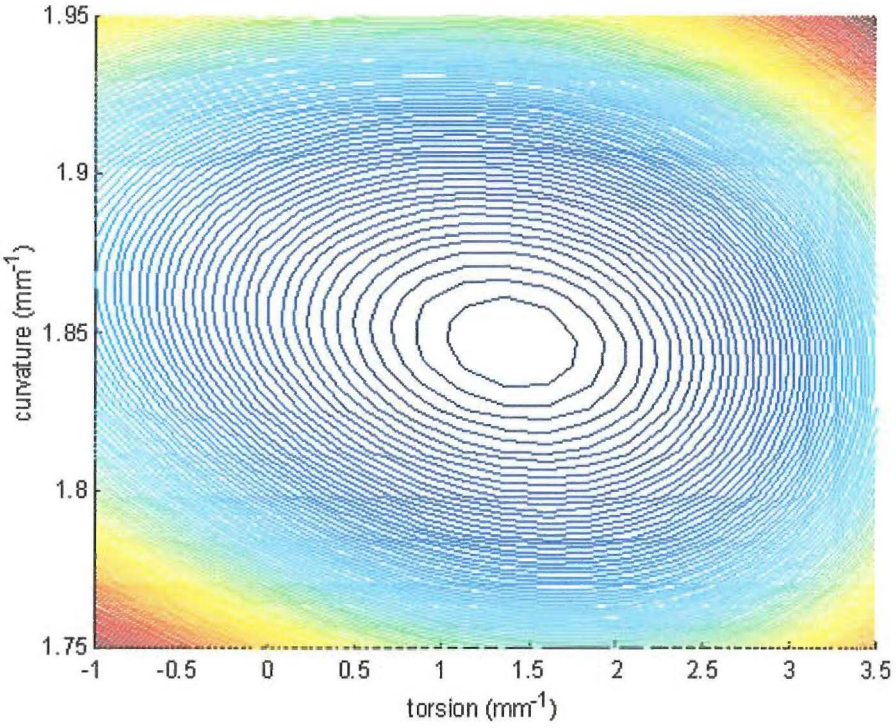

Figure 32: Energy contours of a simple helix and rod model

after desorption is $\tilde{R}_w = (1-\gamma)R_w$. In addition, the shell is assumed to be homogenous and isotropic. The cuticle is initially a cylinder and after desorption its axis becomes helical. The coordinate along its axis is denoted by z and the cylindrical angle by ψ.

The cylindrical axis describes a helix of curvature κ and torsion τ, the dimensionless components of strain $\epsilon = (\epsilon_{zz}, \epsilon_{\psi\psi}, \epsilon_{z\psi})$, are given by

$$\begin{aligned} \epsilon_{zz} &= (\rho - 1) - \tilde{R}_w \kappa \cos\psi \ , \\ \epsilon_{z\psi} &= \frac{1}{2}\tilde{R}_w \tau \ , \\ \epsilon_{\psi\psi} &= 0 \ . \end{aligned}$$

These formulae may be motivated as follows. First consider a cuticle which is simply elongated but has $\kappa = 0 = \tau$. The strain is $\epsilon_{zz} = \rho - 1$. Similarly, if there is no elongation ($\rho = 1$) and no curvature ($\kappa = 0$), but torsion is non-zero then the cuticle is simply twisted about its axis and the only non-zero component of strain is the shear term $\epsilon_{z\psi} = \frac{1}{2}\tilde{R}_w\tau$. Notice this has been made dimensionless by the inclusion of $\tilde{R}_w$, which is different to the conventions used by most other authors. Finally, if $\tau = 0 = \rho - 1$, but $\kappa \neq 0$, then the cuticle is curved but not stretched or twisted and the strain is only longitudinal: $\epsilon_{zz} = -\tilde{R}_w \kappa \cos\psi$. The $\cos\psi$ term means that portions of the cylinder on the inside of the curve are in compression, while the exterior portions are in tension.

By assumption, the cuticle is homogeneous and isotropic so the compliance matrix is (see Appendix C for further details regarding stress and strain in two dimensional shells)

$$C = r_c \begin{pmatrix} \frac{E_c}{1-\nu^2} & \frac{\nu E_c}{1-\nu^2} & 0 \\ \frac{\nu E_c}{1-\nu^2} & \frac{E_c}{1-\nu^2} & 0 \\ 0 & 0 & \frac{E_c}{1+\nu} \end{pmatrix} , \tag{3.8}$$

and the strain energy of a deformed cuticle shell is therefore

$$\begin{aligned} e_c &= \int_0^L \int_0^{2\pi} \tfrac{1}{2}\epsilon^t C \epsilon \, \tilde{R}_w \mathrm{d}\psi \mathrm{d}z \\ &= \frac{r_c}{2} \int_0^L \int_0^{2\pi} \left[\Big((\rho - 1) - \tilde{R}_w \kappa \cos(\psi) \Big)^2 \frac{E_c}{1-\nu^2} + \left(\frac{1}{2} \tilde{R}_w \tau \right)^2 \frac{E_c}{1+\nu} \right] \tilde{R}_w \mathrm{d}\psi \mathrm{d}z \\ &= \frac{r_c \tilde{R}_w \pi L E_c}{2(1-\nu^2)} \left[\tilde{R}_w^2 \kappa^2 + 2(\rho - 1)^2 + \tfrac{1}{2}(1-\nu) \tilde{R}_w^2 \tau^2 \right]. \end{aligned}$$

The total strain energy of wool fibre is $e_w + e_c$. Using the same configuration as Section 3.4 and using $E_c = 0.1$ to 5 (relative to the cortex), $\nu = 0.5$ and $r_c = 0.1$ μm, the new results are given in Figure 33, 34 and 35. Note the 'x' marks on the figures show where the Young's modulus of the cuticle is zero, which can be considered as no cuticle. These are the same results given in Section 3.4.

The results show that curvature, torsion and curvature-to-torsion ratio decrease with the value of the Young's modulus of the cuticle. A low Young's modulus value of the cuticle helps the fibre to form a more helical shape by increasing the curvature-to-torsion ratio. However, since the value of cuticle's moduli are presently unknown, these results may be altered dramatically by future experimental work. This formulation allows different values of the moduli to be used.

3.8 Approximate analytical solution

The equations of the strain energy of helical IFs consist of an elliptic integral which cannot be solved and analysed easily. By evaluating a second order Taylor's expansion, the strain energy equation of the wool fibre is reduced into a second order polynomial in $(\rho - 1)$, κ and τ. The reason such an expansion is reasonable is that the numerical simulations always yield

$$|\rho - 1| \ll 1 \, .$$

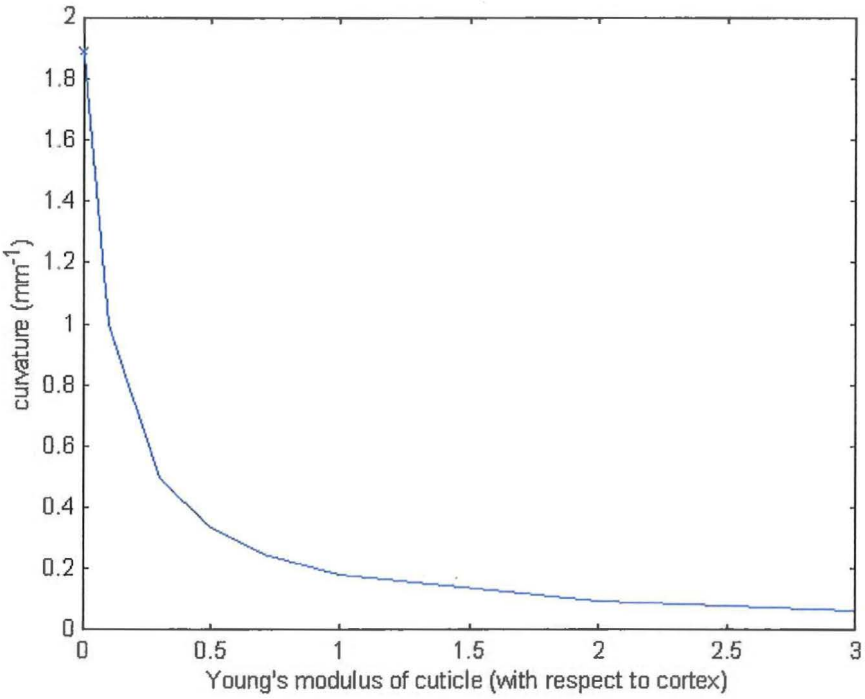

Figure 33: Fibre curvature versus Young's modulus of cuticle

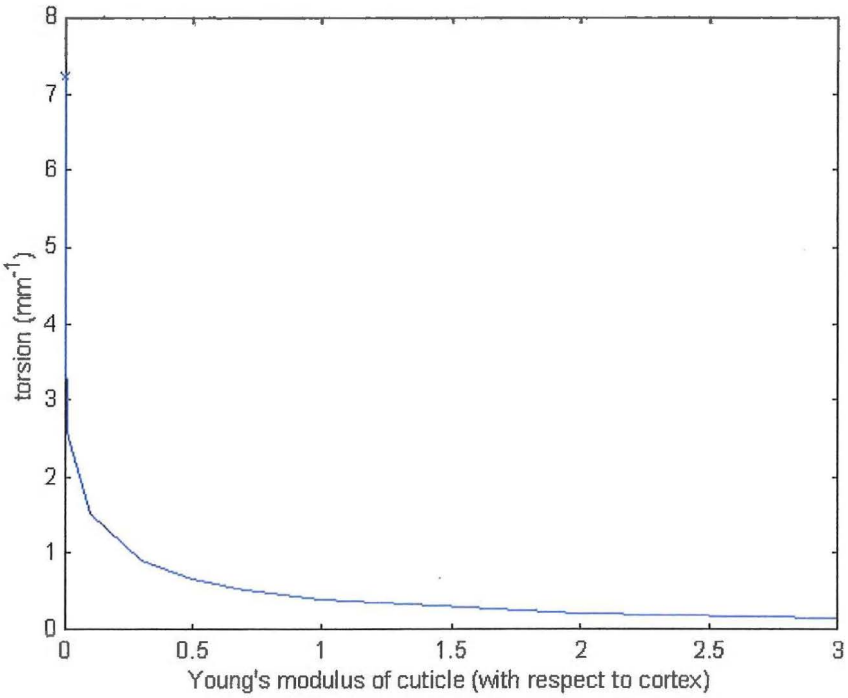

Figure 34: Fibre torsion versus Young's modulus of cuticle

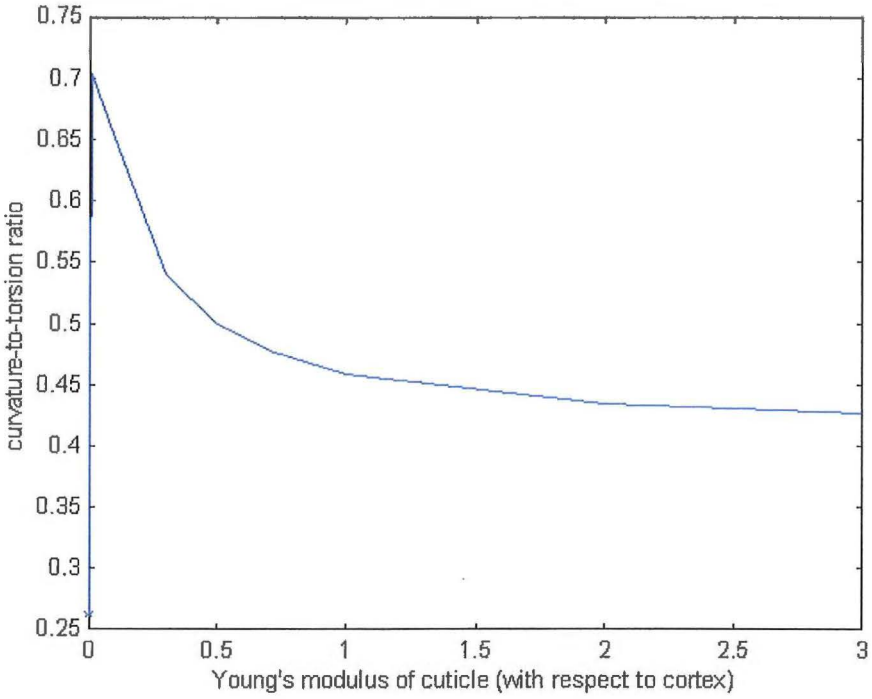

Figure 35: Fibre curvature-to-torsion ratio versus Young's modulus of cuticle

Moreover, in the expressions for IF energy, the parameters κ and τ are always multiplied by either $\tilde{d}$ or $\tilde{r}$. Experimental evidence (see Section 6) suggests that $\kappa \sim 1$ mm$^{-1} \sim \tau$ and also $\tilde{r} \sim 0.3$ μm and $\tilde{d} \sim 20$ μm. Therefore,

$$|\kappa\tilde{r}| \ll 1\,, \quad |\kappa\tilde{d}| \ll 1\,, \quad |\tau\tilde{r}| \ll 1 \quad \text{and} \quad |\tau\tilde{d}| \ll 1\,.$$

In special cases symmetry dictates the value of θ obtained, and the first derivative of the approximate energy with respect to the three remaining variables will form a system of linear equations which may be solved analytically.

The numerical simulations often result in two local minima, one with positive torsion and the other with negative torsion. A second-order expansion will yield at most one minimum. However, the motivation behind constructing the expansion is that the analytically-found minimum may be close enough to the true global minimum that an analytic exploration of parameter sensitivity along the lines of the graphs found in Section 3.5 may be possible. Unfortunately, this does not occur.

The strain energy equation of a helical IF may be rearranged to read

$$\frac{e_o}{L_o A_o} = \frac{E_o}{2}\left(1 - \frac{\tilde{L}_o}{L_o}\right)^2 .$$

As well as expanding in small $\rho - 1$, κ and τ, the large L limit is taken, which simplifies this ortho-cortical energy density, since terms like $\frac{1}{L}\int_0^{\rho L} \cos(\omega s) ds$ are $O(1/L)$ and may be neglected in favour of $O(1)$ terms such as $\frac{1}{L}\int_0^{\rho L} \cos^2(\omega s) ds$. The general form of the expansion is

$$\begin{aligned}
\frac{e_o}{L_o E_o A_o} \;=\; & k_0' + k_1'(\rho-1) + k_2'\kappa_r + k_3'\kappa_d + k_4'\tau_r + k_5'\tau_d \\
& + k_6'(\rho-1)^2 + k_7'\kappa_r^2 + k_8'\kappa_d^2 + k_9'\tau_r^2 + k_{10}'\tau_d^2 \\
& + k_{11}'(\rho-1)\kappa_r + k_{12}'(\rho-1)\kappa_d + k_{13}'(\rho-1)\tau_r + k_{14}'(\rho-1)\tau_d \\
& + k_{15}'\kappa_r\kappa_d + k_{16}'\kappa_r\tau_r + k_{17}'\kappa_r\tau_d + k_{18}'\kappa_d\tau_r + k_{19}'\kappa_d\tau_d + k_{20}'\tau_r\tau_d\,.
\end{aligned}$$

where (k')'s are non-dimensional constants and $\kappa_r = \kappa\tilde{r}$, $\kappa_d = \kappa\tilde{d}$, $\tau_r = \tau\tilde{r}$, $\tau_d = \tau\tilde{d}$. It can be rewritten in terms of $(\rho - 1)$, κ and τ

$$\begin{aligned}\frac{e_o}{L_o E_o A_o} &= k_0 + k_1(\rho-1) + k_2\kappa + k_3\tau + k_{11}(\rho-1)^2 + k_{22}\kappa^2 + k_{33}\tau^2 \\ &\quad + k_{12}(\rho-1)\kappa + k_{13}(\rho-1)\tau + k_{23}\kappa\tau \ .\end{aligned}$$

The symbolic mathematics package Mathematica [13] was used to obtain

$$\begin{aligned}
k_0 &= \frac{1}{2}(\alpha-1)^2 \ , \\
k_1 &= \frac{\alpha-1}{\alpha}\cos^2(\phi) \ , \\
k_2 &= -\frac{\alpha-1}{\alpha}d_o\cos(\theta_o-\theta)\cos^2(\phi) \ , \\
k_3 &= \frac{\alpha-1}{\alpha}r\cot(\phi)(\alpha^2-\cos^2(\phi)) \ , \\
k_{11} &= \frac{1}{2\alpha^3}\cos^2(\phi)(\alpha^2(\alpha-1)+\cos^2(\phi)) \ , \\
k_{22} &= \frac{\cos^2(\phi)}{16\alpha^3}[4d_o^2(1+2\alpha^2(\alpha-1)+\cos(2\phi))\cos^2(\theta_o-\theta) \\
&\quad +(\alpha-1)r^2(1-2\alpha^2+\cos(2\phi))^2\csc^2(\phi)] \ , \\
k_{33} &= \frac{\cot^2(\phi)}{4\alpha^3}[d_o^2(\alpha-1)\cos^2(\phi)(\alpha^2+\cos^2(\phi) \\
&\quad +2r^2(\alpha^5-\alpha^2(\alpha+1)\cos^2(\phi)+\cos^4(\phi)] \ , \\
k_{12} &= -\frac{1}{\alpha^3}[d_o\cos^2(\phi)(2(\alpha-1)\alpha^2+\cos^2(\phi)\cos(\theta_o-\theta)] \ , \\
k_{13} &= -\frac{1}{4\alpha^3}[r(1-2\alpha^2+\cos(2\phi))(1+2\alpha^2(\alpha-1)+\cos(2\phi)\cot(\phi)] \ , \\
k_{23} &= -\frac{1}{4\alpha^3}[(\alpha-3)d_o r\cos^2(\phi)(1-2\alpha^2+\cos(2\phi)\cos(\theta_o-\theta)\cot(\phi)] \ ,
\end{aligned}$$

with

$$\alpha = \sqrt{1+(\gamma-1)^2\tan^2\phi}\cos\phi \ .$$

The same steps applied to the para or meso-cortical IF energy yields

$$\frac{e_p}{LA_pE_p} = \tfrac{1}{2}(\rho - 1 + d_p\kappa\cos(\theta_p - \theta))^2 \ .$$

Setting

$$K_i = \sum_{\text{all IFs}} k_i \text{ and } K_{ij} = \sum_{\text{all IFs}} k_{ij} \ ,$$

these are the summation of the coefficients of the strain energy equations of each IFs and the minimum of the total energy (Equation (3.7)) is at

$$\begin{pmatrix} 2K_{11} & K_{12} & K_{13} \\ K_{12} & 2K_{22} & K_{23} \\ K_{13} & K_{23} & 2K_{33} \end{pmatrix} \begin{pmatrix} \rho - 1 \\ \kappa \\ \tau \end{pmatrix} = - \begin{pmatrix} K_1 \\ K_2 \\ K_3 \end{pmatrix} .$$

These equations can be solved easily, with the same configuration as described in Section 3.4 where symmetry implies that $\theta = \frac{3\pi}{2}$, and the minimum is found at

$$\begin{aligned} \kappa &= 4.23 \times 10^{-6} \text{ mm}^{-1} \ , \\ \tau &= 8.06 \times 10^{-6} \text{ mm}^{-1} \ , \\ \rho &= 1.001 \ , \\ a &= 5.10 \times 10^{4} \text{ mm} \ , \\ c &= 9.72 \times 10^{4} \text{ mm} \ , \\ \kappa : \tau &= 0.52 \ . \end{aligned}$$

The results of the quadratic approximation are quite surprisingly different from the original full model. It gives a trivial answer with a minimum around origin on the curvature and torsion space. A higher-order approximation would probably better estimate the position of the minimum, while here only shows the direction of getting an approximation model.

4 Macrofibril model

4.1 Introduction

In the previous chapter, a basic model is studied as a simplified case without considering the macrofibril structure of the wool fibre, while the macrofibril model provides a more realistic and complicated model. Under the microscope, the transverse cross-section of the ortho-cortical macrofibrils show a whorl pattern of circular structures, which gives evidence that macrofibrils in ortho-cortex are assembled with bundles of concentric helical IFs. In the meso-cortex, the IFs are located hexagonally. The para-cortex is similar but it has a more disordered pattern and the density of IFs is less than that in meso-cortex.

Hence, the macrofibrils can be described as a collection of concentric helices in the ortho-cortex. In the para- and meso-cortex, rod-like IFs are used instead and the number of IFs in the para-cortex will about one-third to a half of that in the meso-cortex.

4.2 Mathematical model

With the same assumptions which are used in the basic model, each single ortho-cortical macrofibril can be considered as a cylinder with a number of concentric helical IFs in the original state. Refer to Figure 36, the cross-section of the macrofibril will consist of layers of annuli of different radii. Each annulus has a different amount of helices of the same radius.

Let n_{a} be the number of annuli in a macrofibril and n_i be the number of IFs in the i^{th} annulus with $i = 1..n_{\mathrm{a}}$. If the transverse cross-sectional area of the ortho-cortical IFs is A_{IF}, in the ortho-cortical macrofibrils, the cross-section area of the IFs are proportional to the square of their radii. Then an IF with radius r and pitch angle $\phi(r)$ will give a cross-sectional area $\frac{A_{\mathrm{IF}}}{\cos(\phi(r))}$. In the meso- and para-cortex, the cross-sectional area of the IFs is A_{IF}, for

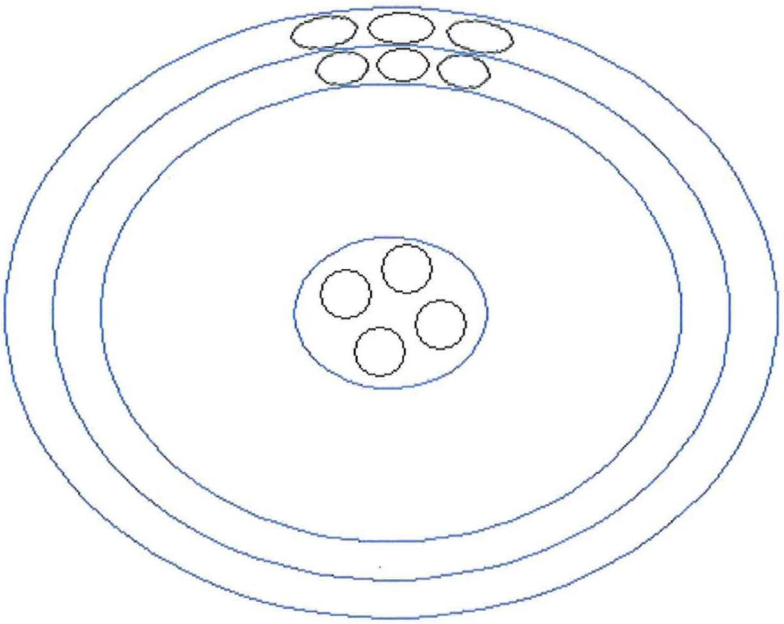

Figure 36: Cross-section of a macrofibril model (refer to Figure 10)

the rod-like IFs inside are assumed be always parallel to the axial direction of the wool fibre. Therefore, the ortho-cortical IFs near the centre of the macrofibril have small pitch angles and these IFs will trend to rods.
Then the strain energy of each IF during shrinkage can be calculated by a similar equation from the previous chapter. Suppose there are N_{o} macrofibrils in the ortho-cortex. Denoting the j_{th} ortho-cortical IF in the i_{th} annulus of the k_{th} marcofibril, with $i = 1..n_a$, $j = 1..n_i$ and $k = 1..N_o$. Given the generating curve (axis of the macrofibril) $\mathbf{g}_{\mathrm{o}}^k$ and the position of the IF (in global coordinates) $\mathbf{h}_{\mathrm{o}}^{ijk}$.

$$\mathbf{g}_{\mathrm{o}}^k = \mathbf{l}(s) + \tilde{d}_{\mathrm{o}}^k \cos(\theta_{\mathrm{o}}^k - \theta)\mathbf{N}(s) + \tilde{d}_{\mathrm{o}}^k \sin(\theta_{\mathrm{o}}^k - \theta)\mathbf{B}(s),$$

and

$$\begin{aligned}
\mathbf{h}_{\mathrm{o}}^{(ijk)} &= \mathbf{g}_{\mathrm{o}}^k(s) + \tilde{r}_{IF}^i \cos(\omega s - \theta + \theta_{IF}^{ij})\mathbf{N}(s) + \tilde{r}_{IF}^i \sin(\omega s - \theta + \theta_{IF}^{ij})\mathbf{B}(s), \\
&= \mathbf{l}(s) + \left[\tilde{d}_{\mathrm{o}}^k \cos(\theta_{\mathrm{o}}^k - \theta) + \tilde{r}_{IF}^i \cos(\omega s - \theta + \theta_{IF}^{ij})\right] \mathbf{N}(s) \\
&\quad + \left[\tilde{d}_{\mathrm{o}}^k \sin(\theta_{\mathrm{o}}^k - \theta) + \tilde{r}_{IF}^i \sin(\omega s - \theta + \theta_{IF}^{ij})\right] \mathbf{B}(s),
\end{aligned}$$

where $\mathbf{l}(s)$ is the reference curve (axis) of the wool fibre. For the effect of lateral contraction γ of the wool fibre when drying, all the radial distances will be decreased by a factor $(1-\gamma)$. Therefore, after shrinkage, the distance between the reference curve to the generating curve of the k_{th} macrofibril becomes $\tilde{d}_o^k = (1-\gamma)d_o^k$ and the radius of a IF in the i_{th} annulus is $\tilde{r}_{\mathrm{IF}}^i = (1-\gamma)r_{IF}^i$. Ortho-cortical IFs in the same annulus also have a phase difference between each other. Let $\theta_{\mathrm{IF}}^{ij}$ be the phase angle of the j^{th} ortho-cortical IF in the i^{th} annulus. Although the pitch angles and the radii of the IFs in different annuli are varying, the pitch distance of the helical IFs is assumed to be the same and it is equal to the ratio $\frac{\tan(\phi(r_{\mathrm{IF}}^i))}{r_{\mathrm{IF}}^i}$. Therefore, the parameter $\omega = \frac{\tan(\phi(r_{\mathrm{IF}}^{n_a}))}{\rho r_{\mathrm{IF}}^{n_a}}$ is constant for all helical IFs and $\phi(r_{\mathrm{IF}}^{n_a})$ is the pitch angle and $r_{\mathrm{IF}}^{n_a}$ is the radius of the outermost ortho-cortical IFs.

Using the Frenét formulae again,

$$\begin{aligned}
\frac{\mathrm{d}\mathbf{h}_{\mathrm{o}}^{ijk}}{\mathrm{d}s}(s) &= \mathbf{T}(s) + \left(\tilde{d}_{\mathrm{o}}^{k}\cos(\theta_{\mathrm{o}}^{k}-\theta) + \tilde{r}_{\mathrm{IF}}^{i}\cos(\omega s-\theta+\theta_{\mathrm{IF}}^{ij})\right)(-\kappa\mathbf{T}(s)+\tau\mathrm{B}(s)) \\
&\quad -\tilde{r}_{\mathrm{IF}}^{i}\omega\sin(\omega s-\theta+\theta_{\mathrm{IF}}^{ij})\mathbf{N}(s) \\
&\quad + \left(\tilde{d}_{\mathrm{o}}^{k}\sin(\theta_{\mathrm{o}}^{k}-\theta) + \tilde{r}_{\mathrm{IF}}^{i}\sin(\omega s-\theta+\theta_{\mathrm{IF}}^{ij})\right)(-\tau\mathbf{N}(s)) \\
&\quad -\tilde{r}_{\mathrm{IF}}^{i}\omega\cos(\omega s-\theta+\theta_{\mathrm{IF}}^{ij})\mathbf{B}(s), \\
&= \left[1-\kappa(\tilde{d}_{\mathrm{o}}^{k}\cos(\theta_{\mathrm{o}}^{k}-\theta)+\tilde{r}_{\mathrm{IF}}^{i}\cos(\omega s-\theta+\theta_{\mathrm{IF}}^{ij}))\right]\mathbf{T}(s) \\
&\quad -\left[\tilde{r}_{\mathrm{IF}}^{i}\omega\sin(\omega s-\theta+\theta_{\mathrm{IF}}^{ij})+\tau(\tilde{d}_{\mathrm{o}}^{k}\sin(\theta_{\mathrm{o}}^{k}-\theta)+\tilde{r}_{\mathrm{IF}}^{i}\sin(\omega s-\theta+\theta_{\mathrm{IF}}^{ij}))\right]\mathbf{N}(s) \\
&\quad +\left[\tilde{r}_{\mathrm{IF}}^{i}\omega\cos(\omega s-\theta+\theta_{\mathrm{IF}}^{ij})+\tau(\tilde{d}_{\mathrm{o}}^{k}\cos(\theta_{\mathrm{o}}^{k}-\theta)+\tilde{r}_{\mathrm{IF}}^{i}\cos(\omega s-\theta+\theta_{\mathrm{IF}}^{ij}))\right]\mathbf{B}(s).
\end{aligned}$$

Then,

$$\begin{aligned}
\left|\frac{\mathrm{d}\mathbf{h}_{\mathrm{o}}^{ijk}}{\mathrm{d}s}\right|^{2} &= \left[1-\kappa(\tilde{d}_{\mathrm{o}}^{k}\cos(\theta_{\mathrm{o}}^{k}-\theta)+\tilde{r}_{\mathrm{IF}}^{i}\cos(\omega s-\theta+\theta_{\mathrm{IF}}^{ij}))\right]^{2} \\
&\quad +\left[\tilde{r}_{\mathrm{IF}}^{i}\omega\sin(\omega s-\theta+\theta_{\mathrm{IF}}^{ij})+\tau(\tilde{d}_{\mathrm{o}}^{k}\sin(\theta_{\mathrm{o}}^{k}-\theta)+\tilde{r}_{\mathrm{IF}}^{i}\sin(\omega s-\theta+\theta_{\mathrm{IF}}^{ij}))\right]^{2} \\
&\quad +\left[\tilde{r}_{\mathrm{IF}}^{i}\omega\cos(\omega s-\theta+\theta_{\mathrm{IF}}^{ij})+\tau(\tilde{d}_{\mathrm{o}}^{k}\cos(\theta_{\mathrm{o}}^{k}-\theta)+\tilde{r}_{\mathrm{IF}}^{i}\cos(\omega s-\theta+\theta_{\mathrm{IF}}^{ij}))\right]^{2}.
\end{aligned}$$

The arc length of a deformed $(i,j,k)^{\mathrm{th}}$ ortho-cortical IF is

$$\begin{aligned}
\tilde{L}_{\mathrm{o}}^{ijk} &= \int_{0}^{\rho L}\left|\frac{\mathrm{d}\mathbf{h}_{\mathrm{o}}^{ijk}}{\mathrm{d}s}\right|\mathrm{d}s, \\
&= \int_{0}^{\rho L}\Big(\left[1-\kappa(\tilde{d}_{\mathrm{o}}^{k}\cos(\theta_{\mathrm{o}}^{k}-\theta)+\tilde{r}_{\mathrm{IF}}^{i}\cos(\omega s-\theta+\theta_{\mathrm{IF}}^{ij}))\right]^{2} \\
&\quad +\left[\tilde{r}_{\mathrm{IF}}^{i}\omega\sin(\omega s-\theta+\theta_{\mathrm{IF}}^{ij})+\tau(\tilde{d}_{\mathrm{o}}^{k}\sin(\theta_{\mathrm{o}}^{k}-\theta)+\tilde{r}_{\mathrm{IF}}^{i}\sin(\omega s-\theta+\theta_{\mathrm{IF}}^{ij}))\right]^{2} \\
&\quad +\left[\tilde{r}_{\mathrm{IF}}^{i}\omega\cos(\omega s-\theta+\theta_{\mathrm{IF}}^{ij})+\tau(\tilde{d}_{\mathrm{o}}^{k}\cos(\theta_{\mathrm{o}}^{k}-\theta)+\tilde{r}_{\mathrm{IF}}^{i}\cos(\omega s-\theta+\theta_{\mathrm{IF}}^{ij}))\right]^{2}\Big)^{\frac{1}{2}}\mathrm{d}s.
\end{aligned}$$

Given the original arc length of the IF is $L_{\mathrm{o}}^{ijk} = L/\cos(\phi(r_{\mathrm{IF}}^{i}))$, the strain

energy of the ortho-cortical IF is then

$$e_{\mathrm{o}}^{ijk} = \frac{1}{2}\frac{E_{\mathrm{o}}A_{\mathrm{o}}}{L_{\mathrm{o}}^{ijk}}\left(L_{\mathrm{o}}^{ijk} - \tilde{L}_{\mathrm{o}}^{ijk}\right)^2,$$

where E_{o} is the Young's modulus and A_{o} is the transverse cross-sectional area of the ortho-cortical IF.

Likewise, if there are N_{p} macrofibrils in the wool fibre, the position (in global coordinates) of the j_{th} IF in the i_{th} annulus of the k_{th} para-cortical macrofibril is

$$\begin{aligned}\mathbf{h}_{\mathrm{p}}^{ijk} &= \mathrm{l}(s) + \left[\tilde{d}_{\mathrm{p}}^{k}\cos(\theta_{\mathrm{p}}^{k} - \theta) + \tilde{r}_{IF}^{i}\cos(\theta_{IF}^{ij} - \theta)\right]\mathbf{N}(s) \\ &\quad + \left[\tilde{d}_{\mathrm{p}}^{k}\sin(\theta_{\mathrm{p}}^{k} - \theta) + \tilde{r}_{IF}^{i}\sin(\theta_{IF}^{ij} - \theta)\right]\mathbf{B}(s),\end{aligned}$$

with the deformed radius $\tilde{d}_{\mathrm{p}}^{k} = (1-\gamma)d_{\mathrm{p}}^{k}$ and $i = 1..n_a$, $j = 1..n_i$ and $k = 1..N_{\mathrm{p}}$. So

$$\begin{aligned}\frac{\mathrm{d}\mathbf{h}_{\mathrm{p}}^{ijk}}{\mathrm{d}s}(s) &= \mathbf{T}(s) + \left(\tilde{d}_{\mathrm{p}}^{k}\cos(\theta_{\mathrm{p}}^{k} - \theta) + \tilde{r}_{\mathrm{IF}}^{i}\cos(\theta_{\mathrm{IF}}^{ij} - \theta)\right)(-\kappa\mathbf{T}(s) + \tau\mathrm{B}(s)) \\ &\quad + \left(\tilde{d}_{\mathrm{p}}^{k}\sin(\theta_{\mathrm{p}}^{k} - \theta) + \tilde{r}_{\mathrm{IF}}^{i}\sin(\theta_{\mathrm{IF}}^{ij} - \theta)\right)(-\tau\mathbf{N}(s)), \\ &= \left[1 - \kappa(\tilde{d}_{\mathrm{p}}^{k}\cos(\theta_{\mathrm{p}}^{k} - \theta) + \tilde{r}_{\mathrm{IF}}^{i}\cos(\theta_{\mathrm{IF}}^{ij} - \theta))\right]\mathbf{T}(s) \\ &\quad - \left[\tau(\tilde{d}_{\mathrm{p}}^{k}\sin(\theta_{\mathrm{p}}^{k} - \theta) + \tilde{r}_{\mathrm{IF}}^{i}\sin(\theta_{\mathrm{IF}}^{ij} - \theta))\right]\mathbf{N}(s) \\ &\quad + \left[\tau(\tilde{d}_{\mathrm{p}}^{k}\cos(\theta_{\mathrm{p}}^{k} - \theta) + \tilde{r}_{\mathrm{IF}}^{i}\cos(\theta_{\mathrm{IF}}^{ij} - \theta))\right]\mathbf{B}(s),\end{aligned}$$

and

$$\begin{aligned}\left|\frac{\mathrm{d}\mathbf{h}_{\mathrm{p}}^{ijk}}{\mathrm{d}s}\right|^2 &= \left[1 - \kappa(\tilde{d}_{\mathrm{p}}^{k}\cos(\theta_{\mathrm{p}}^{k} - \theta) + \tilde{r}_{\mathrm{IF}}^{i}\cos(\theta_{\mathrm{IF}}^{ij} - \theta))\right]^2 \\ &\quad + \tau^2\left[(\tilde{d}_{\mathrm{p}}^{k})^2 + (\tilde{r}_{\mathrm{IF}}^{i})^2 + 2\tilde{d}_{\mathrm{p}}^{k}\tilde{r}_{\mathrm{IF}}^{i}\cos(\theta_{\mathrm{p}}^{k} - \theta_{\mathrm{IF}}^{ij})\right].\end{aligned}$$

The deformed arc length of the para-cortical IF is

$$\begin{aligned}\tilde{L}_{\mathrm{p}}^{ijk} &= \int_0^{\rho L} \left|\frac{\mathrm{d}\mathbf{h}_{\mathrm{p}}^{ijk}}{\mathrm{d}s}\right| \mathrm{d}s, \\ &= \int_0^{\rho L} \Big(\Big[1 - \kappa(\tilde{d}_{\mathrm{p}}^{k} \cos(\theta_{\mathrm{p}}^{k} - \theta) + \tilde{r}_{\mathrm{IF}}^{i} \cos(\theta_{\mathrm{IF}}^{ij} - \theta))\Big]^2 \\ &\quad + \tau^2 \left[(\tilde{d}_{\mathrm{p}}^{k})^2 + (\tilde{r}_{\mathrm{IF}}^{i})^2 + 2\tilde{d}_{\mathrm{p}}^{k}\tilde{r}_{\mathrm{IF}}^{i} \cos(\theta_{\mathrm{p}}^{k} - \theta_{\mathrm{IF}}^{ij})\right]\Big)^{\frac{1}{2}} \mathrm{d}s.\end{aligned}$$

The strain energy of the para-cortical IF is

$$e_{\mathrm{p}}^{ijk} = \frac{1}{2} \frac{E_{\mathrm{p}} A_{\mathrm{p}}}{L_{\mathrm{p}}^{ijk}} \left(L_{\mathrm{p}}^{ijk} - \tilde{L}_{\mathrm{p}}^{ijk}\right)^2,$$

where E_{p} is the Young's modulus and A_{p} is the transverse cross-sectional area of the ortho-cortical IF. Where the original state of a para-cortical is a straight rod parallel to the reference curve, the arc length of a wet para-cortical IF L_{p}^{ijk} will be equal to the original arc length of the reference curve L. The strain energy equation of a single meso-cortical IF can be worked out in the same way. The deformed arc length of the j^{th} meso-cortical IF in the i^{th} annulus of the k^{th} macrofibril is

$$\begin{aligned}\tilde{L}_{\mathrm{m}}^{ijk} &= \int_0^{\rho L} \Big(\Big[1 - \kappa(\tilde{d}_{\mathrm{m}}^{k} \cos(\theta_{\mathrm{m}}^{k} - \theta) + \tilde{r}_{\mathrm{IF}}^{i} \cos(\theta_{\mathrm{IF}}^{ij} - \theta))\Big]^2 \\ &\quad + \tau^2 \left[(\tilde{d}_{\mathrm{m}}^{k})^2 + (\tilde{r}_{\mathrm{IF}}^{i})^2 + 2\tilde{d}_{\mathrm{m}}^{k}\tilde{r}_{\mathrm{IF}}^{i} \cos(\theta_{\mathrm{m}}^{k} - \theta_{\mathrm{IF}}^{ij})\right]\Big)^{\frac{1}{2}} \mathrm{d}s,\end{aligned}$$

and the strain energy is

$$e_{\mathrm{m}}^{ijk} = \frac{1}{2} \frac{E_{\mathrm{m}} A_{\mathrm{m}}}{L_{\mathrm{m}}^{ijk}} \left(L_{\mathrm{m}}^{ijk} - \tilde{L}_{\mathrm{m}}^{ijk}\right)^2,$$

with Young's modulus E_{m} and transverse cross-sectional area A_{m}. Lastly,

the total strain energy of the wool fibre is

$$e_{\mathrm{w}}(\kappa,\tau,\rho,\theta)=\sum_{k=1}^{N_{\mathrm{o}}}\sum_{i=1}^{n_{\mathrm{a}}}\sum_{j=1}^{n_i}e_{\mathrm{o}}^{ijk}+\sum_{k=1}^{N_{\mathrm{p}}}\sum_{i=1}^{n_{\mathrm{a}}}\sum_{j=1}^{n_i^\star}e_{\mathrm{p}}^{ijk}+\sum_{k=1}^{N_{\mathrm{m}}}\sum_{i=1}^{n_{\mathrm{a}}}\sum_{j=1}^{n_i}e_{\mathrm{m}}^{ijk}.$$

The numbers of IFs in the macrofibrils in ortho-cortex and meso-cortex are both equal to $\sum_{i=1}^{n_{\mathrm{a}}} n_i$, while the number of IFs in para-cortical macrofibrils is equal to $\sum_{i=1}^{n_{\mathrm{a}}} n_i^\star$ and it is around half of the others to simulate the observed lower density of the IFs in the para-cortex. The resulting geometry is once again to be found by differentiating e_{w} with respect to the four variables κ, τ, ρ and θ.

4.3 Results of a fibre with macrofibril model

Here we use the same 50:50 ortho-para pattern from section 3.3. However, instead of having 3928 helical ortho-cortical IFs and 1965 para-cortical IFs, this model contains around the same density (also the amount in this case) of macrofibrils while the density of the IFs inside macrofibrils will be less in the para-cortex than in the ortho-cortex. Therefore, there are 3928 macrofibrils in both ortho- and para-cortex, 148 IFs in each ortho-cortical macrofibril and 70 IFs in each para-cortical macrofibril. The simulation results are,

$$\kappa = 1.88\mathrm{mm}^{-1},$$

$$\tau = 26.58\mathrm{mm}^{-1},$$

$$\rho \approx 1.00,$$

$$\theta = 4.71,$$

$$a = 0.75\mu\mathrm{m},$$

$$c = 37.61\mu\mathrm{m},$$

$$\kappa : \tau = 0.02.$$

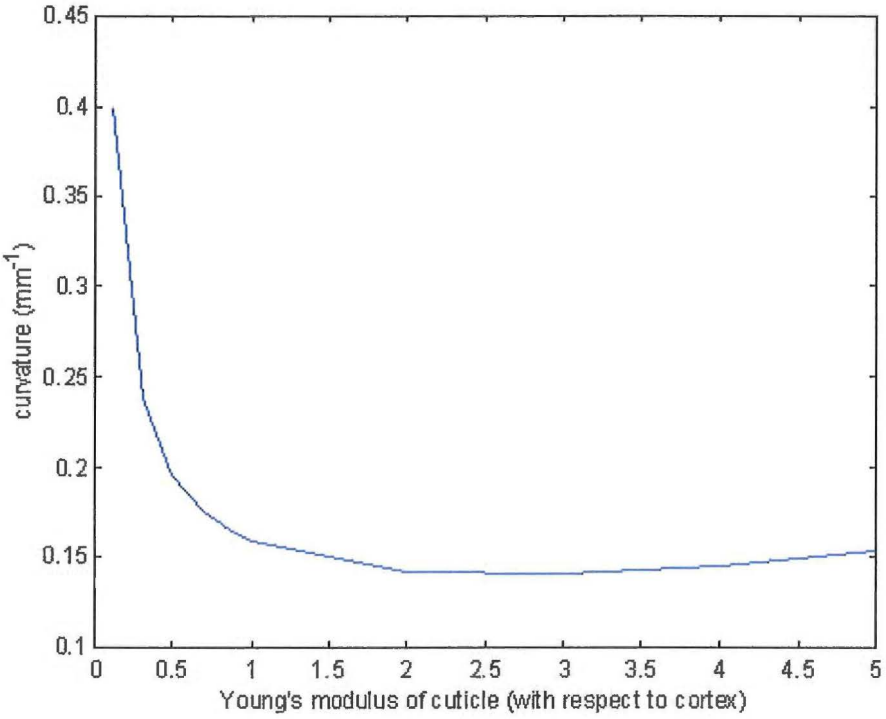

Figure 37: Fibre curvature versus Young's modulus of cuticle (with respect to cortex)

An extremely low curvature-to-torsion ratio is given for it requires high energy to bend and stretch the IFs near the centre of the ortho-cortical macrofibrils. This also cause the whole fibre is difficult to stretch longitudinally, and hence, ρ is nearly equal to 1. From the assumptions, no shearing and delocation is not permitted between the IFs, the amount of curvature may be highly suppressed. The results can be improved by the addition of a cuticle shell(Refer to section 3.7). By changing the value of the Young's modulus of the cuticle (with respect to cortex), the results are show in Figure 37, 38 and 39.

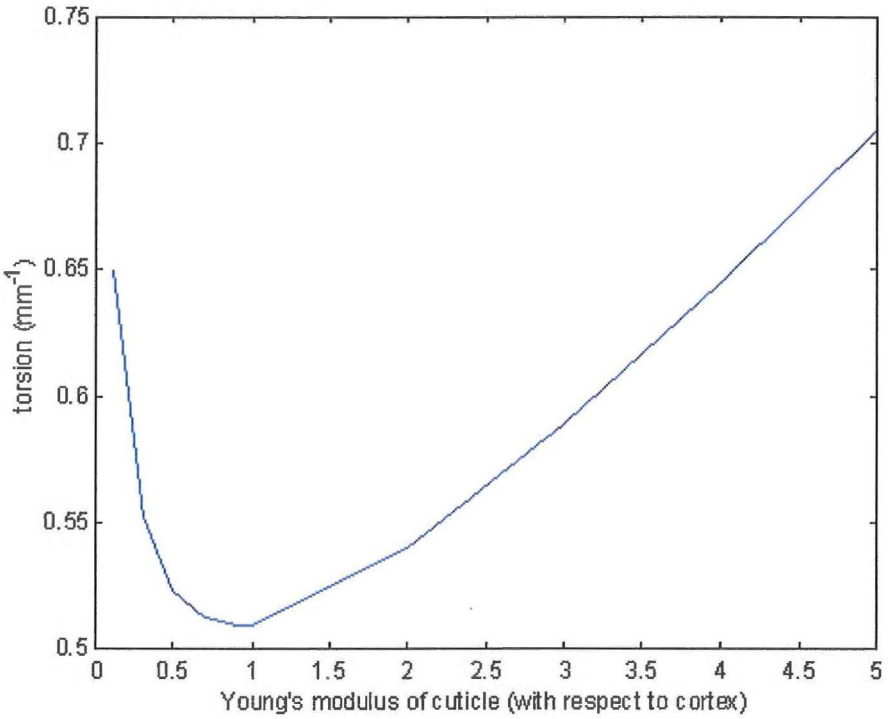

Figure 38: Fibre torsion versus Young's modulus of cuticle (with respect to cortex)

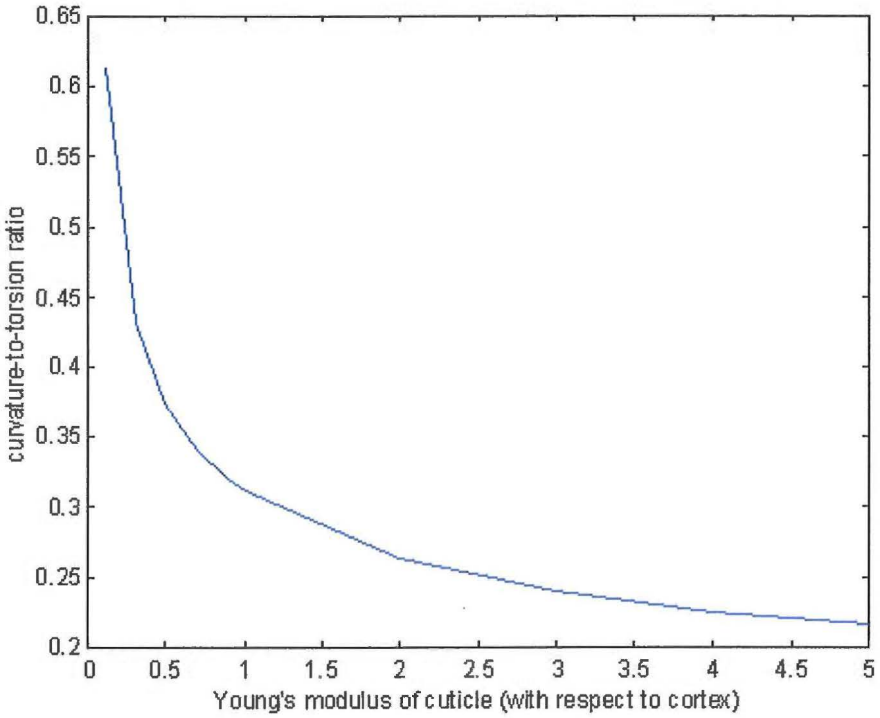

Figure 39: Fibre curvature-to-torsion ratio versus Young's modulus of cuticle (with respect to cortex)

The results are quite similar to those of the basic model with cuticle. It can be seen that an improvement of the curvature-to-torsion ratio is really large compared with the macrofibril alone, but with the Young's modulus greater than 1, it still has quite a low curvature-to-torsion ratio. As this simulation model includes more detail and sensible structures, it is expected that it will improve with more experimental data and modifications of the assumptions and the model.

5 Continuum model

5.1 Introduction

In the two previous models, the wool fibre is constructed in a discrete approach. To find the resulting geometry of the wool fibres which can attain the minimum strain energy state, the strain energy of each IF is calculated individually and the total sum of the energy of all of the IFs is minimised. It is simple to calculate the strain energy of the para-cortical or meso-cortical IFs. However, refer to equation (3.6), the deformed arc length of an ortho-cortical IF is consisted with an elliptic integral, which cannot be solved analytically. Instead, numerical integration methods are needed in the simulation. In macrofibril model, there is an integration in the strain energy equation in each IF. Therefore, there are over ten thousands of integrations are computed to calculate the total strain energy of a wool fibre. In the continuum model, there is only one multi-variable integration in each kind of cortex. The number of the computation should be largely reduced. To improve the efficiency of the algorithm, a continuous formulation is used. Hence, the summation of the strain energy will be replaced by an integral of the density of the strain energy with respect to the cross-sectional areas of the cortices.

5.2 Mathematical model

Based on the concept and the assumptions of the basic model (refer to chapter 3), a wet wool fibre is modelled as a cylinder with radius R_w and length L originally. Like the basic model, only one IF will be consisted within each macrofibril. During water desorption, lateral dilation γ applied and the minimum strain energy state is attained. From equation (3.3), an equation will be modified to calculate the strain energy density instead of finding the

strain energy of a single IF. Hence, the deformed arc length of a helical IF is

$$\begin{aligned}\tilde{L}_{\mathrm{o}} &= \int_0^{\rho L}\left|\frac{\mathrm{d}\mathbf{h}_{\mathrm{o}}}{\mathrm{d}s}\right|\mathrm{d}s \\ &= \int_0^{\rho L}\Big(\Big[1-\kappa(\tilde{d}_{\mathrm{o}}\cos(\theta_{\mathrm{o}}-\theta)+\tilde{r}\cos(\omega s-\theta))\Big]^2 \\ &\quad +\Big[\tilde{r}\omega\sin(\omega s-\theta)+\tau(\tilde{d}_{\mathrm{o}}\sin(\theta_{\mathrm{o}}-\theta)+\tilde{r}\sin(\omega s-\theta))\Big]^2 \\ &\quad +\Big[\tilde{r}\omega\cos(\omega s-\theta)+\tau(\tilde{d}_{\mathrm{o}}\cos(\theta_{\mathrm{o}}-\theta)+\tilde{r}\cos(\omega s-\theta))\Big]^2\Big)^{\frac{1}{2}}\mathrm{d}s, \end{aligned} \tag{5.9}$$

where $\tilde{L}_{\mathrm{o}}$ beside is a function of κ, τ, ρ and θ, it also depends on $\tilde{d}_{\mathrm{o}}$ and θ_{o}. $\left(\tilde{d}_{\mathrm{o}},\theta_{\mathrm{o}}\right)$ is the polar coordinates of the position of the generating curve of the helical IFs on the cross-section of the fibre. Suppose the macrofibrils are packed in a square lattice pattern, the packing fraction η_{o} of the macrofibrils will be equal to $\frac{\pi}{4}$. Subsequently, the strain energy density of the helical IFs is

$$\mathrm{d}e_{\mathrm{o}} = \frac{1}{2}\frac{E_{\mathrm{o}}}{L_{\mathrm{o}}}\left(L_{\mathrm{o}}-\tilde{L}_{\mathrm{o}}\right)^2\mathrm{d}A.$$

Let A_{o} be the cross-sectional area of the ortho-cortex; the total strain energy induced by ortho-cortical IFs is

$$e_{\mathrm{o}} = \int\int_{A_{\mathrm{o}}}\frac{1}{2}\frac{\eta_{\mathrm{o}}E_{\mathrm{o}}}{L_{\mathrm{o}}}\left(L_{\mathrm{o}}-\tilde{L}_{\mathrm{o}}\right)^2\mathrm{d}A.$$

From equation (3.2), the deformed arc length of a para-cortical IF is

$$\tilde{L}_{\mathrm{p}} = \rho L\sqrt{\left(1-\tilde{d}_{\mathrm{p}}\cos(\theta_{\mathrm{p}}-\theta)\kappa\right)^2+\left(\tilde{d}_{\mathrm{p}}\tau\right)^2},$$

and the strain energy density of para-cortex with packing fraction $\eta_{\mathrm{p}} = \frac{1}{3}\eta_{\mathrm{o}}$, which reflects the lesser density of IFs in para-cortex, is

$$\mathrm{d}e_{\mathrm{p}} = \frac{1}{2}\frac{E_{\mathrm{p}}}{L_{\mathrm{p}}}\left(L_{\mathrm{p}}-\tilde{L}_{\mathrm{p}}\right)^2\mathrm{d}A.$$

Suppose the cross-sectional area of the para-cortex is A_{p}, the total strain energy in para-cortex is

$$e_{\mathrm{p}} = \int\int_{A_{\mathrm{p}}} \frac{1}{2}\frac{E_{\mathrm{p}}}{L_{\mathrm{p}}}\left(L_{\mathrm{p}} - \tilde{L}_{\mathrm{p}}\right)^2 \mathrm{d}A.$$

Correspondingly, in meso-cortex, the deformed arc length of a IF is

$$\tilde{L}_{\mathrm{m}} = \left(1 - \tilde{d}_{\mathrm{m}}\cos(\theta_{\mathrm{m}} - \theta)\kappa\right)^2 + \left(\tilde{d}_{\mathrm{m}}\tau\right)^2.$$

The strain energy density of meso-cortex with packing fraction $\eta_{\mathrm{m}} = \eta_{\mathrm{o}}$ is

$$\mathrm{d}e_{\mathrm{m}} = \frac{1}{2}\frac{E_{\mathrm{m}}}{L_{\mathrm{m}}}\left(L_{\mathrm{m}} - \tilde{L}_{\mathrm{m}}\right)^2 \mathrm{d}A,$$

and the total strain energy of the meso-cortex with cross-sectional area A_{m} is

$$e_{\mathrm{m}} = \int\int_{A_{\mathrm{m}}} \frac{1}{2}\frac{E_{\mathrm{m}}}{L_{\mathrm{m}}}\left(L_{\mathrm{m}} - \tilde{L}_{\mathrm{m}}\right)^2 \mathrm{d}A.$$

The total strain energy of the wool fibre during water desorption is

$$e_{\mathrm{w}} = e_{\mathrm{o}} + e_{\mathrm{p}} + e_{\mathrm{m}}.$$

By differentiating the above equation with respect to κ, τ, ρ and θ, the shape of the fibre attains minimum strain energy state can be ascertained.

5.3 Results

With a 50:50 split of ortho-and-para-cortex pattern, the pitch angle of ortho-cortical IFs $\phi = 30°$ and lateral contraction $\gamma = 0.1$, the numerical simulation yields,

$$\kappa = 1.80 \text{ mm}^{-1},$$

$$\tau = 8.45 \text{ mm}^{-1},$$

$$\rho = 1.01 \ ,$$

$$\theta = \frac{3\pi}{2} \ ,$$

$$a = 0.02 \ \mu\text{m} \ ,$$

$$c = 0.11 \ \mu\text{m} \ ,$$

$$\kappa : \tau = 0.21 \ .$$

The curvature-to-torsion ratio seems lower than the result of the basic model with the same configuration. The cause may be similar to the macrofibril model, it dues to the IFs near the centres of the macrofibrils which need high energy to elongate the arc lengths. It can be improved by introducing cuticle into the model. Given the thickness of the cuticle shell is 0.1 μm, Young's modulus is 1 (relative to the cortex) and $\nu = 0.5$, the new results are

$$\kappa = 0.84 \ \text{mm}^{-1} \ ,$$

$$\tau = 1.34 \ \text{mm}^{-1} \ ,$$

$$\rho = 1.01 \ ,$$

$$\theta = \frac{3\pi}{2} \ ,$$

$$a = 0.33 \ \mu\text{m} \ ,$$

$$c = 0.53 \ \mu\text{m} \ ,$$

$$\kappa : \tau = 0.62 \ .$$

These results are quite different from the results in the macrofibril model, although, it was developed from the macrofibril model. It may be caused by the addition of packing faction in the continuum model and it is of course impossible to put in infinite number of IFs inside the fibre in the practical situation.

6 Fibre shape measurement

6.1 Introduction

Experimental data is required to verify the mathematical model's predictions. In this chapter, a method for measuring the curvature and torsion of wool fibres is described, in particular that of "free" wool fibres, which are as free as possible from external influences.

Photography is an ideal way of determining a fibre's shape since its shape can be changed easily by any physical contact, even airflow. Various photographic projections of a fibre are taken and from each of these images the fibre's space curve can be reconstruction. A large amount of image processing is required during this reconstructed: various techniques have been devised and the one that was found to be most efficient is described here. Finally, curvature and torsion along the fibre can be calculated using the 3D coordinates.

Eighteen Perendale wool fibres were analysed. Perendale is chosen here for it is medium class wool, which has both high crimp and low crimp fibres. Comparing wool fibre from a single sheep breed may be helpful to reduce some unknown different factors between sheep breeds. Nine of the 18 were taken from the fleece of one sheep and nine from another sheep. The 18 fibres were not chosen at random since it was felt that experimental errors might swamp the results for very straight fibres, and the image processing was too difficult for highly convoluted fibres.

6.2 Capturing the images

Sample fibres are cleaned in solvent to remove grease. Then they are steamed and allowed to dry slowly. This process is known to return the fibre to a shape close to that found in the fleece.

The fibre is placed in a glass chamber so that the closed space inside pro-

vides a stable environment which prevents any fibre movement when taking the photographs. The chamber is shaped like a hexagonal glass prism with its axis vertical. It is 6.5 cm tall and each side is 2.5 cm wide. It stands on a base which can be rotated smoothly about a vertical axis. The glass chamber is constructed from microscope-slide glass (anti-reflection glass could be used to further reduce light dispersion to obtain sharper images in future). The chosen fibre is hung within the chamber so it roughly coincides with the chamber's vertical axis. Its top end is attached to a clip that pokes through the top cover of the chamber. The clip has a round bottom which sits in a concave depression in the top cover. This allows the clip freedom to sit on the top at many different angles, so that the fibre presents a good appearance through all six glass windows (sometimes the intersections between the glass panes may obscure parts of the fibre). The chamber is shown in Figure 40.

The photographs are taken using an SLR camera with a fixed focal-length macro lens. This is mounted on an adjustable rig which is fixed to a wooden base, and the rig is adjusted so the lens is 5-10 cm away from the prism in order to maximise the size of the fibre image. 35mm colour film is used in order to keep processing costs low.

Typical fibres occupy a significant portion of the chamber and so it is difficult to achieve the required depth of field. This problem can be overcome by taking more than one photograph for each projection, focusing on different points on the fibre. A better solution is to use the smallest possible aperture (F-stop 16). Such a small aperture requires an intense light source or a long shutter speed, usually around $\frac{1}{2}$ s.

The light source is a major concern. Uniform and diffuse light sources can reduce shadows and dim points on the fibres, and hence the variation of the greyscale of the fibre image. Two set-ups have been tested. The first one uses a fluorescent light ring in front of the camera lens and a dark background. However, with a strong light source the background becomes too bright, which reduces the contrast between the fibre and the background. The second

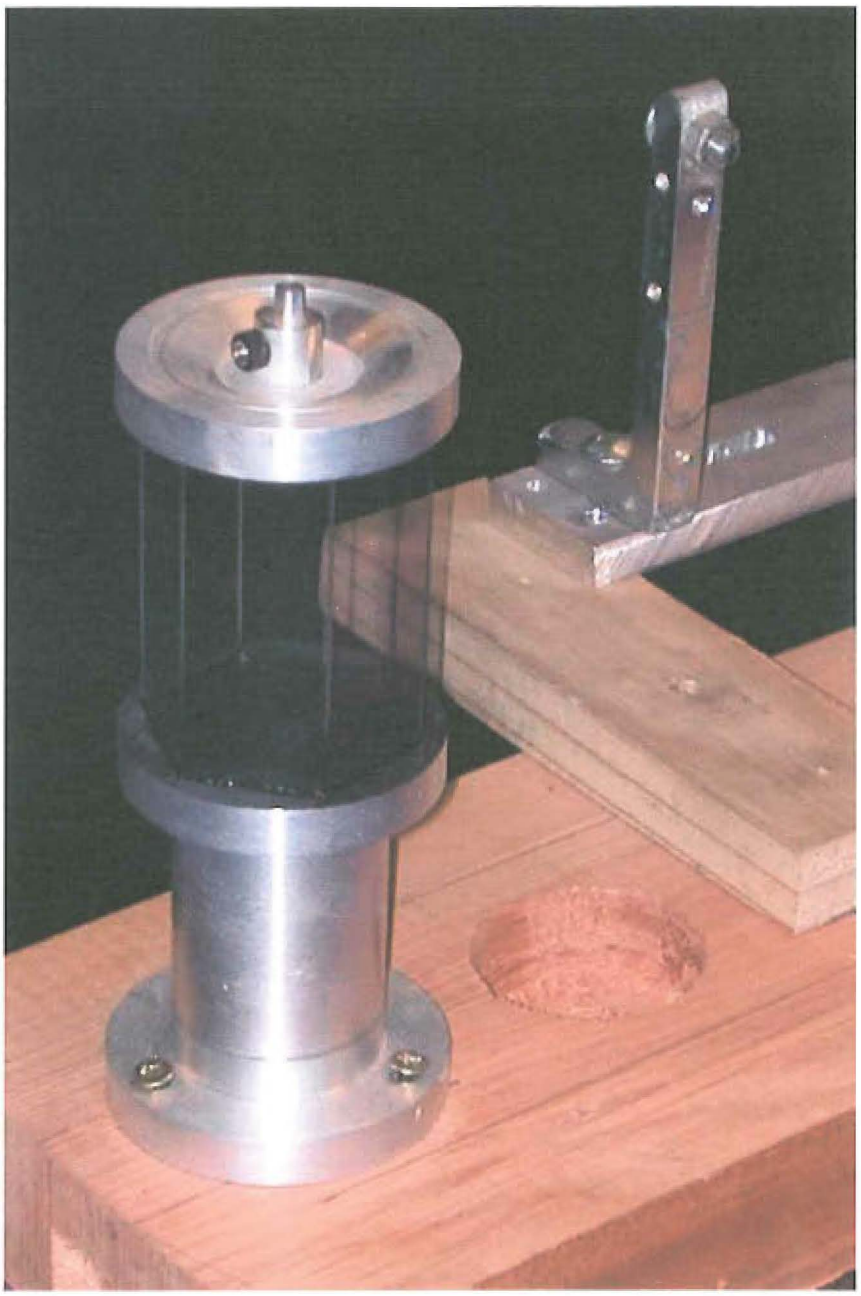

Figure 40: The glass chamber for holding fibre samples

method utilises a fluorescent light box placed behind the fibre chamber and photographing is performed in a dark room to minimise the light coming from the front, which causes shadows on the fibre. This second method essentially photographs the fibre's shadow against the bright background and it produces good contrast images with a sharp focus.

With the set-up complete, the glass chamber is rotated to a position where the plane of the glass is perpendicular to the camera axis to minimise the reflection of light. Two photographs of each of the six projections are usually taken for each fibre sample, each one of the pair focusing on a different point. After the two photos are taken for a projection, the chamber is rotated carefully by 60° until all six projections are photographed.

Objects of size around 10 μm $\times$ 10 μm can be resolved using this set-up, which is adequate for the purposes of measuring a fibre's space curve since most fibres measured are 20–30 μm in diameter. The only significant source of resolution loss is the microscope-slide prism sides. Without these sides a 30 μm diameter fibre produces an image of roughly 30 μm, while addition of the prism sides increases this to 40–50 μm.

The photographs are developed to produce photo prints that are around four times bigger than the objects. There is insignificant loss of resolution during this stage.

Finally, a 1600 dpi (dots per inch) CCD scanner is used to digitalise the images.

Digital cameras were found to be unviable. This was because their resolution was inadequate (e.g., a square array of 1000 $\times$ 1000 pixels focused on an area of 7cm $\times$ 7cm means one pixel corresponds to 70 μm $\times$ 70 μm, which compares unfavourably with the 10 μm $\times$ 10 μm achieved by an ordinary camera) and the cost was large since standard digital cameras aren't equipped with macro lenses.

6.3 Image processing

After scanning, all unnecessary information is discarded, such as colour and most of the background of the photos which can be cut away with drawing programs such as Adobe Photoshop. This helps to reduce the unwanted noise caused by the background and reduces processing time when thinning the images of the fibre curves.

At this stage, the fibre images will be a thick curve with width more than 20 pixels, with each pixel representing approximately 4 μm in the object.

The images are thresholded and then thinned to one-pixel wide line using the mathematical program Matlab. The images are read as matrices of grayscale and the entries of the matrices have values from 0 (black) to 255 (white). Pixels of values less than a certain threshold value, which depends on the individual photo, are given the value '1', otherwise they are discarded by assigning them the value '0'. Therefore, in the image-matrices '1' represents fibre body while '0' represents background. The images have clear boundaries which helps reduce the time spent thinning. A convolution is applied on the image matrices so that only pixels near the centre of the fibre body are preserved. Thinning to a one-pixel wide curve is then achieved using the 'bwmorph' function of the image package of Matlab, using the 'thin' option. After thinning undesirable hairy branches always form on the one-pixel wide curve. Unless these are very numerous they may be easily removed manually using Adobe Photoshop. All these difficulties may be reduced considerably by capturing sharp images with high contrast.

6.4 Ordering the points

After thinning, the next step is to order the points from the top of the fibre to its other end for each of the six projections of each fibre. This is done manually because reference to the original photographs was often needed to judge where the fibre was heading at the points of intersection. Also,

the "hairs" on the surface of the thinned image tend to confuse a totally automated algorithm, as did breaks in the fibre image, especially around points of intersection.

6.5 Smoothing the points

The coordinates thus obtained are naturally discrete (since they are simply a set of pixel values), so a low-pass filter may be applied to obtain a smooth fibre image. Specifically, denote the coordinate pairs of the points by (x_j, z_j), where $j = 0, \ldots, N-1$, ($N \sim 10000$ for the images in question). The linear trend in the sequence x_j may be removed via $x_j \to x_j - (jx_{N-1} + (N-1-j)x_0)/(N-1)$, and a Fourier transform of the result may be taken

$$x_j = \frac{1}{\sqrt{N}} \sum_{n=0}^{N-1} \tilde{x}_n \exp(2\pi i j n/N) \ ,$$

and similarly for z_j. Then the Fourier modes may be scaled

$$\tilde{x}_n \to \begin{cases} \left(1 - n_{\text{smooth}} \frac{n^2}{N^2}\right) \tilde{x}_n & n < N/\sqrt{n_{\text{smooth}}} \\ 0 & N/\sqrt{n_{\text{smooth}}} \leq n < N/2 \end{cases}$$

for some "number of points to smooth over" n_{smooth}. The Fourier modes for $n > N/2$ are scaled similarly (ensuring that the final result for x_j is real). After applying the inverse Fourier transform and restoring the linear trend, the result is a smoother image. It was found that a smooth curve was obtained by running this smoothing routine a few hundred times, each time setting $n_{\text{smooth}} = 3$, and then running a further few hundred times, each time setting $n_{\text{smooth}} = 30$. In this procedure the coordinates of each data point change slightly, so a limit was placed on the total shift of each data point throughout the entire smoothing processes. This limit was taken to be the typical radius of the fibre's photographic image in pixels: about 15 pixels for

most fibres.[2]

6.6 Extracting the space curve

Finally, the six different projections of each fibre may be merged together to obtain the space curve living in three dimensions. This is made difficult due to the different magnification of each segment of each fibre in each image (the camera is further away from various fibre segments than other segments), and is probably the weakest part of the whole procedure. Denote the coordinates of the points in the six fibre images by $(z(s_k), x_k(s_k))$, where $k = 1, \ldots, 6$. Here s_k is a discretised quantity but it may be trivially made continuous by spline interpolation. The construction of the space curve is made easier by noting that the beginning of the fibre (at $s_k = 0$) and the end of the fibre, as well as the points where $z'(s_k) = 0$ on each image may be identified.

To act as an aid in quantifying the error in the space-curve construction, the six images may be grouped into two groups of three images, and the space curve generated from the two groups compared. After this is done, the space curve may be also constructed from the six images using the same algorithm. The algorithm for constructing the space curve is as follows:

1. Identify the top in each photograph and shift each image so that this point has the same z value in each.

2. Scan along the fibre to find the turning points where $z' = 0$. Due to experimental errors in the photographs and image processing, some spurious turning points might be found. It is therefore important to only identify a point as a turning point if it turns by more than a given amount. It is also sometimes necessary to tune this amount 'on the fly' so as to pick out the correct turning points in each photograph.

[2]In the final analysis, although the smoothing produced a much better looking image on short scales, it made very little difference to the results because the 'scale' of measurements (defined below) was taken to be significantly larger than one pixel.

In practice, it is always easy to identify the correct turning points by comparing all three images: each image should have the same number of turning points, each of which occurs at roughly the same z value in each image.

3. Identify the end of the fibre in each photograph.

4. Each image will thereby be made up of a number of distinct segments bounded by the turning points. The vertical height (distance along the z axis) of each segment will be slightly different in each image due to differences in magnification. Denote the mean vertical height over all three images by m_s ($s = 1, \ldots$,number of segments). Piecewise scale each segment in each image so that it has a vertical height equal to m_s.

5. Choose one image to be the reference image and denote by θ_1 and θ_2 the camera angles relative to this photograph. Now that the differences in magnification have been scaled out, the reference image may be traversed, yielding values $(z(s), x(s))$. The value of the orthogonal coordinate $y(s)$ for each s may be obtained by the mean

$$y(s) = \frac{1}{2}\left(\frac{x_1(s) - x(s)\cos\theta_1}{\sin\theta_1} + \frac{x_2(s) - x(s)\cos\theta_2}{\sin\theta_2}\right) .$$

Here $x_1(s)$ is the 'horizontal' coordinate value of the point with vertical value $z(s)$ in the image at angle θ_1 to the reference, and similarly for $x_2(s)$.

6.7 Curvature and torsion

Finally, the curvature and torsion along the fibre may be calculated. Currently there are standard instruments that measure curvature of snippets of wool fibres [5, 7]. These instruments measure curvature on a macroscopic scale, that is, they approximate a wool snippet of given non-infinitesimal

length by a circular arc. Curvature and torsion are classically defined through the Frenèt formulae on infinitesimal scales, but to keep as close as possible to the current technologies, and to avoid short distance experimental errors as much as possible, the curvature and torsion of the fibre space-curves are also found at a non-infinitesimal scale.

For a piecewise linear curve, the curvature at a vertex is the reciprocal of the radius of curvature of the arc which passes through the point and its two immediate neighbours. The torsion measures the amount of non-planarity of the curve. Consider four points in 3-space $\mathbf{x}_{i-1}, \ldots, \mathbf{x}_{i+2}$, and define the vectors joining them by $\mathbf{v}_i = \mathbf{x}_i - \mathbf{x}_{i-1}$ and $\mathbf{T}_i = \frac{\mathbf{v}_i}{|\mathbf{v}_i|}$. The cross-product of the Frenét formula

$$\frac{\mathrm{d}\mathbf{T}}{\mathrm{d}s} = \kappa \mathbf{N} \ ,$$

with $\mathbf{T}$ which gives

$$\kappa = \left| \frac{\mathrm{d}\mathbf{T}}{\mathrm{d}s} \times \mathbf{T} \right| \ .$$

Each term on the RHS may be estimated in the discrete formalism. Firstly

$$\frac{\mathrm{d}\mathbf{T}}{\mathrm{d}s} \approx \frac{1}{s_i} \left(\mathbf{T}_{i+1} - \mathbf{T}_i \right) \ ,$$

where $s_i = \left| \frac{\mathbf{v}_i + \mathbf{v}_{i+1}}{2} \right|$. The unit tangent $\mathbf{T}$ at a vertex may be approximated by the average of the tangent vector before and after the vertex

$$\mathbf{T} \approx \frac{1}{2} \left(\mathbf{T}_{i+1} + \mathbf{T}_i \right) \ .$$

Then the curvature at point i is defined as

$$\begin{aligned} \kappa_i &= \left| \frac{1}{s_i} \left(\mathbf{T}_{i+1} - \mathbf{T}_i \right) \times \frac{1}{2} \left(\mathbf{T}_{i+1} + \mathbf{T}_i \right) \right| \\ &= \frac{|\mathbf{v}_i \times \mathbf{v}_{i+1}|}{|\mathbf{v}_i| \, |\mathbf{v}_{i+1}| \, |(\mathbf{v}_1 + \mathbf{v}_{i+1})/2|} \ . \end{aligned}$$

This formula has been constructed so that it has the greatest possible sym-

metry; specifically there is invariance under interchange of the notion of 'forwards' and 'backwards'. Similarly, the cross product of the Frenét formula,

$$\frac{\mathrm{d}\mathbf{B}}{\mathrm{d}s} = -\tau\mathbf{N} \ ,$$

with $\mathbf{B}$ yields

$$\tau = -\left|\frac{\mathrm{d}\mathbf{B}}{\mathrm{d}s} \times \mathbf{B}\right| \ .$$

To rewrite the formula into a discrete form,

$$\frac{\mathrm{d}\mathbf{B}}{\mathrm{d}s} \approx \frac{1}{s_i}\left(\mathbf{B}_{i+1} - \mathbf{B}_i\right) \ ,$$

where it becomes appropriate to now use $s_i = |\mathbf{v}_i|$, and

$$\mathbf{B} \approx \frac{\mathbf{1}}{\mathbf{2}}\left(\mathbf{B_{i+1}} + \mathbf{B_i}\right).$$

The binormal vector can be found from the relations, $\mathbf{B} = \mathbf{T} \times \mathbf{N}$ and $\mathbf{N} = \frac{1}{\kappa}\frac{\mathrm{d}\mathbf{T}}{\mathrm{d}\mathbf{s}}$. Some algebra reveals that the torsion between the point i and $i+1$ is

$$\tau_{i,i+1} = \frac{\left(\mathbf{v}_i \times \mathbf{v}_{i+1}\right) \cdot \mathbf{v}_{i+2}}{\left|\mathbf{v}_i \times \mathbf{v}_{i+1}\right| \left|\mathbf{v}_{i+1} \times \mathbf{v}_{i+2}\right|} \ .$$

Again this is the most symmetric form possible.

A representative example of the curvature and torsion as a function of arc length is shown in Figure 41. This result was measured at a 'scale' of 1mm. This means that the curvature at each of the roughly 14000 experimentally-measured data points that describe this fibre's space curve was found in the following way. Take a particular point, with coordinates denoted by $\mathbf{x}_i$, then move a distance 1mm backwards along the space curve from this point to find the coordinates $\mathbf{x}_{i-1}$, and move a distance 1mm forwards along the curve to find $\mathbf{x}_{i+1}$. Then apply formula Equation 6.10. A similar procedure is used to find torsion at each of the points. The curvature and torsion cannot be

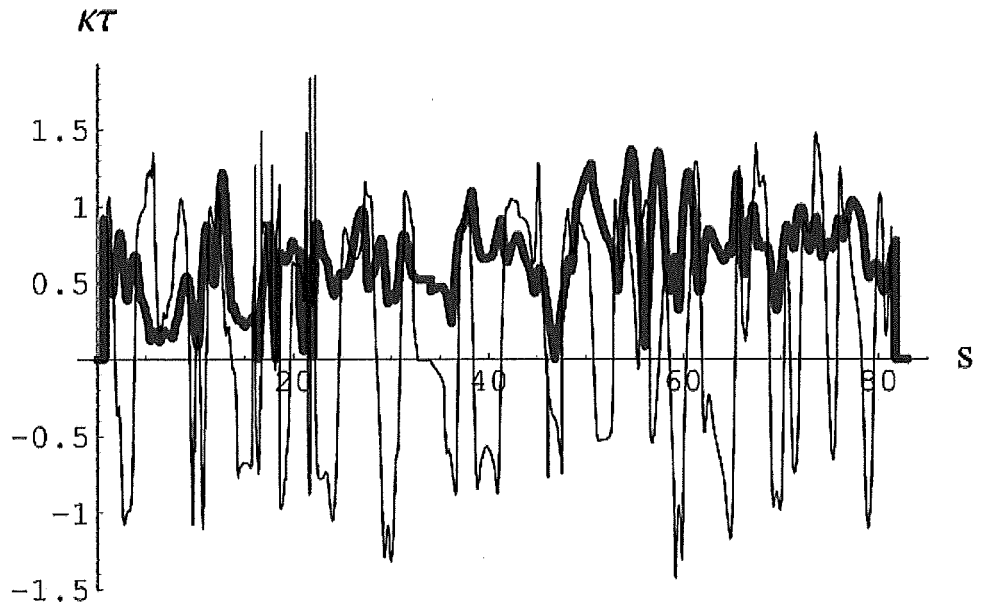

Figure 41: The measurements of curvature and torsion with respect to arc length s (mm), where the bold line is curvature and the thin line is torsion

defined for points close to the ends of the fibre. The OFDA machine also measures curvature at a scale of 1mm.

6.8 Examples

Three examples are given here. The original images and a thinned images of the parts of three fibres are given as Figures 42 to 47. The coordinates of the pixel of the thinned curves and the calculated curvature and torsion along the fibre can then be obtained. The next chapter will show the methods to measure the cross-sectional pattern of the cortical cells and how to use the data and the mathematical model to estimate the local curvature and torsion of the fibres.

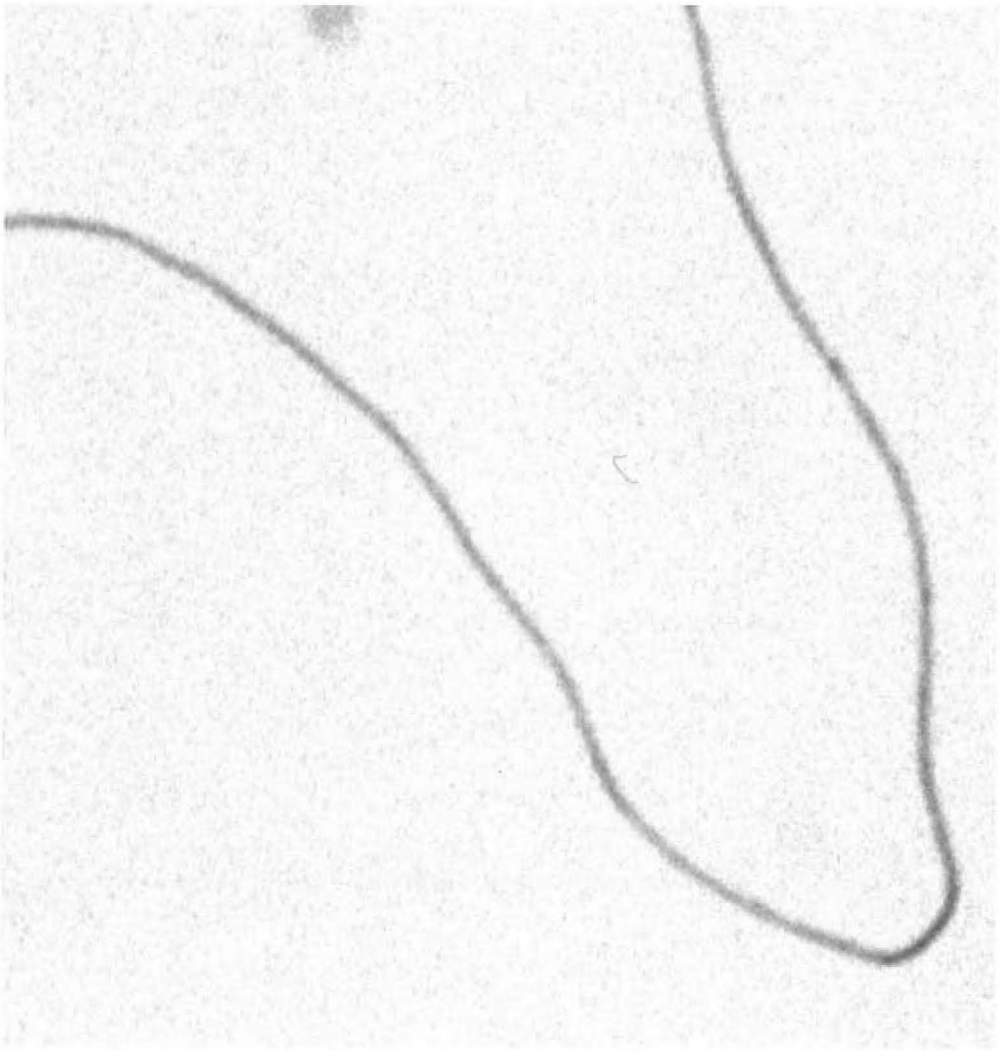

Figure 42: The original photo of a part of fibre A

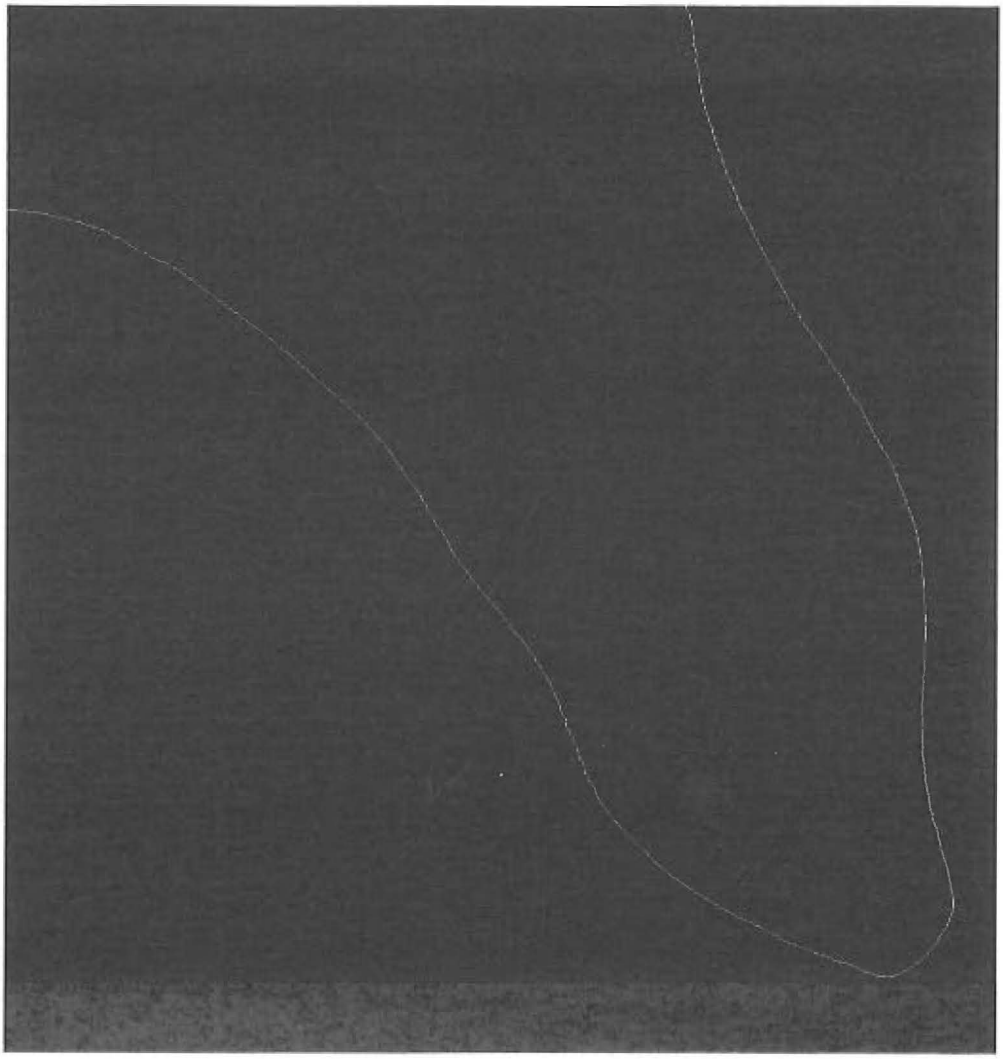

Figure 43: The thinned one-pixel wide image of fibre A

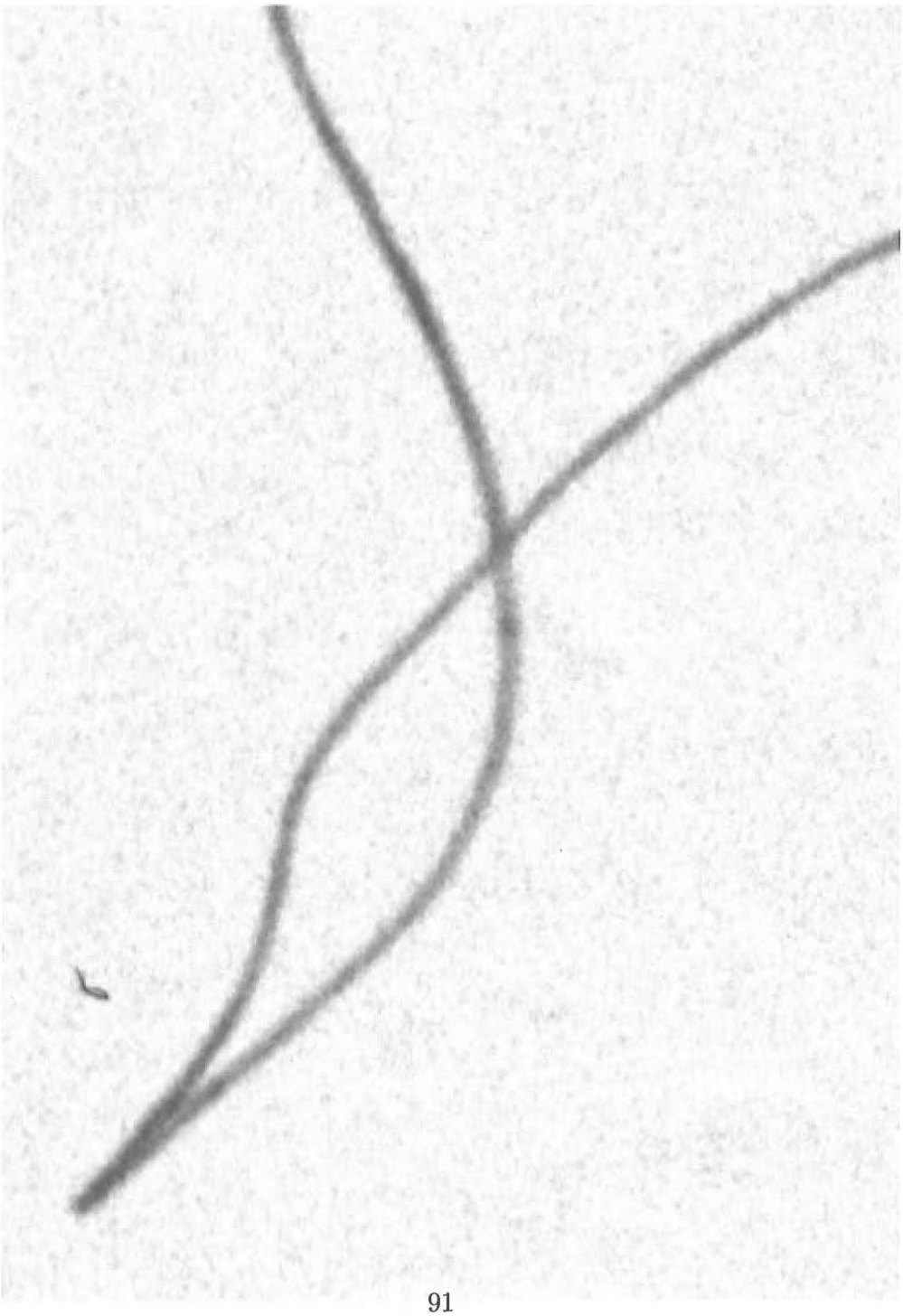

Figure 44: The original photo of a part of fibre B

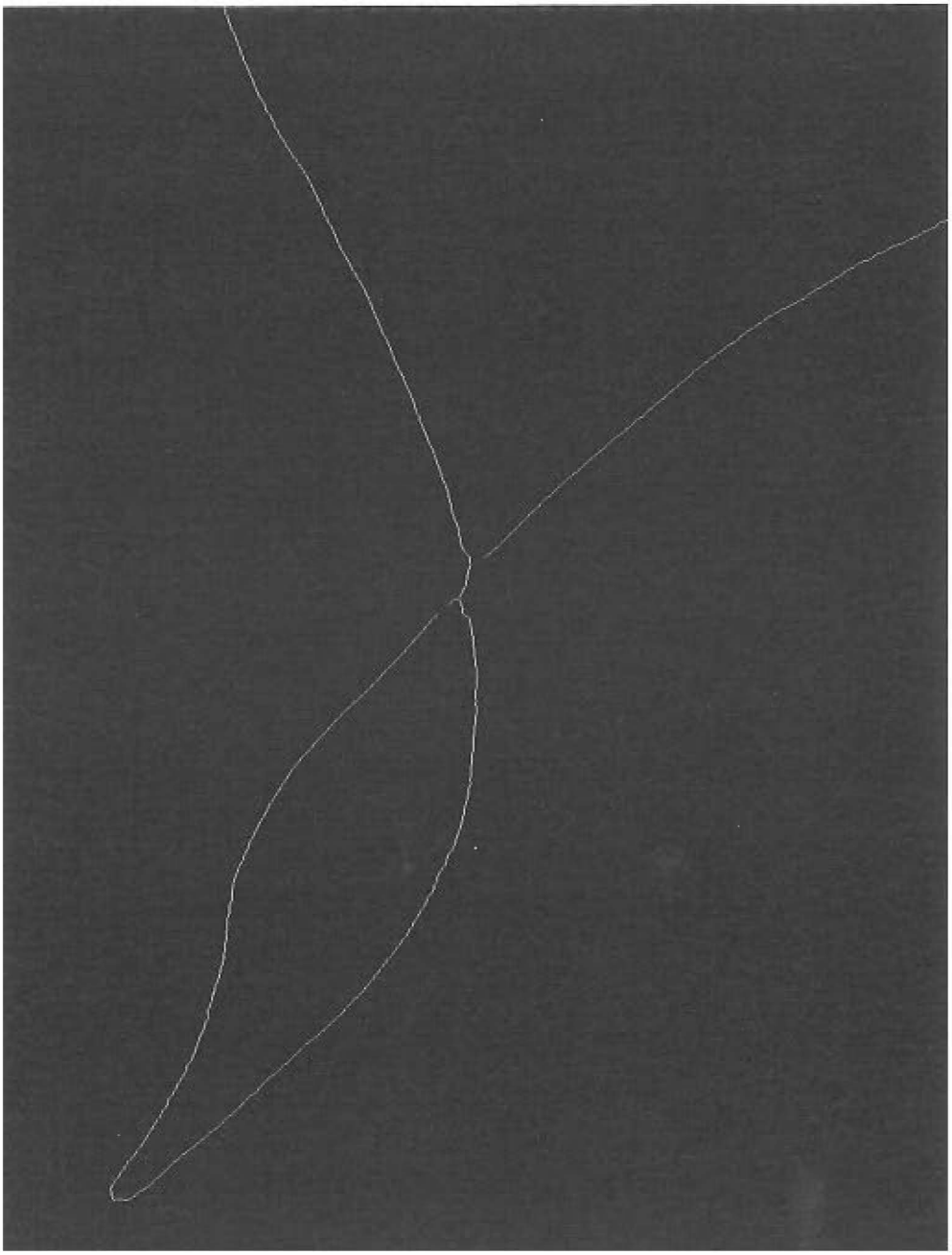

Figure 45: The thinned one-pixel wide image of fibre B

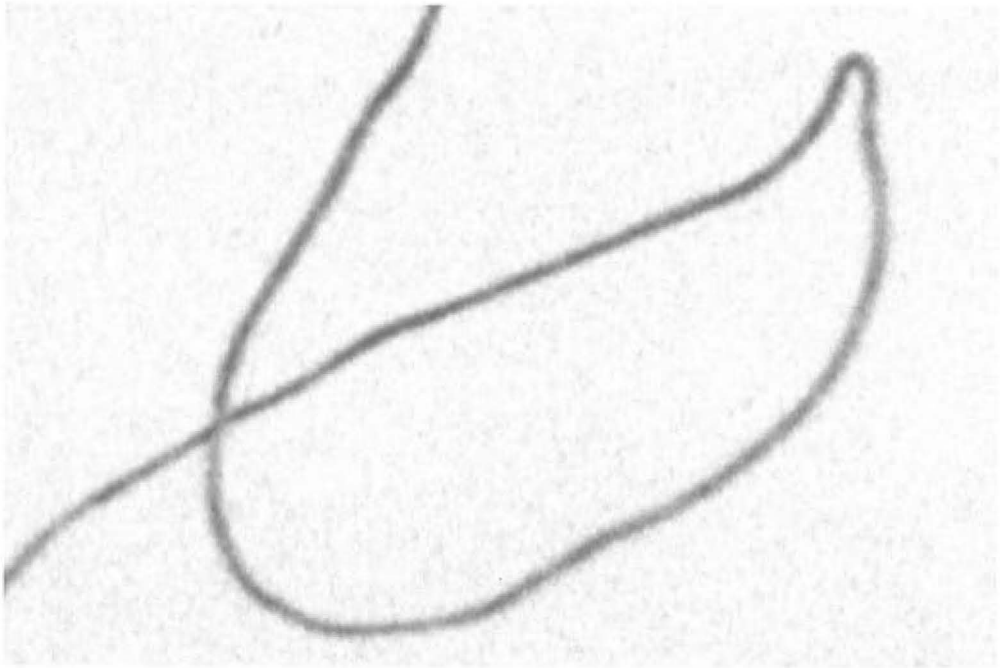

Figure 46: The original photo of a part of fibre C

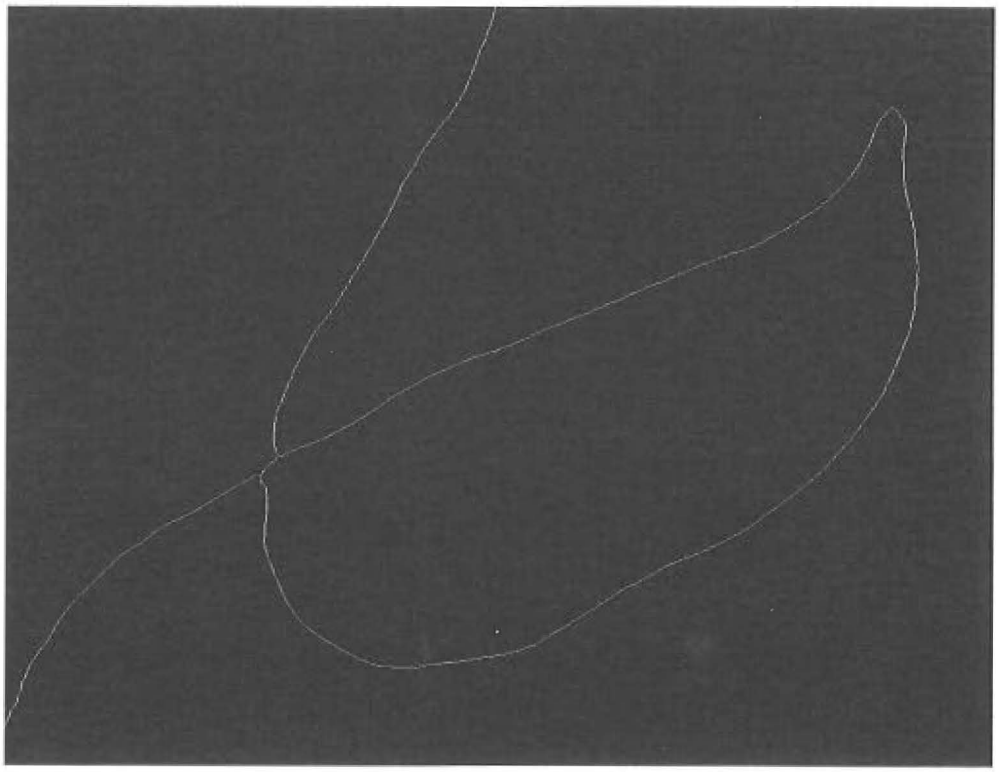

Figure 47: The thinned one-pixel wide image of fibre C

6.9 Analysis of the data obtained

This section is based on material published in [14].

Fibre shape is an important factor in many textile processing operations (such as carding yield and throughput) as well as end-user applications. Fibre shape is also an important ingredient in realistic theoretical models of such operations and applications.

A visual estimate of crimp [1] is the most commonly used measure of shape, but it is generally accepted that it is not a complete descriptor of processability or end-product performance. One potential reason for this is that crimp, and other automated measurements of fibre curvature [8], such as OFDA [5] and Sirolan-Laserscan [7] measurements, do not capture the three-dimensional nature of fibre shape.

To the author's knowledge, the explicit mathematical nature of fibre shape is poorly understood: it is not known what information is not captured by measuring curvature alone. The aim of this section is to understand more fully the nature of fibre shape in order to suggest practical ways to obtain any 'missing' information either by alternative measurement techniques or alternative uses of information obtained from current techniques, and in the process build a theory of fibre shape that would be useful for future theoretical modelling.

The results are only preliminary due to the small sample size (only 18 fibres have been photographed), but interesting results are obtained nevertheless.

6.9.1 Relationship between various moments of curvature and torsion

Figure 41 demonstrates that curvature and torsion fluctuate considerably about their mean values for each fibre. This is the generic behavior for Perendale wool fibres: by observing fibres from a handy woollen garment, the reader will readily agree that no fibres are substantially helical, which is

the constant-curvature, constant-torsion situation.

Moreover, the mean curvature is non-zero, but the mean torsion is close to zero.

Comparing results from all the fibres measured, it is found that the mean curvature $\bar{\kappa}$, and the RMS curvature $\sqrt{\overline{\kappa^2}}$ enjoy a linear relationship:

$$\sqrt{\overline{\kappa^2}} \approx 1.1\bar{\kappa} \,, \tag{6.10}$$

for a scale of 1 mm. This is shown in Figure 48, in which it is also clear that the same relation holds for fibres from both sheep. A similar linear relation holds for all scales.

A similar relation holds between the RMS torsion ($\sqrt{\overline{\tau^2}}$) and the mean magnitude of torsion ($\overline{|\tau|}$):

$$\sqrt{\overline{\tau^2}} \approx 1.2\overline{|\tau|} \,, \tag{6.11}$$

again for a scale of 1mm. This is depicted in Figure 49 and a similar result holds at all scales. However, the reader may note that this relationship is less statistically significant than the analogous result for curvature, since all quantities related to torsion vary very little over the entire sample. There is an outliner in the plot, it may be caused by a straight fibre, which has high torsion.

6.9.2 A Fourier analysis

A discrete Fourier transform of the values of curvature at equally spaced points along the fibre κ_n, $n = 0, \ldots, N-1$ ($N \approx 14000$ for Figure 41) and torsion τ_n, is used to analyse the results further:

$$\kappa_n = \frac{1}{\sqrt{N}} \sum_{j=0}^{N-1} \tilde{\kappa}_j e^{2\pi i j n/N} \quad \text{and} \quad \tau_n = \frac{1}{\sqrt{N}} \sum_{j=0}^{N-1} \tilde{\tau}_j e^{2\pi i j n/N} \,.$$

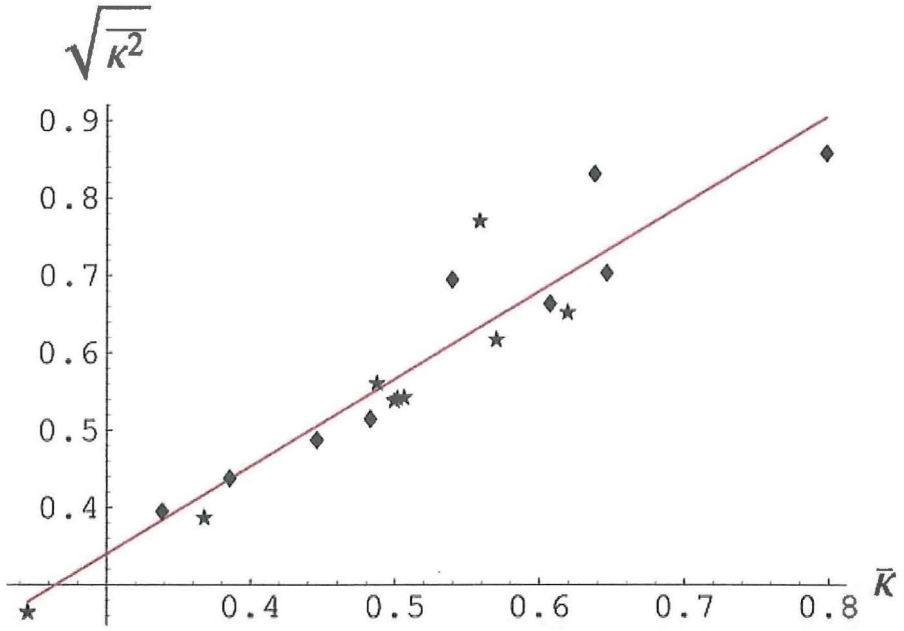

Figure 48: The rms curvature (in mm^{-1}) versus the mean curvature (in mm^{-1}). The results from fibres from the two different sheep are distinguished by stars and diamonds, but follow the same linear trend.

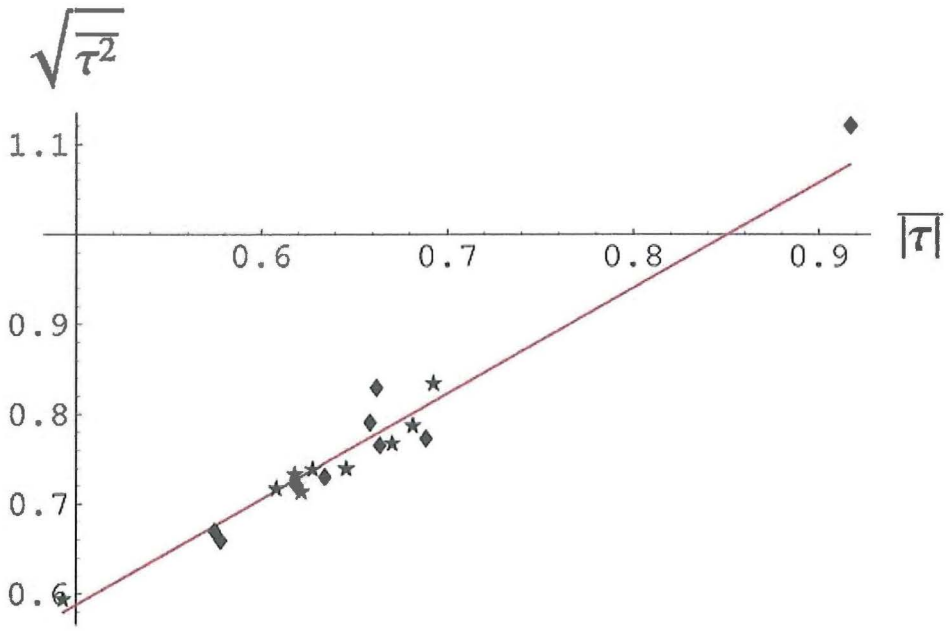

Figure 49: The rms torsion (in mm^{-1}) versus the mean magnitude torsion (in mm^{-1})

Since κ and τ are real functions, $\tilde{\kappa}_0$ and $\tilde{\tau}_0$ are real, while $\tilde{\kappa}_j = \tilde{\kappa}^*_{N-j-1}$ and $\tilde{\tau}_j = \tilde{\tau}^*_{N-j-1}$. In the following discussion, only the modes with $j \leq N/2$ are considered.

The result expressed in Equation (6.10) indicates that $\tilde{\kappa}_0$ is much greater than all the other $|\tilde{\kappa}_j|$. Similarly, the result of Equation 6.11 indicates that a Fourier decomposition of $|\tau|$ would have a large constant term (with zero phase), which suggests that the power spectrum of τ is peaked around one particular frequency. Moreover, because $\bar{\tau}$ is small, this frequency is not zero.

These observations are supported by an examination of the power spectra shown in Figures 50 and 51. It is the small frequency behavior that is of interest here, since, as noted above, the scale of typical fluctuations is large and, besides, high-frequency modes tend to be overcome by experimental noise, especially from the thinning and smoothing processes. (However, readers familiar with analysing other power spectra found in nature [2] might be amused to know that the high-frequency modes follow a power law with exponent very close to -1.)

The low-frequency behavior can be adequately modelled by

$$\begin{aligned} \tilde{\kappa}_0 &= \sqrt{N}\bar{\kappa} \quad \text{and} \quad |\tilde{\kappa}_j| = a_\kappa \exp(-b_\kappa j/L) \quad \text{for} \quad 0 < j < N/2 \,, \\ \tilde{\tau}_0 &= \sqrt{N}\bar{\tau} \quad \text{and} \quad |\tilde{\tau}_j| = a_\tau \exp(-b_\tau j/L) \quad \text{for} \quad 0 < j < N/2 \,. \end{aligned} \tag{6.12}$$

Here L is the length of the fibre (so that j/L is a 'frequency') and the dimensionful constants a_κ, b_κ, a_τ and b_τ are all positive and may be different for each fibre.

By fitting the power spectra with the above functions for each fibre, it is found that a_κ is directly proportional to the product of the standard deviation $\sigma(\kappa) = \sqrt{\overline{\kappa^2} - \bar{\kappa}^2}$ with the square-root of the fibre's length,

$$a_\kappa \approx 1.4\sqrt{N/L}\,\sigma(\kappa) \,, \tag{6.13}$$

as shown in Figure 52 for a scale of 1mm (all dimensionful quantities are

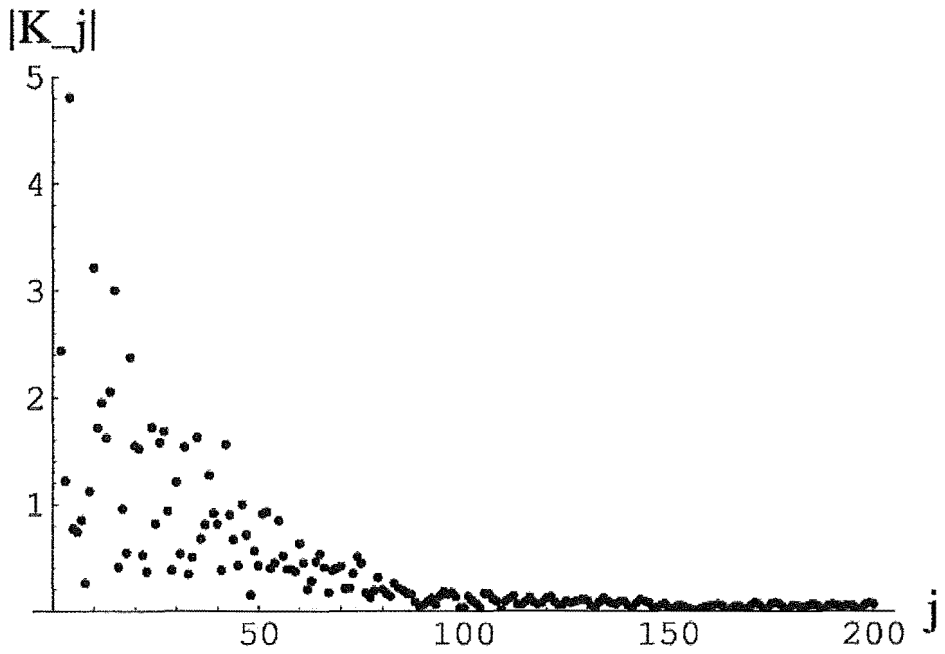

Figure 50: $|\tilde{\kappa}_j|$ as a function of j for $j > 0$ is roughly exponential with a power-law tail. For this particular example, $\tilde{\kappa}_0 = 40.7$ mm^{-1} but this point is not plotted.

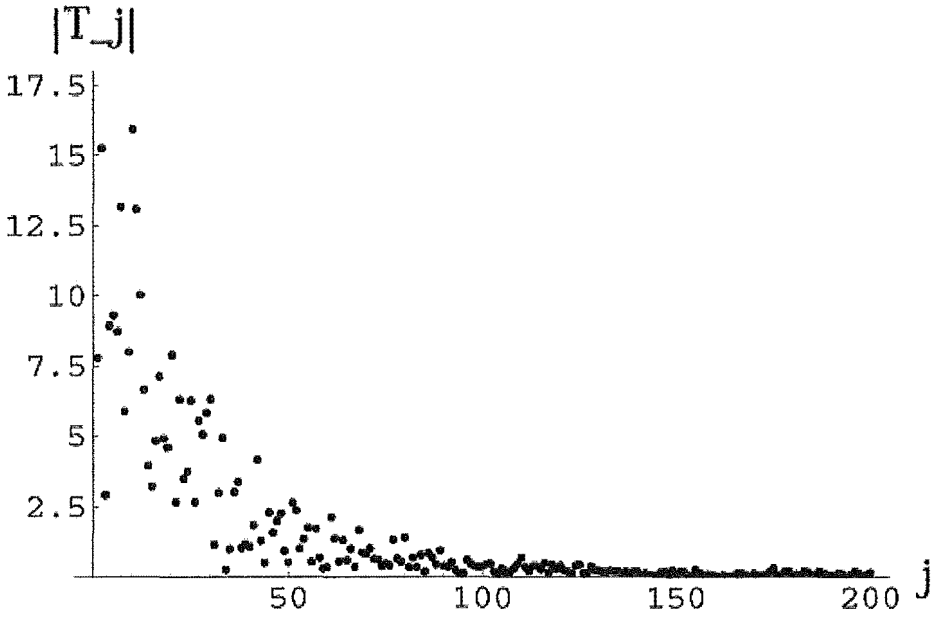

Figure 51: $|\tilde{\tau}_j|$ as a function of j

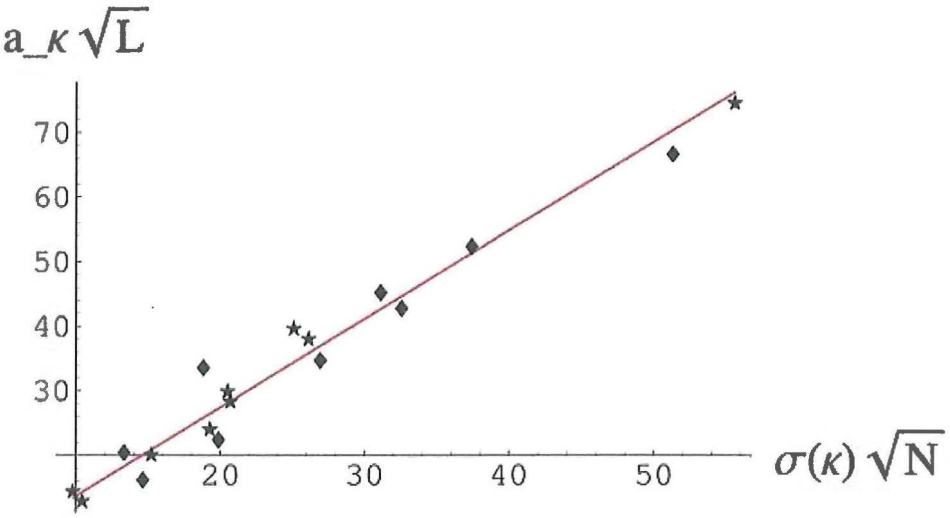

Figure 52: The parameter $a_\kappa\sqrt{L}$ (mm^{-1}) as a function of the scaled standard deviation of curvature, $\sigma(\kappa)\sqrt{N}$ (mm^{-1}) .

measured in mm). This is not completely unexpected since a_κ parameterises the fluctuations of κ about its mean. However, it is conceivable that the dimensionful numerical factor $1.4\sqrt{\mathrm{mm}}$ is an invariant of sheep breed.

The phase of each frequency mode was found to be entirely random for all scales considered. This is important for the generating algorithm below. However, in less than 50% of the fibres there was a positive correlation (where the phases were similar) or a negative correlation between the phase of $\bar{\kappa}_j$ and $\bar{\tau}_j$.

6.9.3 Torsion

The results do not indicate there is any strong correlation between the curvature and the torsion of the fibre. Observing such a relationship, if it exists, is frustrated by the fact that all quantities related to torsion are rather uniform over the entire sample of fibres studied. For instance, the plot of a_τ versus $\tilde{\kappa}_0$

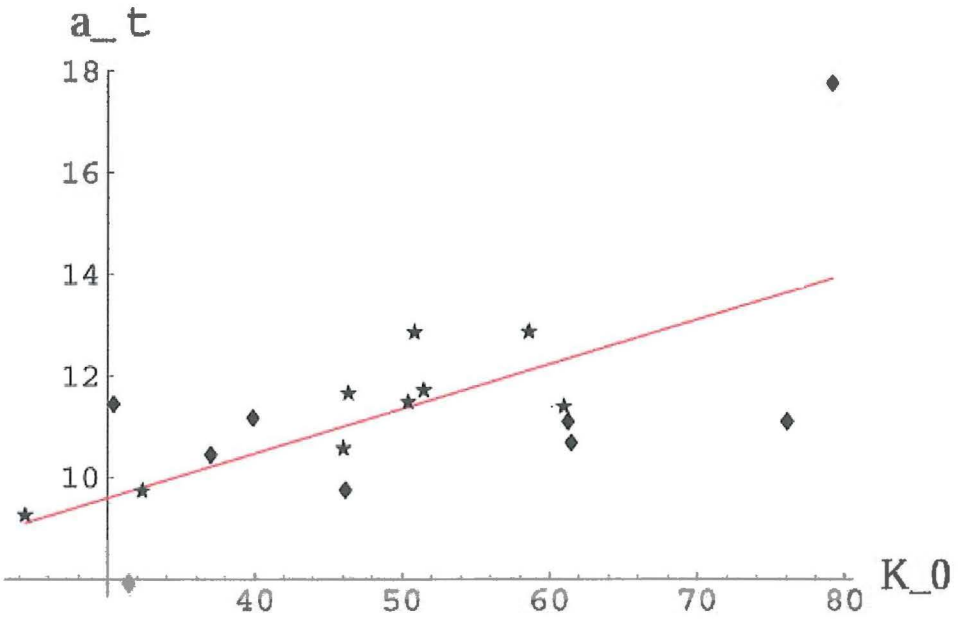

Figure 53: a_τ (mm^{-1}) as a function of $\tilde{\kappa}_0$ (mm^{-1})

shown in Figure 53 suggests that $a_\tau \approx 7.0 + 0.09\tilde{\kappa}_0$: in other words, there is little correlation between these two variables. Figure 54 shows a scatter-plot of a_τ and b_τ for all the fibres studied.

6.9.4 Generating realistic fibre shapes on a computer

The empirical relations found above may be taken as a basis for a model of fibre shape. Therefore, given the unknowns in the power spectra of Equation 6.12, random phases may be chosen for each mode κ_j and τ_j and an inverse FFT may be used to find curvature and torsion as a function of arc length. Given an initial point in space and a direction, the space curve of the fibre may be generated.

The inputs to the procedure are $\bar{\kappa}$, $\sqrt{\overline{\kappa^2}}$, and $\bar{\tau}$ if required. However, the latter may be taken to be small (yielding, say, $\sqrt{N}\bar{\tau} = \tilde{\tau}_0 = \frac{1}{10}a_\tau e^{-b_\tau}$),

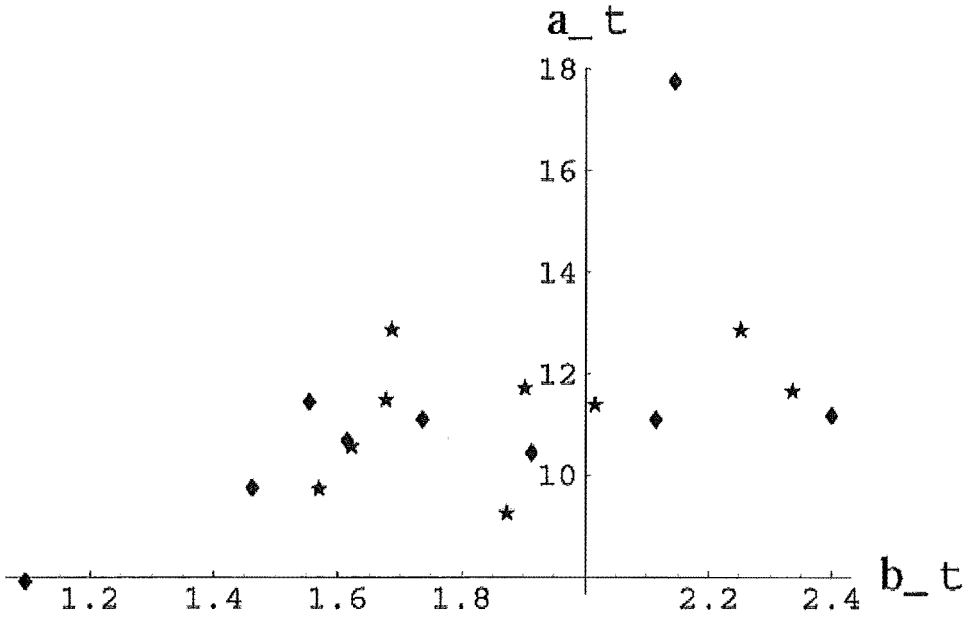

Figure 54: a_τ (mm^{-1}) as a function of b_τ

or even zero. The constant a_κ may be found directly from Equation 6.13. Parseval's theorem yields

$$N\overline{\kappa^2} = \tilde{\kappa}_0^2 + 2\sum_{j=1}^{N/2} a_\kappa^2 e^{-2b_\kappa j/L} \approx \tilde{\kappa}_0^2 + \frac{2a_\kappa^2}{e^{2b_\kappa/L} - 1} \,.$$

Taken in conjunction with other formulae, this yields $2b_\kappa/L \approx \log(1 + 2 \times 1.4^2/L)$.

Since the fibres' torsional properties were found to be independent of their curvature and were similar for all fibres, a_τ and b_τ may be chosen arbitrarily within reasonable limits suggested by Figure 54.

If this procedure yields points of negative curvature, another random data set may be generated, or it may be noted that a space curve of negative curvature $-|\kappa|$ and torsion τ, is physically indistinguishable from a curve with positive curvature $+|\kappa|$ and torsion $-\tau$. The effect of this sign change on the power spectra is very small and certainly within the accuracy of the whole procedure.

An example of a computer-generated fibre's curvature and torsion is shown in Figure 55. Here $\bar{\kappa} = 0.64\text{mm}^{-1}$ and $\sqrt{\overline{\kappa^2}} = 0.70\text{mm}^{-1}$ were chosen with $N = 14000$ and the fibre length of L =83mm. The above formulae give $\tilde{\kappa}_0 = 41\text{mm}^{-1}$, $a_\kappa = 5.0\text{mm}^{-1}$ and $b_\kappa = 1.8\text{mm}$. The torsional parameters $a_\tau = 11\text{mm}^{-1}$ and $b_\tau = 2.3\text{mm}$ were chosen. Therefore, this fibre should be similar to the one depicted in Figure 41.

6.9.5 Summary and Discussion

This section reported on the results of the experimental work which measured the space curve of 18 free Perendale wool fibres. It was shown that the power spectrum of curvature and torsion could be well approximated by exponentials. Moreover, curvature, including all its statistical fluctuations along the fibre's length, seems to be completely parameterised in terms of its mean and RMS values. The torsional properties of the fibres were found

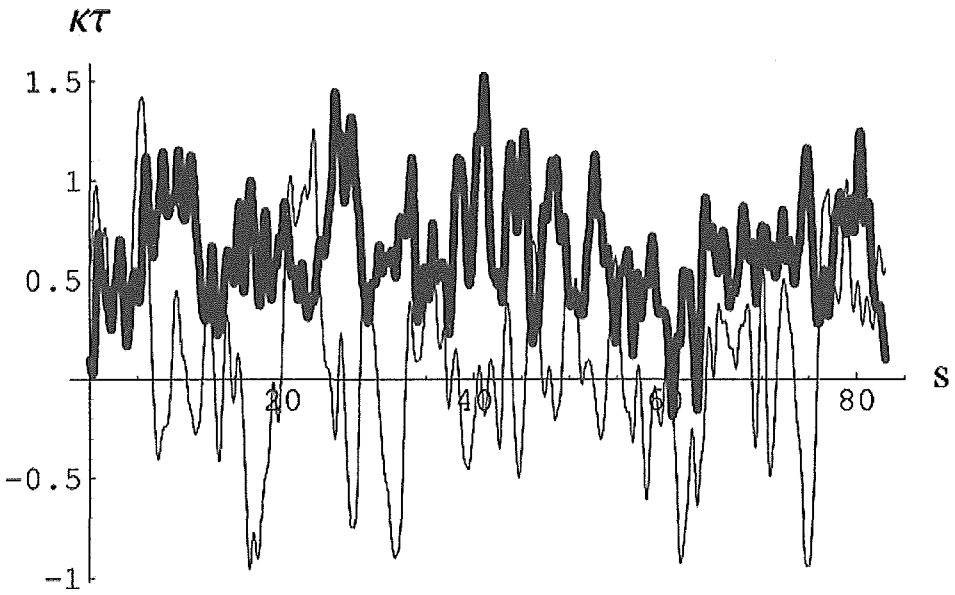

Figure 55: κ (bold) and τ (both measured in mm^{-1}) as a function of arc length s (in mm) generated by the procedure described in the text.

to be comparatively constant. The phases of the spectra were random and largely uncorrelated between the same modes of curvature and torsion. A procedure for rapid computer simulation of fibre shapes in terms of the mean and RMS curvature was presented.

These results are important for they suggest that a parameterisation of fibre shape in terms of only a handful of parameters probably exists and, because the low frequency modes completely dominate, only comparatively low resolution images are needed to capture this information in future. Knowing that a fibre's space curve can be generated from a small number of easily measurable parameters help infer its processability and end-product performance.

Unfortunately, no strong conclusions could be made about torsion because the torsional parameters tended to be constant over the sample of 18 fibres. This uniformity may be an intrinsic feature of wool fibres.

The featureless exponential power spectrum is surprising because a "wavey" periodic pattern is often evident in the staple. However, the paths of individual fibres are fairly irregular when tracked through the staple (as may be inferred from Figure 56), which suggests that the expected peak in the power spectra will be rather weak. A superposition of the power spectra of the 18 fibres didn't show an obvious peak at nonzero frequency which suggests that the position of this peak probably depends on the staple.

Torsion sometimes seems slightly step-wise along the fibre's length — staying roughly constant in magnitude but changing sign occasionally — especially at large scales. This is not captured by the exponential power spectrum (or $\sqrt{\overline{\tau^2}} \propto \overline{|\tau|}$), but again, because of a lack of data, no other telltale peaks were observed. This could be the cause of the wavey pattern in the staple.

Finally, it would be an interesting exercise to explore the relationship between the bulk of the fibre and parameters such as $\bar{\kappa}$, $\sigma(\kappa)$, a_κ, etc. Bulk could be defined as the ratio of the volume of the smallest parallelopiped

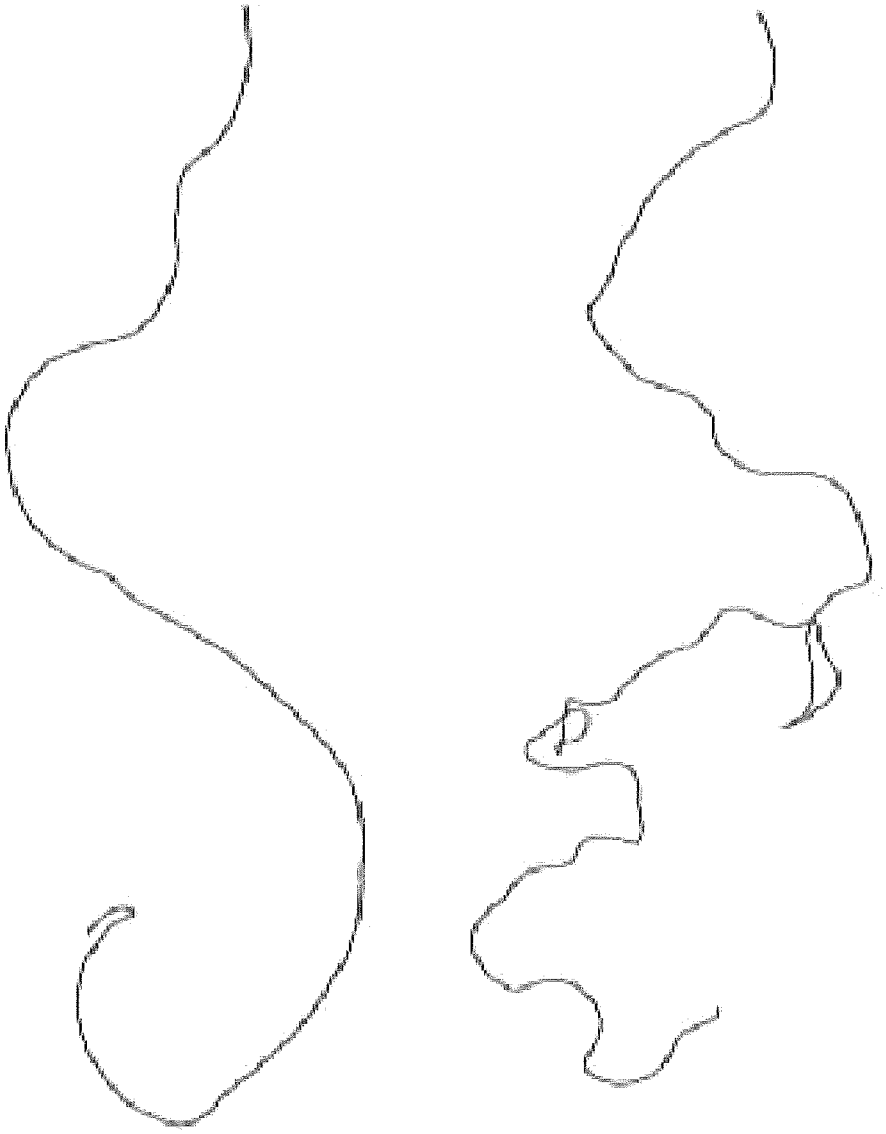

Figure 56: Two typical projections. The fibre on the left, which has length 71mm, has a smaller mean curvature than the fibre on the right with length 83mm.

that will enclose the fibre, to its length. There is a relationship between bulk (and fibre diameter) and curvature [19]: it would be amusing if something like Equation (6.13) emerged as a condition of maximum bulk.

7 Measurement of ultrastructure

7.1 Introduction

In this thesis, the assumption of determining the fibre shape is mainly based on the ultra-structure of the fibres. Therefore, it is important to be able to obtain some real data about the ultra-structure pattern and it can be used to estimate the local result shape of fibres. In order, it can help to understand the relationship between the fibre shapes and the causal factors. The microscopy technique used to obtain the cortical cells pattern will be shown in the next section. Then, with the measured pattern, it can be used by the mathematical model developed to calculate the resulting geometry and it will be explained afterward.

7.2 Microscopy technique

Three techniques are studied and compared in this report: Methylene Blue staining and Rhodamine B staining of transverse sections mounted in resin, and confocal microscopy on whole fibres stained with Rhodamine B. Methylene Blue staining of transverse sections mounted in resin is a relatively mature technology (Orwin et al [18]) and the interpretation of the images can be performed with relative confidence. However, there are two significant disadvantages: 1) it is destructive, the fibre needs to be cut and set in resin and 2) the setting of the section in resin is time consuming (hence expensive). Methylene Blue stained mounted transverse sections can be viewed with a conventional light microscope. Confocal microscopy can be performed on whole fibres, simply mounted on a slide, which have undergone an appropriate Rhodamine B staining protocol. This method is both non-destructive and requires significantly less labour (hence is cheaper). As an intermediate comparison, resin-mounted transverse sections were subjected to the Rhodamine B staining protocol and viewed with a fluorescence attachment for a

standard microscope.

1. Methylene Blue

   Methylene Blue preferentially stains the cuticle and the Para-cortex, and both these appear significantly darker in the images than the Meso-cortex with the Ortho-cortex lighter again. The technique involves completely staining the fibre then destaining until discrimination is achieved. Thus the absolute levels of 'darkness' and 'lightness' are variable between sections and depend on the overall level of destaining.

   Objective techniques for interpreting these images are under development. The (draft) basic rules are:

   (a) Any part of the cortex as dark as the cuticle is Para-cortex. It is likely that some parts of the cuticle will appear darker than others, the darker parts should be used as the 'guide'.

   (b) Any part of the cortex as light as the background (the part of the image outside the fibre) is Ortho-cortex or Ortho-like meso.

   (c) Anything in-between is Meso-cortex, with the darker parts Para-like meso and the lighter parts Ortho-like meso.

2. Rhodamine B (on mounted, transverse sections).

   Rhodamine B preferentially stains the Ortho-cortex which appears significantly lighter in the images than the Meso-cortex with the Para-cortex darker again. As for Methylene Blue, the absolute levels of 'darkness' and 'lightness' are variable between sections and depend on the penetration of the stain.

   Objective techniques for interpreting these images are under development. The (draft) basic rules are:

   (a) Any part of the cortex which is light is Ortho-cortex.

(b) Any part of the cortex as dark as the background (the part of the image outside the fibre) is Para-cortex or Para-like meso.

(c) Anything in-between is Meso-cortex, with the darker parts Para-like meso and the lighter parts Ortho-like meso.

3. Confocal Microscopy, using the Leica confocal microscope at Victoria University (Wellington) on Rhodamine B stained fibres.

   The staining protocol is identical to the Rhodamine B above and once the images have been converted from colour (they appear red and black as output by the microscope software) to greyscale they can be interpreted as above.

Figures (57) through (64) show Methylene Blue and Rhodamine B stained sections of Fibre 104/5 at points 1 and 3, Fibre 104.4 at point 5 and fibre 543.11 at point 1. In the Methylene Blue images, it can be seen that there are no areas of the cortices which are as dark as the cuticles and hence it is interpreted that there is no para-cortex. The images of the Rhodamine B stained sections have some light areas which are interpreted as areas of ortho-cortex. These correspond to light areas in the Methylene Blue images which is consistent. The grey areas in the Methylene Blue images correspond to grey/dark areas in the Rhodamine B images. These are interpreted as meso-cortex. Figures (65) through (68) show the confocal images of the same sections. There is good correspondence (allowing for a 90 degree anti-clockwise rotation) between Figures (63) and (67) and between Figures (64) and (68). The correspondence between the other two pairs of figures is not so good.

7.3 Simulation of ultrastructure in mathematical model

With the given MOP patterns of wool fibres, they can be used to estimate the local shapes of the fibre through the mathematical model developed. In

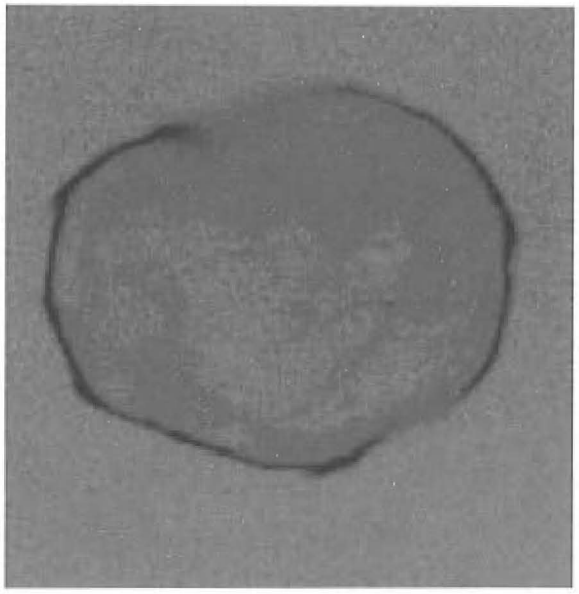

Figure 57: Methylene Blue image of Section 104-5-1

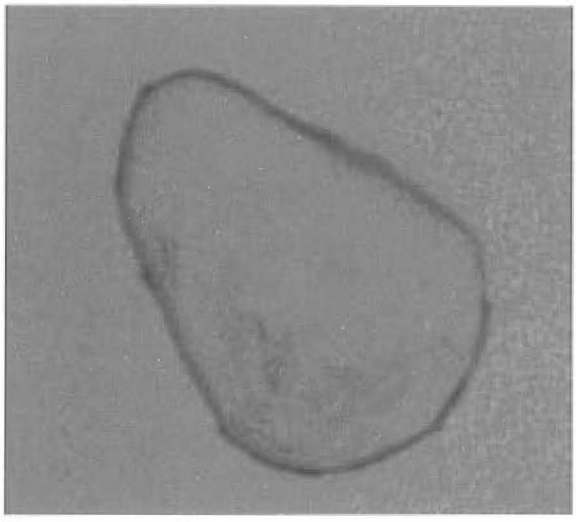

Figure 58: Methylene Blue image of Section 104-5-3

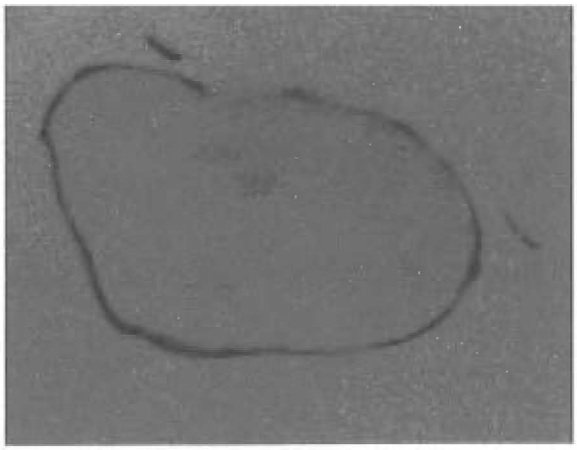

Figure 59: Methylene Blue image of Section 104-4-5

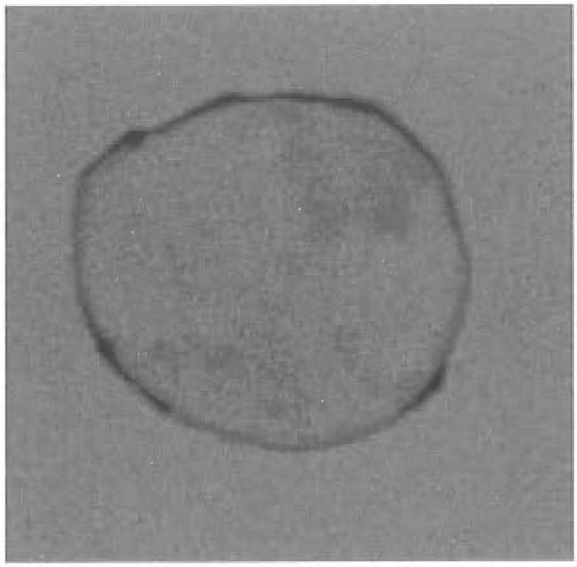

Figure 60: Methylene Blue image of Section 543-11-1

Figure 61: Rhodamine B image of Section 104-5-1

Figure 62: Rhodamine B image of Section 104-5-3

Figure 63: Rhodamine B image of Section 104-4-5

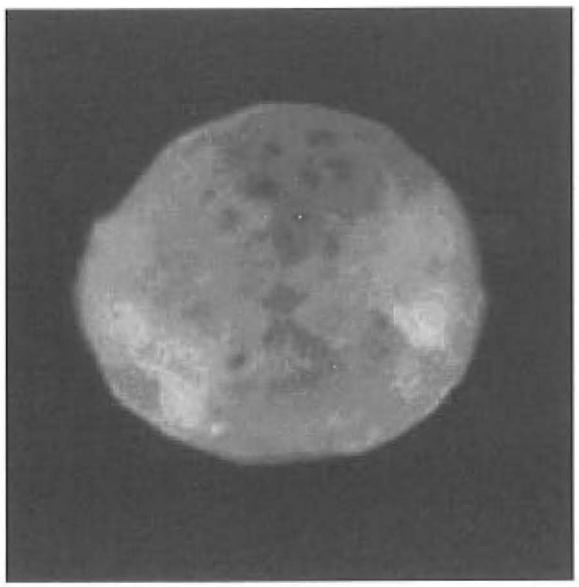

Figure 64: Rhodamine B image of Section 543-11-1

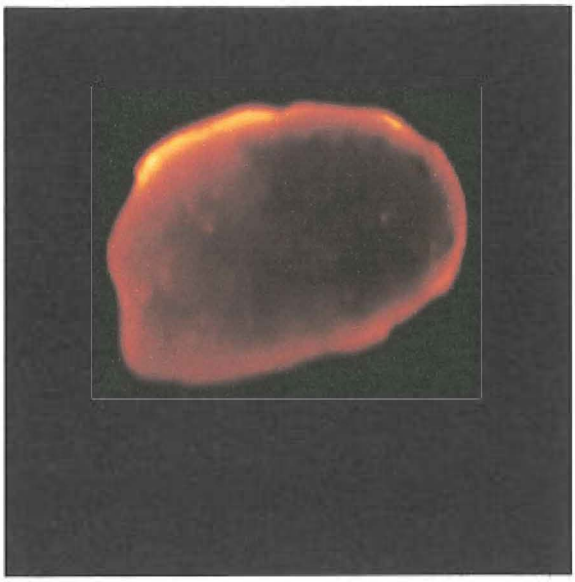

Figure 65: Confocal image of fibre 104-5-1

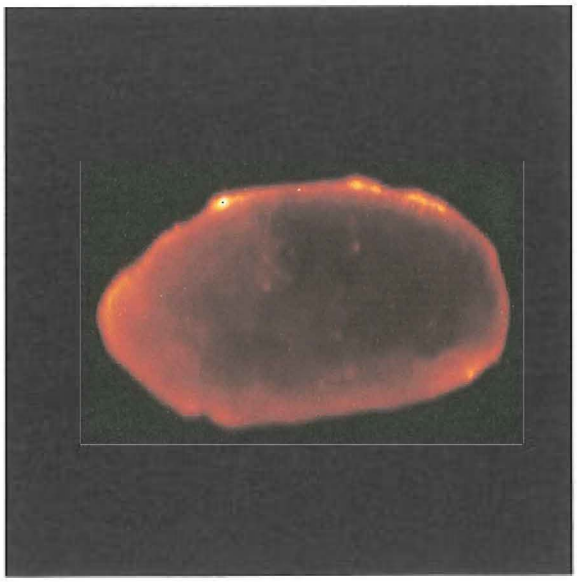

Figure 66: Confocal image of fibre 104-5-3

Figure 67: Confocal image of fibre 104-4-5

Figure 68: Confocal image of fibre 543-11-1

the previous chapter, it shows the method to measure the natural shape in curvature and torsion along the fibre. Then, with a chosen point on the fibre, the local cross-section can be obtained by microscopy and it will be used to calculate a simulated result by the mathematical model. By comparing the two sets of results, we can verify the accuracy of the mathematical model. There is still practical difficulty, it is hard to make sure that the two sets of results comparing are from the exactly same point. This problem will be possible to overcome with more time and more advanced technology in the future. From Figure 69 and 71, the light regions representing ortho-cortex will be placed with a number of helical IFs, the dark regions reckoned as para-cortex will be placed with rods, while the regions with darkness between these two will be thought as meso-cortex. Density of rods in meso-cortex will be around a half of that in para-cortex. Simple bilateral patterns examples are shown as follow. In the simulation, the original radius of the fibres is 15 μm, the radius of the helical IFs is 0.3 μm and the pitch angle is 30°. Basic model from Chapter 3 is using, with lateral dilation of 0.1, the estimated results of a sample MOP pattern from a high crimp fibre with around 60 : 40 ortho-to-para-cortex ratio are

$$\kappa = 1.86 \text{ mm}^{-1} ,$$

$$\tau = 3.12 \text{ mm}^{-1} ,$$

$$\rho = 1.02 ,$$

$$\theta = 4.71 ,$$

$$a = 0.14\text{mm} ,$$

$$c = 0.24\text{mm} ,$$

$$\kappa : \tau = 0.60 .$$

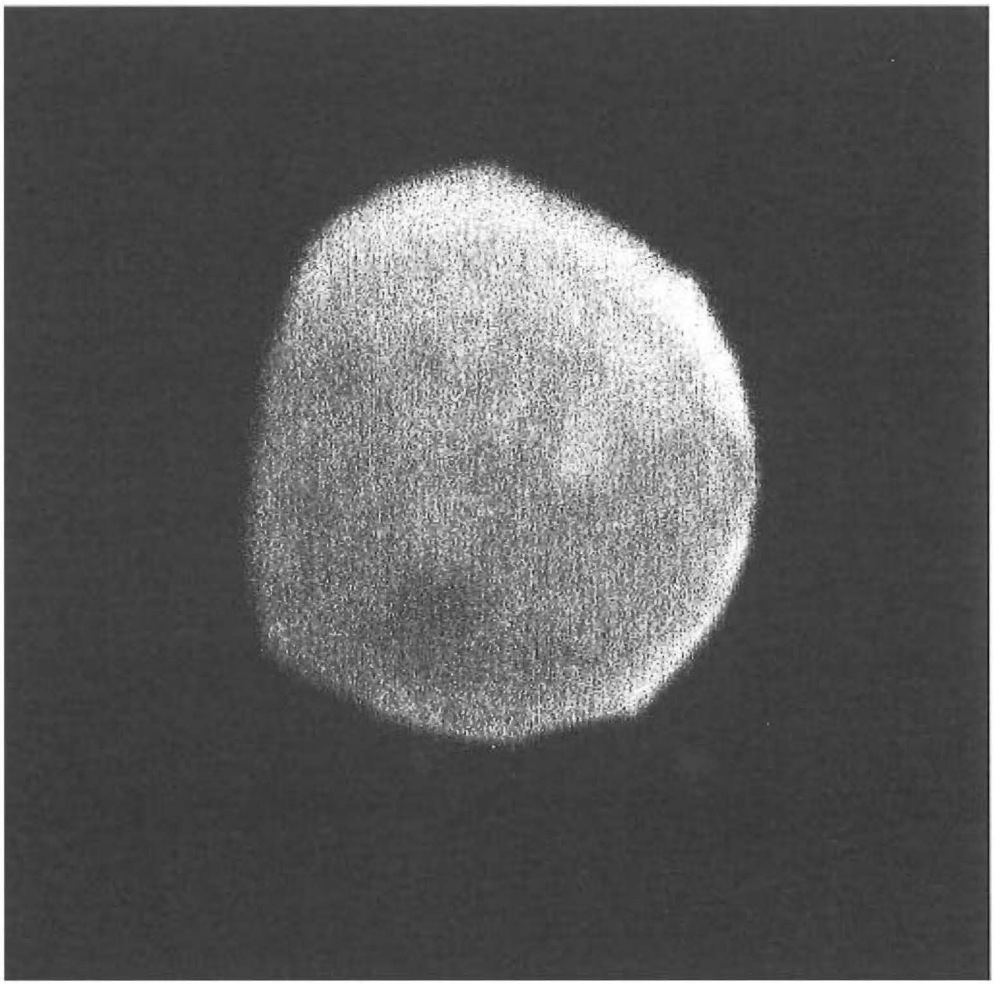

Figure 69: Confocal microscopy of a high crimp fibre

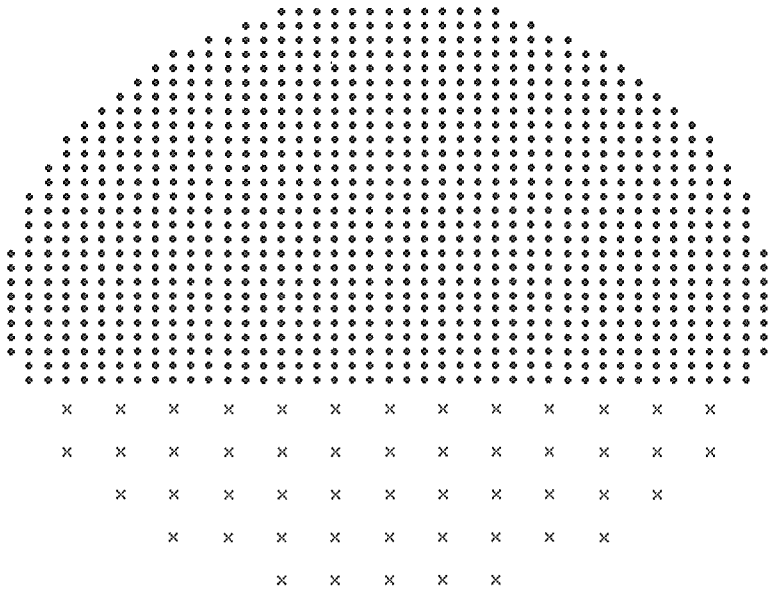

Figure 70: Simulated model of a high crimp fibre

Then, the estimated results of a sample MOP pattern from a low crimp fibre with around 30 : 70 ortho-to-para-cortex ratio are

$$\kappa = 1.34 \text{ mm}^{-1} ,$$

$$\tau = 11.53 \text{ mm}^{-1} ,$$

$$\rho = 1.00 ,$$

$$\theta = 4.71 ,$$

$$a = 0.01 \ \mu\text{m} ,$$

$$c = 0.09 \ \mu\text{m} ,$$

$$\kappa : \tau = 0.12 .$$

The MOP patterns are not usually distributed laterally and evenly, so a more refined model can be set up with irregular boundaries between different cortices. However, the given examples will be good enough to be approximated by some bilateral patterns.

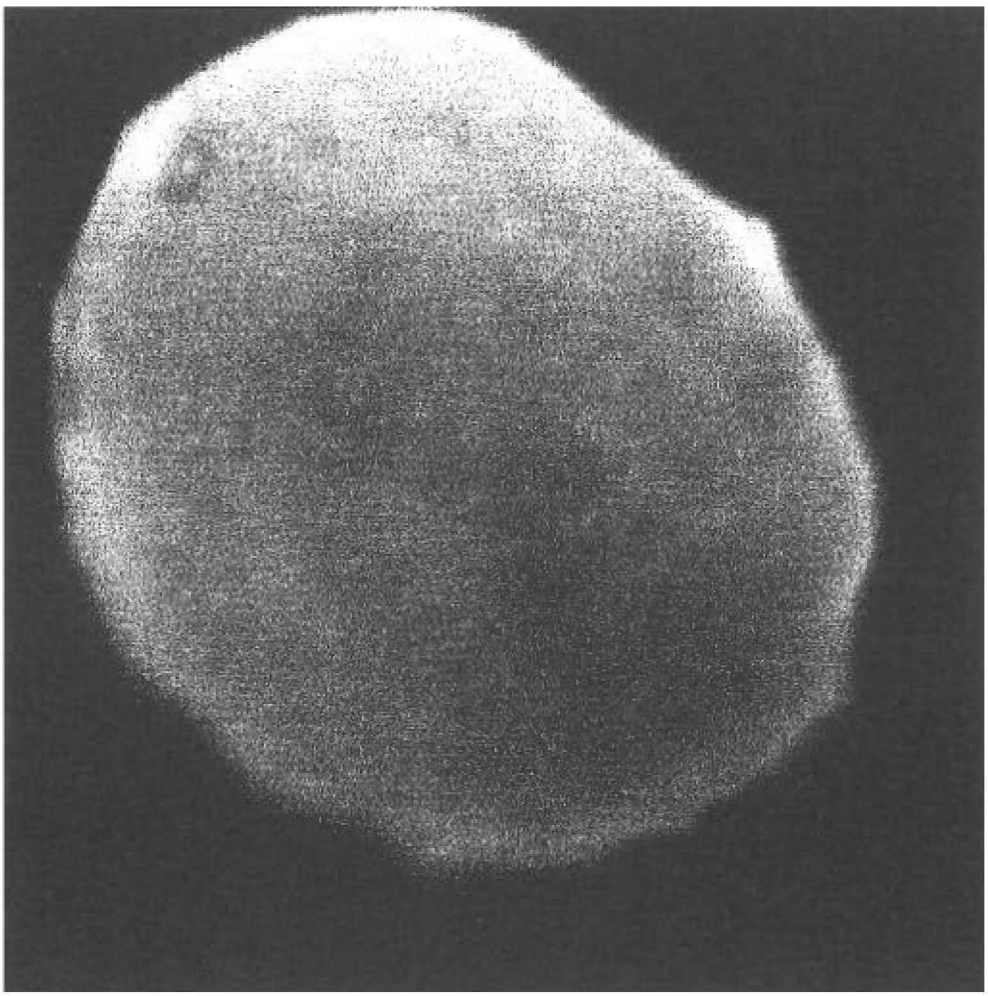

Figure 71: Confocal microscopy of a low crimp fibre

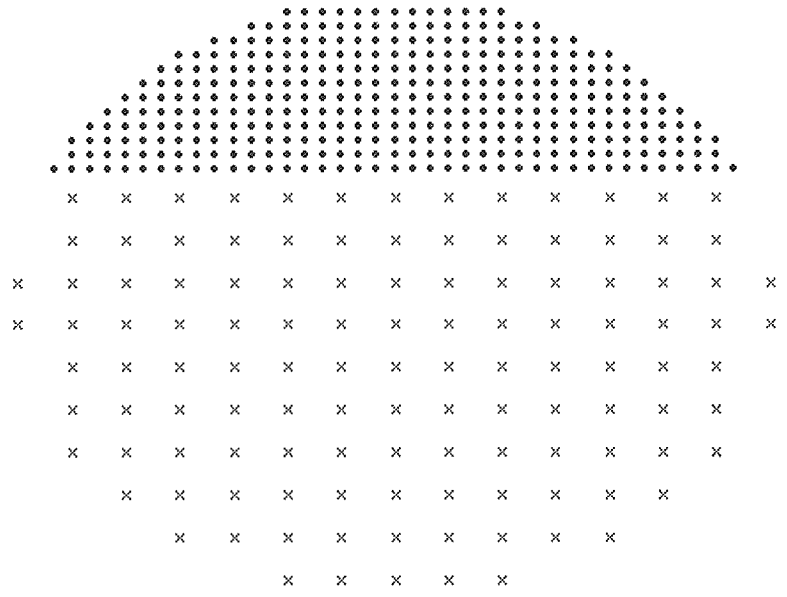

Figure 72: Simulated model of a low crimp fibre

8 Conclusion

In this thesis we have presented a mathematical model for simulating the local shape of wool fibre from its MOP pattern. In the past this problem has been studied as bimetallic (or multimetallic) strip model, in which the deformed shape is described with curvature alone and zero torsion. Here we have shown a model with the presence of curvature and torsion together is more appropriate to depict the 3D curve of real wool fibres. With the consideration of the ultrastructure, the model is more realistic and able to help us to understand the effect from the ultrastructure to the fibre shape.

Since the mechanism mentioned in this thesis is just one of the dominant mechanisms and there are still many uncertainties in the knowledge of wool fibre, the results provided here are qualitative rather than quantitative. Moreover, there are improvements needed, especially the computation cost of the model. However, this model should be good enough as a basic model that gives reasonable estimations for the fibre shapes.

The basic model is a simple model that lacks the full sophistication incorporated in the detailed structures inside the fibre. However, it is still a good draft model that captures most of the properties qualitatively and it is easier to handle computationally. With the addition of the macrofibril structure, the model becomes more realistic. However, the increase of the number of IF elements causes the computation cost to increase exponentially. The curvature of the deformed fibre is also usually extremely small compared with the torsion. This is suspected to be caused by the IFs near the centre of the macrofibrils. Adding the cuticle shell to the model easily solved this problem. The continuum model was constructed so as to reduce the computational time. This model avoids the calculation of the strain energy of the individual IFs, but the multiple integral made the programming more complicated. It provides similar high torsion results as the macrofibril model and the problem can be solved with the addition of cuticle.

The key outcomes of this thesis are concluded as:

- The shape of the dry fibre is determined by the configuration of the fibre which minimises the strain energy summed over all microfibrils
- The strain energy is minimised mathematically as a function of four parameters: curvature, κ, torsion, τ, direction of bend, θ, elongation factor of fibre, ρ.
- The local shape of a fibre is therefore determined by the ultrastructure of its cortex.
- This simple model using rods and helices as structural elements in the cortex predicts 3D fibre shapes similar to the measured fibres.
- The macrofibril model is constructed from the basic model from inducing the macrofibrils structure as bundles of concentric helices and rods.
- The macrofibril model produces extreme curvature-to-torsion ratio but it can be corrected by the addition of the cuticle shell.
- The continuum model calculates the strain energy of the wool fibres by integration instead of summing up the strain energy of individual IFs, which has similar properties as the macrofibril model.
- The results from this thesis show the relationship between the ultrastructure and the macrostructure of the wool fibres and verify the theory in Munro and Carnaby model is working.

Several problems and extensions remain open for future modelling. Some of the ultrastructures are not considered, such as the matrix cells around the IFs or the modulations formed in some of the fibres. There are some possible mechanisms also affecting the shapes of the fibres, e.g. differential growth of the different cortical cells. Some of the assumptions may need to be altered, such as the assumption of no shearing between the IFs. Some of the data

required has not yet been adequately determined. Some parameters such as the Young's modulus of a single IF are impossible to measure. Since it is possible to control the ultrastructure of the wool fibre with the development of genetic engineering. Hence, if we know the ultrastructure that can give more crimpy wool fibre, it is possible to control the fibre shape and improve the quality of the wool fibre by genetic engineering. This thesis describes a small step into the area of wool research that is largely unexplored. With a better understanding of the mechanisms which govern the formation of wool crimp from the ultrastructure, it is hoped that better formulation and solutions to the problems we have studied will be forthcoming in the future, to the benefit of the wool industry and mathematical modelling.

Appendices

A The geometry of space curves and fibres

A space curve is a one-dimensional curve that is immersed in three-space. Denote the arc-length along the curve by s. Points on the curve may then be described by the vector $\mathbf{l}(s)$ with respect to some global origin in three-space. The tangent, principal normal and principal binormal vectors to the curve are respectively

$$\begin{aligned} \mathbf{T}(s) &= \frac{\mathrm{d}\mathbf{l}(s)}{\mathrm{d}s}, \\ \mathbf{N}(s) &= \kappa^{-1}\frac{\mathrm{d}\mathbf{T}(s)}{\mathrm{d}s}, \\ \mathbf{B}(s) &= \mathbf{T}\times\mathbf{N}. \end{aligned} \tag{A.14}$$

These three vectors are defined as unit vectors, which in turn define the *curvature* κ. Thus $(\mathbf{T},\mathbf{N},\mathbf{B})$ define an orthonormal frame at every point along the space curve.

The Frenèt equations introduce the *torsion* τ, in order to write further relations between the vectors:

$$\begin{aligned} \frac{\mathrm{d}\mathbf{T}(s)}{\mathrm{d}s} &= \kappa(s)\mathbf{N}(s), \\ \frac{\mathrm{d}\mathbf{N}(s)}{\mathrm{d}s} &= -\kappa(s)\mathbf{T}(s)+\tau(s)\mathbf{B}(s), \\ \frac{\mathrm{d}\mathbf{B}(s)}{\mathrm{d}s} &= -\tau(s)\mathbf{N}(s). \end{aligned} \tag{A.15}$$

Hence κ is the reciprocal of the radius of curvature of a planar arc which locally approximates the space curve, and τ parameterises the curve's out-of-plane bending.

The example that is often used in this thesis is the helix. Its space curve

is

$$\mathbf{l}(s) = \left(a\cos(s/\sqrt{a^2+c^2}), a\sin(s/\sqrt{a^2+c^2}), \frac{cs}{\sqrt{a^2+c^2}} \right) .$$

Here a is the "radius" of the helix and c is its "pitch". During one cycle of the helix it travels $2\pi c$ along the z axis: this distance is often called the "pitch distance". The pitch angle ϕ is

$$\tan\phi = c/a .$$

The orthonormal tangent, principal normal and principal binormal vectors are

$$\begin{aligned}
\mathbf{T} &= \frac{1}{\sqrt{a^2+c^2}} \left(-a\sin(s/\sqrt{a^2+c^2}), a\cos(s/\sqrt{a^2+c^2}), c \right) , \\
\mathbf{N} &= \left(-\cos(s/\sqrt{a^2+c^2}), -\sin(s/\sqrt{a^2+c^2}), 0 \right) , \\
\mathbf{B} &= \frac{1}{\sqrt{a^2+c^2}} \left(c\sin(s/\sqrt{a^2+c^2}), -c\cos(s/\sqrt{a^2+c^2}), a \right) ,
\end{aligned}$$

and the curvature and torsion are

$$\kappa = \frac{a}{a^2+c^2} \quad \text{and} \quad \tau = \frac{c}{a^2+c^2} .$$

The fibres studied in this thesis are not truly one-dimensional curves, but are more like slender rods in that they have cross-sections of non-zero area. A "datum line" may be attached to each cross-section, and the parameter $\theta(s)$ is introduced to parameterise the angle between the datum line and the principal normal. This is shown in Figure 20.

In the case of a prismatic fibre, where all cross-sections are identical in shape and ultrastructure distribution, the natural choice is to take the same datum line for each cross-section. Since a prismatic fibre has translational invariance along its length, the curvature and torsion must be independent of arc length. However, θ may be linear in s without violating translational invariance, which means the cross-sections may rotate at a uniform rate around

the reference curve. This degree of freedom is not studied in this thesis.

B The formulations of long and short rod model

Long and short rod model is basically the same as the basic model in Chapter 3 except the helices are replaced by long rods. Let n_l be the number of long rods, n_s be the number of short rods. The positions of the long rods on the fibre cross-section are parameterised by the set $(d_\mathrm{l}^i, \theta_\mathrm{l}^i)$, with $i \in \{1, n_\mathrm{l}\}$, where d_l^i is the length of the vector from the reference curve of the wool fibre to the i^{th} long rod and θ_l^i is the angle between this vector and the datum line (refer to Figures 18 and 20 but the helical IFs are replaced by long rods). Similarly, the positions of a short rod is $(d_\mathrm{s}^i, \theta_\mathrm{s}^i)$ with $i \in \{1, n_\mathrm{s}\}$. The formulations of both the long and short rods are the same except the initial arc length of a long rod is $L_l^i = \alpha L$ where $\alpha > 1$ and the initial arc length of a short rod is $L_s^i = L$. Then, refer to equations (3.2) and (3.3), the deformed arc length of a long rod is,

$$\tilde{L}_\mathrm{l}^i = \rho L \sqrt{\left(1 - \tilde{d}_\mathrm{l}^i \cos(\theta_\mathrm{l}^i - \theta)\kappa\right)^2 + \left(\tilde{d}_\mathrm{l}^i \tau\right)^2} \,,$$

and the strain energy of a single long rod is,

$$e_\mathrm{l}^i = \frac{1}{2} \frac{E_\mathrm{l} A_\mathrm{l}}{L_\mathrm{l}^i} \left(L_\mathrm{l}^i - \tilde{L}_\mathrm{l}^i\right)^2 \,,$$

where E_l is the Young's modulus and A_l is the transverse cross-sectional area of the long rods.

Similarly, the deformed arc length of a short rod is,

$$\tilde{L}_\mathrm{s}^i = \rho L \sqrt{\left(1 - \tilde{d}_\mathrm{s}^i \cos(\theta_\mathrm{s}^i - \theta)\kappa\right)^2 + \left(\tilde{d}_\mathrm{s}^i \tau\right)^2} \,,$$

and the strain energy of a single short rod is,

$$e_{\mathrm{s}}^{i} = \frac{1}{2}\frac{E_{\mathrm{s}}A_{\mathrm{s}}}{L_{\mathrm{s}}^{i}}\left(L_{\mathrm{s}}^{i} - \tilde{L}_{\mathrm{s}}^{i}\right)^{2} ,$$

where E_{s} is the Young's modulus and A_{s} is the transverse cross-sectional area of the long rods.

Hence, the total energy of a wool fibre is

$$e_{\mathrm{w}}(\kappa, \tau, \rho, \theta) = \sum_{i=1}^{n_{\mathrm{l}}} e_{\mathrm{l}}^{i} + \sum_{i=1}^{n_{\mathrm{s}}} e_{\mathrm{s}}^{i} .$$

C Two-dimensional stress and strain

In Section 3.7 a thin cylindrical cuticle was added to the exterior of the fibre. Such thin shells are conventionally considered to be essentially two-dimensional and their thickness is added in at convenient times. The following provides some background.

Locally coordinatise the shell with cartesian coordinates x_1 and x_2. The stress tensor is denoted by σ and the strain tensor by ϵ. In general the stress-strain Hooke's law reads

$$\begin{pmatrix} \epsilon_{11} \\ \epsilon_{22} \\ \sqrt{2}\epsilon_{12} \end{pmatrix} = C^{-1} \begin{pmatrix} \sigma_{11} \\ \sigma_{22} \\ \sqrt{2}\sigma_{12} \end{pmatrix} ,$$

where C is called the "compliance matrix" of the shell.

When the shell is homogeneous and isotropic

$$C = \begin{pmatrix} \lambda+\mu & \lambda & 0 \\ \lambda & \lambda+\mu & 0 \\ 0 & 0 & \mu \end{pmatrix}$$

, so

$$C^{-1} = \begin{pmatrix} \frac{\lambda+\mu}{(\lambda+\mu)^2-\lambda^2} & -\frac{\lambda}{(\lambda+\mu)^2-\lambda^2} & 0 \\ -\frac{\lambda}{(\lambda+\mu)^2-\lambda^2} & \frac{\lambda+\mu}{(\lambda+\mu)^2-\lambda^2} & 0 \\ 0 & 0 & \frac{1}{\mu} \end{pmatrix} ,$$

where λ and μ are called the Lamè constants. These can be written in terms of the Young's modulus and Poisson's ratio of the shell which are defined physically as follows. When the only non-zero component of the stress tensor is σ_{11} then the strain components are

$$\epsilon_{11} = \frac{1}{E_c}\sigma_{11} ,$$

and

$$\epsilon_{22} = -\nu\epsilon_{11} = -\frac{\nu}{E_c}\sigma_{11} .$$

Here E_c is Young's modulus and ν is the Poisson ratio of the shell. Therefore,

$$\frac{\lambda+\mu}{(\lambda+\mu)^2-\lambda^2} = \frac{1}{E_c} \qquad \text{and} \qquad -\frac{\lambda}{(\lambda+\mu)^2-\lambda^2} = -\frac{\nu}{E_c} ,$$

or

$$\lambda+\mu = \frac{E_c}{1-\nu^2} \qquad \text{and} \qquad \mu = \frac{E_c}{1+\nu} ,$$

References

[1] Alexander, E., Menachem, L., Muhsam, H. V. and Shiloh, M. Definition and Measurement of Crimp of Textile Fibres, Textile Res. J. 26, 606–617 (1956).

[2] Bak, P., How Nature Works: The Science of Self-Organized Critically, Copernicus Press, New York, 1996.

[3] Batra, S. K., A Generalized Model for Crimp Analysis of Multi-Component Fibers, Part I: Theoretical Development, Textile Research

Journal, May, 1974, 377-385.

[4] Batra, S. K., A Generalized Model for Crimp Analysis of Multi-Component Fibers, Part II: An Illustrative Example, Textile Research Journal, May, 1974, 386-392.

[5] Brims, M. A., New OFDA developements and the use of OFDA as a projection microscope, IWTO Technical Committee Meeting, Istanbul, May 1993, Report 22.

[6] Caldwell, J., New AFM measurements of fibre moduli, unpublished preprint.

[7] Dabbs, T. P., van Schie, H. and Glass, M. The Effect of Fibre Curvature on Laserscan Diameter Measurement, IWTO Technical Committee Meeting, Nice, December 1994, Report 2.

[8] Edmonds, A. R., Measurement of Fibre Curvature: A Review of Work to Date, Wool Tech. Sheep Breed. 45, 227-234, 1997.

[9] Fraser, R. D. B., and Rogers, G. E., The bilateral structure of wool cortex and its relation to crimp, Aust. J. Biol. Sci., Vol.8, No. 2.

[10] Horio, M., and Kondo, T., Crimping of Wool Fibers, Textile Research Journal, vol. XXIII, No. 6, June, 1953.

[11] Kaplin, I., J., and Whiteley, K., J., An Electron Microscope Study of Fibril: Matrix Arrangements in High- and Low-crimpWool Fibres, Aust. J. Biol. Sci., 1978, 31, 231-40.

[12] Kozyreff, G., Ockendon, H., Sumner, R. W. M. and Wake, G. C., Core Bulk of Wool Fibres as a Function of their Curvature and Diameter, Physics Letter A, 2003, 314, Issues 5-6, pp. 428-443.

[13] Martin, E., Adamchik, V., Wolfram Research, Mathematica 3.0 standard add-on packages/ edited by Emily Martin; with contributions by Victor Adamchik...[et al.], champaign, III: Wolfram Media; Cambridge: New York: Cambridge University Press, c1996.

[14] Marsh, C., Tsang, B., and Wilkins, A., Free Wool Fibre Shape, AUTEX Research Journal, Vol. 3, No. 4, December 2003.

[15] Mercer, E. H., The Heterogeneity of the Keratin Fibers, Textile Research Journal, June, 1953, 388-397.

[16] Munro, W. A., and Carnaby, G. A., Wool fibre crimp, Part I: The Effects of micro-fibrillar geometry, J. Text. Inst., Vol. 90, Part 1, No. 2, pp. 123-136 (1999).

[17] Orwin, D. F. G., The Cytology and Cytochemistry of the Wool Follicle, International Review of Cytology, Vol.60.

[18] Orwin, D. F. G., Woods, J. L., and Ranford, S. L., Cortical Cell Types and their Distribution in Wool Fibres, Aust. J. Biol. Sci., 1984, 37, 237-55.

[19] Sumner, R. M. W., and Upsdell, M. P., Factors Associated with the Prediction of Core Bulk from Fibre Diameter and Fibre Curvature of Individual Fleeces, Wool Tech. Sheep Breed. 49, 29–41 (2001). Also, see references in [8].

[20] Yang, W. L., and Yang, S. K., Analysis of the Curvature in Bicomponent Fibers with Complex Cross Sections, Textile Research Journal, May, 1972, 298-300.